Manipulation of light transport in disordered media by reciprocal design

Vom Promotionsausschuss der
Technischen Universität Hamburg

zur Erlangung des akademischen Grades

Doktor der Naturwissenschaften (Dr. rer. nat.)

genehmigte Dissertation

von

Lukas Maiwald

aus

Lüneburg

2023

Gutachter:
Dr. rer. nat. habil. Alexander Petrov
Prof. Dr.-Ing. habil. Alexander Kölpin

Vorsitzender des Prüfungsausschusses:
Prof. Dr. rer. nat. Patrick Huber

Tag der mündlichen Prüfung:
29. August 2023

DOI:
https://doi.org/10.15480/882.8546

ORCID iD:
https://orcid.org/0000-0001-6682-8482

Abstract

The highly ordered photonic crystals have been a topic of major scientific interest for more than 30 years now. However, in recent years disordered photonic structures have gained increasing attention. This thesis focuses on the optical transport effects in quasiperiodic structures, placing it right in between the two types of structures.

We create a quasiperiodic model structure from the superposition of several 1D sinusoidal gratings. This generation scheme yields a highly flexible template for the optimization of the structure for different purposes. Also, being based on a simple mathematical model, the structure allows an extensive analytical study of its properties. We will use this structure for two main topics:

In the first part, we generate the structure using a large number of underlying gratings to obtain a sharp spherical shell in reciprocal space. Thereby, it acts as an idealized model for a structural color material. Based on this, we use analytical modeling and numerical simulation to investigate the applicability of the Ewald sphere construction to structural colors. We find that it is well suited for qualitative predictions of the scattering directions, and that quantitative results can be obtained for weakly scattering structures. Moreover, we find that the Fresnel reflection at the interface of a color film can have a significant effect on its reflection spectrum, making it an important design factor especially for long-wavelength structural colors.

In the second part, we optimize the structure towards blocking light propagation for all directions and polarizations of light. Such a complete bandgap allows the precise control of light transport and emission, but so far it could only be realized in materials with very high refractive indices. Using mathematical modeling we derive an optimum set of parameters for our model structure. Based on this, we show that it can open a complete bandgap for any refractive index. We support this finding by numerical simulations, showing a complete bandgap in a 2D structure with an extremely low refractive index of 1.11. In 3D we do not find a bandgap, but the structure allows an unprecedented emission suppression of nearly 10 dB at a refractive index of only 1.38. We also show that the structure can be realized by additive manufacturing and confirm some of its properties by microwave transmission measurements.

Zusammenfassung

Die stark geordneten photonischen Kristalle sind seit über 30 Jahren ein wesentlicher Bestandteil der Photonik. In jüngeren Jahren erfreuen sich allerdings auch ungeordnete photonische Strukturen eines wachsenden wissenschaftlichen Interesses. Diese Arbeit befasst sich primär mit der Lichtausbreitung in quasi-geordneten photonischen Materialien und setzt somit an der Schnittstelle zwischen den zwei Extremen an.

Eine quasi-periodische Modellstruktur wird durch Überlagerung mehrerer sinusoidaler 1D-Gitter erzeugt. Durch die hohe Zahl von Freiheitsgraden bei der Generierung dieser Struktur lässt sie sich flexibel an die Anforderungen verschiedener Anwendungen anpassen. Darüber hinaus erlaubt ihre einfache Formulierung eine umfassende mathematische Analyse ihrer Eigenschaften. In dieser Arbeit soll die Anwendung dieser Struktur im Rahmen zweier Themenschwerpunkte gezeigt werden:

Im ersten Teil wird die Struktur mit einer sehr hohen Anzahl der ihr zugrundeliegenden Gitter erzeugt. Dadurch erzeugt sie eine scharfe Kugelschale im reziproken Raum und kann daher als idealisierte Modellstruktur für eine Strukturfarbe genutzt werden. Darauf aufbauend werden analytische und numerische Methoden verwendet, um die Anwendbarkeit der Ewald-Sphären-Konstruktion auf Strukturfarben zu untersuchen. Die Konstruktion eignet sich demnach gut für qualitative Vorhersagen der Streurichtung; für sehr schwache Streuung lassen sich auch quantitative Ergebnisse erzielen. Darüber hinaus wird gezeigt, dass die Fresnel-Reflexion an der inneren Oberfläche eines Farbfilms gerade bei Strukturfarben einen maßgeblichen Einfluss auf die Farbgebung hat. Dadurch wird diese zu einem entscheidenden Design-Parameter, insbesondere bei der Realisierung langwelliger Strukturfarben.

Im zweiten Teil wird die Optimierung der Struktur mit dem Ziel einer exponentiellen Unterdrückung von Lichttransport für alle denkbaren Richtungen und Polarisationen gezeigt. Eine solche vollständige Bandlücke erlaubt die präzise Steuerung der Lichtausbreitung und -emission. Bisher war dies Materialien mit sehr hohen Brechungsindizes vorbehalten. Durch mathematische Modellierung wird gezeigt, dass für jeden beliebigen Brechungsindex ein Satz von optimalen Parametern für die Modellstruktur existiert, der dieser erlaubt, eine vollständige Bandlücke zu öffnen. Durch numerische Simulationen wird diese Vorhersage für den 2D-Fall bestätigt, eine vollständige Bandlücke für einen extrem geringen Brechungsindex von etwa 1,11 wird

nachgewiesen. Im 3D-Fall wird keine Bandlücke im eigentlichen Sinne gefunden, es lässt sich aber eine Emissionsunterdrückung von fast 10 dB bei einem Brechungsindex von nur 1,38 zeigen. Abschließend wird noch dargelegt, dass die Struktur durch additive Fertigung hergestellt werden kann. Einige ihrer Eigenschaften werden in Transmissions-Experimenten im Mikrowellen-Bereich nachgewiesen.

Contents

Abstract ..... **I**

Zusammenfassung ..... **II**

List of figures ..... **VI**

1 Introduction **1**

1.1 Disordered photonics 1

1.2 Thesis outline 2

2 Theoretical background **4**

2.1 Electromagnetic waves 4

2.1.1 Scale invariance of Maxwell's equations 6

2.1.2 Relative permittivity vs. refractive index 7

2.1.3 Perturbation theory 8

2.2 A scattering landscape 9

2.3 Photonic structures 13

2.3.1 Photonic crystals 13

2.3.2 Photonic quasicrystals 20

2.3.3 Short-range ordered photonic structures 22

2.3.4 Model structure 23

2.4 FIT simulations 25

3 Ewald sphere for structural colors **29**

3.1 Introduction to structural colors 29

3.2 Ewald sphere construction 30

3.2.1 Derivation 31

3.2.2 Geometrical interpretation 35

3.2.3 Application to k-shell structures 37

3.2.4 Scattering from a film 40
3.3 Model structure 43
3.4 Simulation method 46
3.5 Results and discussion 47
3.6 Chapter conclusions 52
4 Complete photonic bandgaps in quasiperiodic structures 54
4.1 Introduction 54
4.2 Model structure 56
4.3 Bandgap estimation 59
4.4 Simulation method 67
4.5 Results and discussion 67
4.5.1 2D structures 67
4.5.2 3D structures 70
4.6 Experimental realization 73
4.7 Chapter conclusions 78
5 Conclusions and outlook 80
5.1 Structural colors 80
5.2 Complete photonic bandgaps 82
6 References 84
List of publications 95
Curriculum Vitae ..... Fehler! Textmarke nicht definiert.

List of figures

Fig. 1. Some important aspects of real and reciprocal lattices illustrated for the 2D hexagonal lattice. 14

Fig. 2. Schematic depiction of a simple Bragg mirror and the Fresnel reflections at its material interfaces. 16

Fig. 3. Schematic band diagram of a simple Bragg mirror. 18

Fig. 4. Bragg peak distributions for periodic structures in 2D and 3D. 24

Fig. 5. Primary and dual grid used in the FIT method for one exemplary mesh cell. 26

Fig. 6. Ewald sphere construction for the example of a Bragg mirror with a low refractive-index contrast. 36

Fig. 7. 2D cut through the Ewald sphere construction for the scattering from a structure with a spherical-shell shaped Fourier transform. 38

Fig. 8. Schematic visualization of the intersection between the Ewald sphere and an infinitesimally thin k-shell. 39

Fig. 9. Schematic 2D representation of the scattering in a film as a function of wavelength. 42

Fig. 10. Real-space representation of the investigated structure. 43

Fig. 11. Fourier-space representation of the investigated structure 44

Fig. 12. Simulation results and their connection to the theoretical considerations based on the Ewald sphere. 48

Fig. 13. Different ways of reaching the critical reflection angle after double or single scattering. 50

Fig. 14. Wavelength-dependent scattering directions of the simulated structure 51

Fig. 15. Quasiperiodic structures in real and reciprocal space. 57

Fig. 16. Influence of the structure binarization on the Bragg peak strength 59

Fig. 17. Formation of the CPBG from several individual grating bandgaps. 60

Fig. 18. Connection of grating directions and scattering directions. 60

Fig. 19. Schematic representation of the effective 3D Brillouin zone approximated with only hexagonal facets. 65

Fig. 20. Normalized power emission of a dipole placed inside a square-shaped 2D quasiperiodic structure. 68

Fig. 21. Comparison of the relative omnidirectional bandgap width in theory and simulation. 69

Fig. 22. Normalized emitted power spectrum of a dipole placed inside a 3D quasiperiodic structure. 71

Fig. 23. Far-field simulation results from a spherical 3D structure. 72

Fig. 24. Photograph of the 3D-printed structure. 74

Fig. 25. Scheme (A) and photograph (B) of the experimental setup for transmission measurement. 75

Fig. 26. Measured transmission spectrum of the 3D-printed structure. 76

Fig. 27. Comparison of the transmission spectra seen in experiment and simulation. 77

Fig. 28. Angle mapping of the measured transmission at wavelengths around the bandgap. 78

Fig. 29. Reciprocal design for narrow-band light trapping. 81

1 Introduction

1.1 Disordered photonics

In the late 1980s the topic of photonic crystals [1] started to attract great research interest and has since then not ceased to do so. Being able to fully control the flow of light promised to enable a diverse range of new technologies in the fields of sensing, lasing and optical computing, among others. Today, more than 30 years have passed since the emergence of the field; and while the fundamental principles of the light-matter interaction in photonic crystals are well understood, many questions are still open and research opportunities remain plenty.

In the early days of photonic crystals, highly ordered structures were investigated, while any kind of random disorder usually stemmed from manufacturing defects and was generally seen as detrimental to the performance of the structures. However, more recently the topic of disordered photonics has evolved into a research area in its own right [2]. A lot of work has been focused on the understanding of light transport in disordered optical media. One of the primary aims is the reconstruction of phase fronts that are modulated by the propagation through disordered materials. If the modulation could be measured exactly, the underlying image could be reconstructed, allowing applications like imaging through biological tissues [3].

Other approaches aim for actively taking advantage of controlled degrees of disorder. While the field is still young, and research is mostly fundamental, interesting technical applications can be envisaged. Two commonly named examples are random lasers [4, 5] and enhanced light trapping in solar cells [6–8]. One of the advantages of materials that are designed to be disordered is that they are generally more robust to random disorder, e.g., from manufacturing defects [2]. Additionally, many of the properties of photonic crystals can also be found in structures that are not perfectly crystalline but only partially ordered [9, 10]. Such structures can even outperform traditional photonic crystals in applications where their larger isotropy is beneficial.

It is this last point that we will take advantage of throughout this thesis: For one, we are going to look at structural colors. Structural colors differ from traditional pigment or dye colors in that they obtain their color from a combination of spectrally selective scattering and broadband absorption. Traditional colors instead are based on selective absorption,

potentially combined with broadband scattering. Since the selective absorptivity requires different material properties for different wavelengths, a broad range of materials are needed to obtain a full color palette, which in some cases entails the need for toxic compounds [11]. In contrast to this, an ideal structural color could just be resized to different length scales to obtain all colors.

Most structural colors are iridescent, i.e., they change their color impression based on the illumination situation or the observer position. This creates beautiful effects in its own right, like the shimmering plumage of peacocks or the play of colors in opals or mother of pearl. However, to replace traditional colors, structural colors are required to be non-iridescent. This requires angular isotropy and therefore the utilization of disordered structures.

In the second major topic of this thesis, we are going to build on the understanding gained in the first part. Based on coherent scattering, non-iridescent structural colors produce a reflection peak for all directions. Along with this goes the fact that they suppress transmission for all directions in the same wavelength range; they are said to form a pseudo-bandgap[1] [12]. However, for technical applications there has been a decade-long hunt for materials that form a complete photonic bandgap, i.e., materials that fully suppress light propagation in all directions, at as low as possible refractive indices. Complete bandgaps have been shown in ordered, crystalline media but they require a very large refractive index which drastically limits the material choice. To reduce the required refractive index, the angular isotropy needs to be optimized, which is not compatible with strict crystalline order. Therefore, we again add an element of disorder to gain an advantage over purely ordered structures.

1.2 Thesis outline

The second chapter following this introduction is meant to give the reader an overview of the background knowledge that is needed to follow the discussions afterwards. Starting from Maxwell's equations we will present the derivation of important electromagnetic principles and the assumptions going into them. An introduction to optical scattering in general is given in chapter 2.2. Then, in chapter 2.3 we will present different kinds of optical structures sorted by their degree of disorder. The theoretical description of the light transport in the different classes is discussed. We also introduce the model structure

[1] The term is not consistently used in literature. In some cases, it is used to describe a regular directional bandgap in contrast to a complete (omnidirectional) bandgap. But in the case of structural colors, and therefore in our discussion, it denotes a frequency range where the transmission is significantly reduced without exponentially converging towards zero over sample thickness.

which most of this work is based on, and which can hardly be categorized by the classes introduced before. Finally, a short introduction to the numerical method which the simulation results shown in this work were obtained with – the finite integration technique (FIT) – is given.

The third chapter covers the first of the two main research topics presented herein. It discusses the applicability of the first-order Born approximation and the resulting Ewald sphere construction to the scattering of light by disordered optical structures. The focus is on structures that resemble the natural structures found to be responsible for the non-iridescent structural color of bird plumage. We derive a mathematical model for optical scattering based on the first-order Born approximation. The model corresponds to the same intuitive graphical representation as the Ewald sphere construction known from X-ray scattering, but it also allows the explicit calculation of the power scattered by a color film. We compare the analytical model to numerical results obtained by FIT simulations. In doing so, we find that the Ewald sphere construction is well suited to make rough predictions of scattering, and that quantitative results can be obtained in cases where the structure is formed by weak modulations of the refractive index. Moreover, we find that the Fresnel reflection at the film-air interface plays an important role in obtaining a narrow peak in the reflection spectrum – one of the key requirements in order to make a structural color that can be scaled to obtain different hues.

In the fourth chapter we will discuss the second major topic of this thesis, which is the optimization of the previously used structure towards generating a complete photonic bandgap. An analytical first-order model is derived, which predicts that a complete bandgap should be obtainable even at arbitrarily low refractive indices. We verify this result by numerical simulations. In 2D, we find that the condition for maximum suppression predicted by the analytical model comes close to the optimum found in simulation. Also, the prediction of a complete bandgap is confirmed for the extremely low refractive index of 1.11. In 3D, we find no complete bandgap. Nonetheless, the structures are shown to significantly suppress light emission at very low refractive-index values. The 3D structures are materialized by additive manufacturing on microwave length scale. The strong omnidirectional suppression of light transport is confirmed by measurements.

Finally, the last chapter summarizes the main results of the thesis and discusses prospects for future research activities. In case of the structural color topic, we will also discuss the progress that has been made in the field since our work on the topic was published.

2 Theoretical background

This chapter presents the theoretical basics needed to understand the later parts of this thesis. Obviously, most of the knowledge presented here is derived from existing literature. In cases where all the information presented in a paragraph is taken from the same source, the reference is given at the end of the paragraph.

2.1 Electromagnetic waves

This chapter will give a very brief introduction to the basic equations we are dealing with when discussing electromagnetic waves. It is the foundation for the next chapter, where the general equations are applied to the special case of a periodic permittivity. Most of this subchapter and its first two subchapters (2.1.1 and 2.1.2) is based on the book *Photonic crystals: Molding the flow of light* by Joannopoulos et al. [1] which gives a comprehensive introduction to a large part of the electromagnetic theory needed to understand this work.

The foundation for modern electromagnetic theory was established by James C. Maxwell, who in 1865 published a set of coupled differential equations describing the main electromagnetic quantities and their interactions [13]. The equations are now commonly known as Maxwell's equations and can be written in their differential form as

$$\boldsymbol{\nabla} \times \mathbf{E}(\mathbf{r}, t) = -\frac{\partial \mathbf{B}(\mathbf{r}, t)}{\partial t}, \tag{1}$$

$$\boldsymbol{\nabla} \times \mathbf{H}(\mathbf{r}, t) = \frac{\partial \mathbf{D}(\mathbf{r}, t)}{\partial t} + \mathbf{J}(\mathbf{r}, t), \tag{2}$$

$$\boldsymbol{\nabla} \cdot \mathbf{D}(\mathbf{r}, t) = \rho(\mathbf{r}, t), \tag{3}$$

$$\boldsymbol{\nabla} \cdot \mathbf{B}(\mathbf{r}, t) = 0, \tag{4}$$

where **E** and **H** are the electric and magnetic field, **D** and **B** are the electric and magnetic flux density and $\boldsymbol{\nabla}$ is the nabla operator, $\boldsymbol{\nabla} = [\partial/\partial x, \partial/\partial y, \partial/\partial z]^T$. The variables ρ and **J** represent the free charge and the current density, however, since in this work we will only consider charge-free, non-conducting media we will generally assume $\rho = \mathbf{J} = 0$. This

restriction also leads to a conservation of the tangential components of the field quantities and the normal components of the flux densities at a material boundary.

The flux densities are connected to the field quantities by the material parameters. If we limit our considerations to linear, lossless, isotropic media – again, assumptions that are well-founded in the context of this work – and assume that dispersion is negligibly small in the frequency range of interest, these relations can simply be written as

$$\mathbf{D}(\mathbf{r},t) = \varepsilon_0 \varepsilon_r(\mathbf{r})\mathbf{E}(\mathbf{r},t), \tag{5}$$

$$\mathbf{B}(\mathbf{r},t) = \mu_0 \mu_r(\mathbf{r})\mathbf{H}(\mathbf{r},t), \tag{6}$$

with the permittivity $\varepsilon = \varepsilon_0\varepsilon_r(\mathbf{r})$ and the permeability $\mu = \mu_0\mu_r(\mathbf{r})$ split up into their vacuum (subscript 0) and their spatially dependent relative (subscript r) parts. Moreover, since most materials in optics are non-magnetic, we will assume $\mu_r = 1$. We can now substitute these equations back into the original Maxwell's equations to obtain

$$\boldsymbol{\nabla} \times \mathbf{E}(\mathbf{r},t) = -\mu_0 \frac{\partial \mathbf{H}(\mathbf{r},t)}{\partial t}, \tag{7}$$

$$\boldsymbol{\nabla} \times \mathbf{H}(\mathbf{r},t) = \varepsilon_0 \varepsilon_r(\mathbf{r}) \frac{\partial \mathbf{E}(\mathbf{r},t)}{\partial t}, \tag{8}$$

$$\boldsymbol{\nabla} \cdot \varepsilon_r(\mathbf{r})\mathbf{E}(\mathbf{r},t) = 0, \tag{9}$$

$$\boldsymbol{\nabla} \cdot \mathbf{H}(\mathbf{r},t) = 0. \tag{10}$$

The last two of the Maxwell's equations have two important consequences. First, the electric and magnetic fields have no sources or sinks. We eliminated the possibility of electric field sources and sinks by setting ρ to zero, and magnetic monopoles typically[2] do not exist; magnetic field lines are closed. Second, the field distribution has to be transverse. For example, if we look at the simple case of a magnetic plane wave described by $\mathbf{H}(\mathbf{r}) = \widehat{\mathbf{H}} \exp(i\mathbf{k} \cdot \mathbf{r})$, where $\mathbf{k}$ denotes the wave vector, and take its divergence, $\boldsymbol{\nabla} \cdot \mathbf{H}(\mathbf{r}) = i\widehat{\mathbf{H}} \cdot \mathbf{k} \exp(i\mathbf{k} \cdot \mathbf{r}) = 0$, we see immediately that to fulfill the condition in Eq. (10), $\widehat{\mathbf{H}} \cdot \mathbf{k}$ must be equal to zero.

Next, we can limit ourselves to harmonic time dependence, meaning that we consider only the spatial field profiles for a certain frequency, which are then referred to as harmonic modes:

[2] Magnetic monopoles may exist under very special circumstances [14] – but those circumstances are exotic enough that we can reasonably neglect their existence here.

$$\mathbf{E}(\mathbf{r},t) = \mathbf{E}(\mathbf{r})\exp(-i\omega t), \tag{11}$$

$$\mathbf{H}(\mathbf{r},t) = \mathbf{H}(\mathbf{r})\exp(-i\omega t). \tag{12}$$

We will generally assume such harmonic modes and not write the time-dependence explicitly. With this, we can easily evaluate the time derivatives in Maxwell's equations, so Eq. (7) and (8) become

$$\boldsymbol{\nabla}\times\mathbf{E}(\mathbf{r}) = i\omega\mu_0\mathbf{H}(\mathbf{r}), \tag{13}$$

$$\boldsymbol{\nabla}\times\mathbf{H}(\mathbf{r}) = -i\omega\varepsilon_0\varepsilon_r(\mathbf{r})\mathbf{E}(\mathbf{r}). \tag{14}$$

Upon taking the curl of one of these equations and plugging the other one in, we obtain the two equations

$$\boldsymbol{\nabla}\times\boldsymbol{\nabla}\times\mathbf{E}(\mathbf{r}) = \left(\frac{\omega}{c}\right)^2\varepsilon_r(\mathbf{r})\mathbf{E}(\mathbf{r}), \tag{15}$$

$$\boldsymbol{\nabla}\times\left(\frac{1}{\varepsilon_r(\mathbf{r})}\boldsymbol{\nabla}\times\mathbf{H}(\mathbf{r})\right) = \left(\frac{\omega}{c}\right)^2\mathbf{H}(\mathbf{r}), \tag{16}$$

where $c = 1/\sqrt{\mu_0\varepsilon_0}$ is the vacuum speed of light. These equations, in combination with the appropriate set of boundary conditions, now represent eigenvalue problems. They can be solved in order to obtain the spatial field distributions. After solving for either the H- or the E-field, the other field component can easily be obtained from Eq. (13) or (14), respectively. For non-magnetic materials, typically the equation for the magnetic field is solved. Then the divergence condition for the H-field imposed by Eq. (10) is rather simple as it does not depend on ε_r. On the other hand, the divergence condition for the E-field is automatically fulfilled: Rearranging Eq. (14) gives $\mathbf{E}(\mathbf{r}) = i\big(\omega\varepsilon_0\varepsilon_r(\mathbf{r})\big)^{-1}\boldsymbol{\nabla}\times\mathbf{H}(\mathbf{r})$, where Eq. (9), $\boldsymbol{\nabla}\cdot\varepsilon_r(\mathbf{r})\mathbf{E}(\mathbf{r},t) = 0$, is trivially fulfilled since the divergence of a curl is always zero.

2.1.1 Scale invariance of Maxwell's equations

One very important property of Maxwell's equations is their scale invariance. Assume that the permittivity distribution is scaled by a factor of s, then the new permittivity distribution is obtained by scaling the argument, $\varepsilon_r'(\mathbf{r}) = \varepsilon_r(\mathbf{r}/s)$. We can then define the displacement vector of the scaled distribution as $\mathbf{r}' = s\mathbf{r}$. This leads to an inverse scaling of the nabla operator, $\boldsymbol{\nabla}' = \boldsymbol{\nabla}/s$, as it contains the inversions of all components of $\mathbf{r}$. If we substitute all the scaled quantities into Eq. (16) we get

$$s\nabla' \times \left(\frac{1}{\varepsilon_r(\mathbf{r}'/s)} s\nabla' \times \mathbf{H}(\mathbf{r}'/s) \right) = \left(\frac{\omega}{c}\right)^2 \mathbf{H}(\mathbf{r}'/s), \tag{17}$$

where we now use that $\varepsilon_r(\mathbf{r}'/s) = \varepsilon_r'(\mathbf{r}')$, and we may equivalently define $\mathbf{H}(\mathbf{r}'/s) = \mathbf{H}'(\mathbf{r}')$. Then Eq. (17) turns out to be of the same form as Eq. (16):

$$\nabla' \times \left(\frac{1}{\varepsilon_r'(\mathbf{r}')} \nabla' \times \mathbf{H}'(\mathbf{r}') \right) = \left(\frac{\omega}{sc}\right)^2 \mathbf{H}'(\mathbf{r}'). \tag{18}$$

Expanding or compressing the permittivity distribution by a factor s therefore leads to an equivalently expanded or compressed field distribution at a frequency scaled inversely by the same factor s. This property is highly relevant for the topic of structural colors that will be discussed later in this work. It allows changing the color impression just by scaling the underlying structure, which is one of the main advantages of structural colors compared to traditional pigment colors.

2.1.2 Relative permittivity vs. refractive index

In the Maxwell equations materials are typically described by their relative permittivity. However, in the field of optics it is common to qualify materials by their refractive index n. For a homogeneous medium, n relates the propagation speed of light in the medium to the speed of light in free space, $c = c_0/n$. Throughout this work, we will mostly use n but sometimes switch to permittivity where it is more convenient. Therefore, the relation between the two quantities will briefly be discussed here. Note, that we continue to use the simplifications stated before, i.e., we only deal with linear, lossless, isotropic, non-dispersive and non-magnetic materials.

The refractive index is generally defined as $n = \sqrt{\varepsilon_r \mu_r}$ [15]. For non-magnetic materials we thus get the simple relation $n^2 = \varepsilon_r$. An arbitrary distribution of the refractive index in space may be described as $n(\mathbf{r}) = \bar{n} + \Delta n(\mathbf{r})$, where $\bar{n}$ denotes the average refractive index and $\Delta n(\mathbf{r})$ describes a spatially varying perturbation. If the same structure is to be described in terms of relative permittivity and $\Delta n(\mathbf{r})$ is small, we may define

$$\varepsilon_r(\mathbf{r}) = \bar{\varepsilon}_r + \Delta\varepsilon_r(\mathbf{r}) = \left(\bar{n} + \Delta n(\mathbf{r})\right)^2 \approx \bar{\varepsilon}_r + 2\bar{n}\Delta n(\mathbf{r}), \tag{19}$$

where the second-order term in Δn is ignored as it is negligibly small. Using this notation, the permittivity perturbation can thus be described by $\Delta\varepsilon_r(\mathbf{r}) = 2\bar{n}\Delta n(\mathbf{r})$.

2.1.3 Perturbation theory

The rearranged Maxwell's equations above provide a viable route to obtain the field distribution for arbitrary distributions $\varepsilon_r(\mathbf{r})$. However, they have to be solved for every frequency or every realization of $\varepsilon_r(\mathbf{r})$ individually. Perturbation theory gives us a tool to find the solutions for slightly changed parameters – given, that the solution of the original problem is known – without having to recalculate the whole problem. This includes changes like small nonlinearities or small absorption, which could make the eigenvalue problem considerably more difficult to solve. We will here only discuss the specific case of a small change in $\varepsilon_r(\mathbf{r})$, but the theory is in principle applicable for many kinds of eigenvalue problems. The basics of the theory can be found, e.g., in reference [16]. Since perturbation theory is commonly derived for quantum mechanical problems, we will use bra-ket notation in this discussion. A comprehensive introduction to bra-ket notation is again given in reference [16].

Let us start by rewriting Eq. (15) in a way that clearly shows its eigenvalue problem nature [17]:

$$\hat{O}_1|E\rangle = \frac{\omega^2}{c^2}\hat{O}_2|E\rangle, \tag{20}$$

where $\hat{O}_1 = \boldsymbol{\nabla}\times\boldsymbol{\nabla}\times$ and $\hat{O}_2 = \varepsilon_r(\mathbf{r})$ represent two operators, $|E\rangle$ is the eigenvector, which in this case is the field distribution $\mathbf{E}(\mathbf{r})$, and $(\omega/c)^2$ is the eigenvalue. Such a problem, with operators on both sides of the equation, is called a generalized eigenvector problem [17]. Furthermore, the eigenstates, or modes, are defined in such a way that they are orthogonal, i.e., their inner product $\langle E^{(0)}|E^{(n>0)}\rangle = 0$. Also, the unperturbed solution is assumed to be known and fulfills

$$\hat{O}_1|E^{(0)}\rangle = \frac{{\omega^{(0)}}^2}{c^2}\hat{O}_2|E^{(0)}\rangle, \tag{21}$$

where $|E^{(0)}\rangle$ and $\omega^{(0)}$ are the unperturbed eigenvector and eigenvalue. Now the permittivity distribution, and therefore the operator $\hat{O}_2$, is slightly varied such that $\hat{O}_2' = \bar{\varepsilon}_r + \Delta\varepsilon_r(\mathbf{r})$, where $\Delta\varepsilon_r(\mathbf{r})$ is the weak perturbation. To find the solution for the perturbed system, the eigenvalues as well as the eigenvectors (or eigenmodes) are expanded in powers of the perturbation [17]:

$$\omega = \omega^{(0)} + \omega^{(1)} + \omega^{(2)} + \cdots, \tag{22}$$

$$|E\rangle = |E^{(0)}\rangle + |E^{(1)}\rangle + |E^{(2)}\rangle + \cdots, \tag{23}$$

where the superscripts (n) denote the n-th order of approximation which is proportional to $\Delta\varepsilon_r^n$. We will from now on neglect all terms proportional to $\Delta\varepsilon_r^n$ with $n \geq 2$ as they are approximately zero. Inserting the series expansions into the eigenvalue problem we get

$$\hat{O}_1\left(|E^{(0)}\rangle + |E^{(1)}\rangle\right) = \frac{\bar{\varepsilon}_r + \Delta\varepsilon_r}{c^2}\left(\omega^{(0)} + \omega^{(1)}\right)^2 \cdot \left(|E^{(0)}\rangle + |E^{(1)}\rangle\right). \tag{24}$$

Expanding all the terms on the right side, again neglecting all the higher order terms that form in the process, and using the linearity of $\hat{O}_1$ we can write

$$\begin{aligned}\hat{O}_1\left(|E^{(0)}\rangle\right) + \hat{O}_1\left(|E^{(1)}\rangle\right) = \frac{1}{c^2}\Big(&{\omega^{(0)}}^2\bar{\varepsilon}_r|E^{(0)}\rangle + 2\omega^{(0)}\omega^{(1)}\bar{\varepsilon}_r|E^{(0)}\rangle \\ &+ {\omega^{(0)}}^2\bar{\varepsilon}_r|E^{(1)}\rangle + {\omega^{(0)}}^2\Delta\varepsilon_r|E^{(0)}\rangle\Big).\end{aligned} \tag{25}$$

We find that the leftmost terms on both sides of the equation are nothing else but the unperturbed eigenvalue equation (Eq. (20)), so they cancel out. Then we left-multiply the bra $\langle E^{(0)}|$, canceling all the $|E^{(1)}\rangle$-terms due to the mode orthogonality, rearrange the remaining equation for $\omega^{(1)}$ and write out the inner products [17]:

$$\Delta\omega \approx \omega^{(1)} = -\frac{\omega^{(0)}}{2}\frac{\langle E^{(0)}|\Delta\varepsilon_r|E^{(0)}\rangle}{\langle E^{(0)}|\bar{\varepsilon}_r|E^{(0)}\rangle} = -\frac{\omega}{2}\frac{\int_V \Delta\varepsilon_r(\mathbf{r})|\mathbf{E}(\mathbf{r})|^2 d\mathbf{r}^3}{\int_V \bar{\varepsilon}_r|\mathbf{E}(\mathbf{r})|^2 d\mathbf{r}^3}. \tag{26}$$

This equation can be used, e.g., to calculate the bandgap opening of a low-contrast photonic crystal, which will be discussed in later chapters.

2.2 A scattering landscape

A major part of this work will be concerned with the redirection of electromagnetic waves – reflection, refraction, scattering. Depending on the size, shape and material of the scatterer, light-matter interaction can be dominated by entirely different laws. In fact, the landscape of scattering is so complex and diverse that it is difficult to find comprehensive literature on the topic. We will try to give a very brief overview of the most important phenomena that form the boundaries for the effects discussed in the later chapters. This explicitly excludes the full range of inelastic scattering effects, like Raman scattering or Brillouin scattering.

For macroscopic structures, reflections and refractions at plane interfaces dominate. This includes the well-known effects occurring at plane dielectric interfaces described by Snell's law and the Fresnel equations. Take an electromagnetic plane wave that is traveling in a homogeneous medium of refractive index n_1. This wave is incident on a

planar interface towards another homogeneous medium of refractive index n_2 under an angle α_1 to the surface normal. In this case, the reflected wave will propagate under the same angle α_1 to the surface normal, but with its k-vector mirrored at the material interface, while the refracted wave's propagation angle, α_2, is described by Snell's law [18],

$$n_1 \sin \alpha_1 = n_2 \sin \alpha_2. \tag{27}$$

The most striking consequence of Snell's law is that for light coming from the medium of higher refractive index a limit angle exists, at which the refracted wave no more propagates away from the interface (α_2 becomes 90°). This angle,

$$\alpha_c = \arcsin\left(\frac{n_2}{n_1}\right), \tag{28}$$

is called critical angle or angle of total internal reflection.

The field strengths or powers of the reflected or refracted light are described by the Fresnel equations and depend on the polarization of the incident light. The plane in which the incident, reflected and refracted wave's k-vectors lie is called plane of incidence. Incident light with its electric field component orthogonal to this plane is called s-polarized, while light with the E-field component inside the plane of incidence is called p-polarized. The reflected power for s-polarized light is

$$R_s = \left|\frac{n_1 \cos \alpha_1 - n_2 \cos \alpha_2}{n_1 \cos \alpha_1 + n_2 \cos \alpha_2}\right|^2 \tag{29}$$

and for p-polarized light

$$R_p = \left|\frac{n_2 \cos \alpha_1 - n_1 \cos \alpha_2}{n_2 \cos \alpha_1 + n_1 \cos \alpha_2}\right|^2. \tag{30}$$

For lossless media, energy conservation requires that the factor for the transmitted power is simply $T_i = 1 - R_i, i \in \{s, p\}$. [18]

However, even at seemingly macroscopic interfaces the microscopic texture can have a strong influence on the appearance of an object. While perfectly flat materials appear shiny and give rise to strong specular reflection, rough interfaces can redirect light in all directions, giving the material a matte appearance. Also, the notion of a homogeneous material already implies another limiting case, that of the effective medium. Since every material is structured at least on the atomic or molecular level, a truly homogeneous medium cannot exist. However, when the structure of the medium is much finer than the

wavelength of the light propagating therein – which is typically the case for an optical wave propagating inside a material – the wave will not resolve the atomic structure. It will instead behave as if it were propagating in a homogeneous medium with effective material parameters depending on the fine structure's constituents and their prevalence [19]. There are very elaborate effective medium approximations like the Bruggeman formula or the Maxwell Garnett mixing rule, but all such approaches are approximations which only yield precise results for specific kinds of media. E.g., the Maxwell Garnett rule is only applicable for a small volume fraction of spherical inclusions in a host matrix [20]. For the purposes of this thesis, where we will focus on geometrically complex structures with very small refractive-index contrasts, we deemed it sufficient to simply use the arithmetic mean of the composing refractive indices as the effective refractive index, wherever effective parameters are needed.

The scattering of spherical particles is described by the Mie theory. While the full theory is quite unwieldy, for very small or very large relative particle sizes different approximations can be used. For dilute distributions of dielectric particles much smaller than the wavelength, light scattering can be well approximated by Rayleigh scattering. The incident wave excites a dipole moment inside the particles which acts like an antenna and emits light with a typical Hertzian dipole characteristic. This kind of scattering is highly frequency-selective: The scattered power is proportional to the fourth power of the frequency. For that reason, short-wavelength blue light gets considerably more strongly scattered than longer-wavelength red light. This leads to a very peculiar effect we can observe in our everyday life: the color of the sky. On a clear day, the sky looks mostly blue due to the strongly frequency-dependent scattering of the light traversing the atmosphere of Earth. The sun itself, in contrast, looks slightly yellow due to the blue light being scattered out of the direct light path. During sunset this effect is even more pronounced as the way the sun's light travels through the atmosphere becomes longer due to its oblique angle[3]. [21]

When the particle sizes are similar to the wavelength, intra-particle resonances start playing a role. The full Mie theory is needed to describe these cases and leads to very complex scattering patterns and frequency dependencies. Due to this, it is of high importance for the description of particle-based structural colors [22] as well as the optimization of particle sizes in traditional colors [11]. For large spherical particles with higher contrast, e.g. raindrops, geometrical optics can be applied. [21]

[3] The sky surrounding the sun may appear in long-wavelength colors as well, but this is due to less frequency-selective scattering by larger particles that just pass on the remaining, red-tinted sunlight.

An approximate treatment is also possible for weakly scattering particles. The weak scattering condition is usually formulated by the conditions [21]

$$\left|\frac{n_1}{n_2} - 1\right| \ll 1, \tag{31}$$

$$2ka\left|\frac{n_1}{n_2} - 1\right| \ll 1, \tag{32}$$

where n_1 and n_2 are the refractive indices of the particle and its surrounding medium, k is the wave number of the wave under investigation and a is the length-scale of the particle. These conditions allow the assumption that the incident field is basically undisturbed by the presence of the particle. Then, all volume elements inside the particle can be seen as independent Rayleigh scatterers which coherently superpose to form a total scattered field. This approach is known as the Rayleigh-Gans approximation in light scattering, or as the Born approximation in quantum mechanics. As we will revisit the conditions in the context of the Ewald sphere construction, which is typically used for X-ray scattering on a molecular level, we will herein use the term Born approximation. [21]

Everything we discussed in this chapter so far were descriptions of single scattering processes. However, many of our everyday observations are based on multiple, or diffuse, scattering. Things like clouds, milk, or teeth, all get their white, opaque appearance from light that is redirected several times, making it difficult for an observer to reconstruct the scenery behind or inside of them. For such diffuse scattering, it is very difficult to exactly calculate the overall light scattering as samples typically contain a large number of scatterers which are randomly arranged and, in many cases, moving with time. Rather accurate statistical predictions can be made, though. The most important terms in the context of diffuse scattering are the scattering mean free path and the transport mean free path. The former describes the average path length a photon travels inside the structure between two scattering events, and the latter describes the average path until the directional information of a photon is lost. The two quantities are connected by a term that depends on the isotropy of the individual scattering events, for perfectly isotropic scattering they are equal. Based on these quantities, statistical approaches like diffusion theory or Monte Carlo ray tracing [23] can be used to describe the light scattering. It can roughly be said that these approaches should be utilized when a disordered sample reaches a thickness on the order of the transport mean free path or scattering mean free path, correspondingly. [19]

This concludes the overview of the most basic effects traditionally discussed in the context of light scattering. The reader may have noted that there is a clear focus on spherical

particles in disordered assemblies. The focus of this work, however, is on network-like, partially ordered structures where most of the effects presented above apply only very loosely. Also, we will mostly discuss either single scattering or constructive interference, so diffusion will only appear as a detrimental effect. Finally, the effects we will discuss appear when the light wavelengths are comparable to the length scales of the scatterer. Here, the type of scattering strongly depends on the fine structure of the material, as interference effects can play a major role. The effects observed in different kinds of ordered structures are discussed in the next chapter.

2.3 Photonic structures

In this chapter, we will give an overview of different photonic structures, organized by their degree of disorder. Starting with photonic crystals, which have long-range order and perfect translational symmetry, we will afterwards introduce quasicrystals, which still have long-range order but without translational symmetry. The third part will cover photonic structures that are disordered apart from a short-range order that can, e.g., come from equal average distances between the building blocks of the structure. Finally, the fourth chapter will give a brief primer on the common properties of the quasiperiodic model structures used in this work.

2.3.1 Photonic crystals

Research on photonic crystals started after in 1987 E. Yablonovitch realized that structures ordered on length scales similar to the wavelength of light can have a similar effect on photons as atomic crystals have on electrons [24]. One of the most striking parallels between photonic crystals and their atomic counterparts is the opening of a bandgap. For the case of electrons in atomic crystals, the bandgap is an energy range where no electron states can exist. If the bandgap position overlaps with the energy levels for free electrons that would be required for charge transfer, the electrical conductivity of the crystal becomes practically zero. For photonic crystals, the bandgap is a range of light frequencies for which no propagating modes can exist in the photonic crystal. Thus, at these frequencies light transport through the photonic crystals comes to a halt. This finding led to previously unprecedented degrees of control over the flow and emission of light.

Photonic crystals are, in general, dielectric structures on the length scale of the wavelength of light, which consist of an endless repetition of equal unit cells:

$$\varepsilon(\mathbf{r}) = \varepsilon(\mathbf{r} + \mathbf{R}), \tag{33}$$

where $\mathbf{R}$ is the translation vector between unit cells. $\mathbf{R}$ represents all possible linear combinations of integer multiples of the fundamental unit cell vectors, i.e., $\mathbf{R} = u_1\mathbf{a}_1 + u_2\mathbf{a}_2 + u_3\mathbf{a}_3$, where u_i are said integers and $\mathbf{a}_i$ are the primitive lattice vectors. For two- or one-dimensional photonic crystals, two or one basis vectors are sufficient, correspondingly. An example of a 2D lattice, its unit cell and unit vectors is shown in Fig. 1A and B.

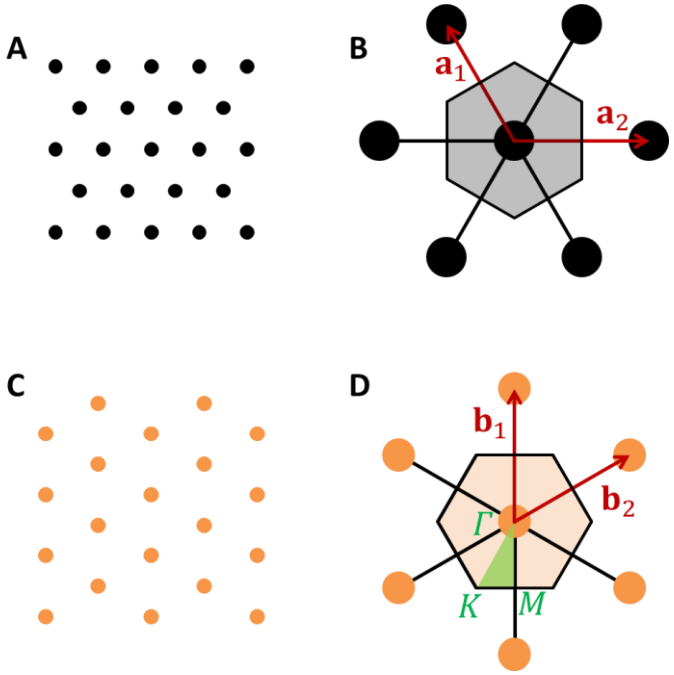


Fig. 1. Some important aspects of real and reciprocal lattices illustrated for the 2D hexagonal lattice. A: Depiction of the hexagonal 2D lattice in real space. B: Zoom into the lattice. A possible choice of the unit vectors $\mathbf{a}_1$ and $\mathbf{a}_2$ is shown in red. The grey shaded area represents the smallest unit cell, the Wigner-Seitz cell. C: Depiction of the reciprocal lattice of the hexagonal lattice in A. The size is scaled arbitrarily for visualization. The reciprocal lattice of a hexagonal lattice is again hexagonal. D: Zoom into the reciprocal lattice. The unit vectors $\mathbf{b}_1$ and $\mathbf{b}_2$ are again highlighted in red. The orange shaded area represents the Brillouin zone. The green shaded area represents the irreducible Brillouin zone. The characteristic points for the hexagonal Brillouin zone are Γ in the origin, M in the center of the edge, and K at the corner formed by the intersection of two edges [25].

Looking at the Fourier transform of the permittivity and exploiting its periodicity we find

$$\varepsilon(\mathbf{r}) = \int \mathcal{E}(\mathbf{k}) e^{i\mathbf{r}\cdot\mathbf{k}} d\mathbf{k}^3 = \varepsilon(\mathbf{r} + \mathbf{R}) = \int \mathcal{E}(\mathbf{k}) e^{i\mathbf{R}\cdot\mathbf{k}} e^{i\mathbf{r}\cdot\mathbf{k}} d\mathbf{k}^3, \tag{34}$$

so $\mathcal{E}(\mathbf{k})$ must be equal to $\mathcal{E}(\mathbf{k})e^{i\mathbf{R}\cdot\mathbf{k}}$. This is only true for $\mathcal{E}(\mathbf{k}) = 0$ or $\mathbf{R}\cdot\mathbf{k} = 2\pi N$ with $N \in \mathbb{Z}$, showing that the Fourier transform is zero except for certain spots which are again periodic. These spots form the reciprocal lattice. As the reciprocal lattice can experimentally be obtained from measuring the Bragg scattering of the crystal, the spots are also referred to as Bragg peaks. The lattice points in 3D are typically denoted as $\mathbf{G} = v_1\mathbf{b}_1 + v_2\mathbf{b}_2 + v_3\mathbf{b}_3$, where v_i are again integer multipliers and $\mathbf{b}_i$ are the primitive reciprocal lattice vectors (see Fig. 1C and D). The primitive vectors of the real and reciprocal lattice are connected as $\mathbf{a}_i \cdot \mathbf{b}_j = 2\pi\delta_{ij}$, where δ_{ij} denotes the Kronecker delta, which equals one if $i = j$ and zero otherwise. Then $\mathbf{R}\cdot\mathbf{G} = 2\pi N$, where N is again an integer. [25]

The periodicity in the permittivity imposes some strict limitations on the field distribution inside the photonic crystal. Since the individual unit cells in an infinite crystal are all exactly equal and can therefore not be distinguished, the field modes inside them can only be different by a phase factor. Mathematically, this can be seen by looking at the operators for the fields on the one hand, and for the periodicity on the other hand. The periodicity of the system can be expressed as an operator $\hat{T}\varepsilon(\mathbf{r}) = \varepsilon(\mathbf{r}+\mathbf{R})$. The field operator is the one on the left-hand side of Eq. (16), $\hat{O}_{\mathbf{H}} = \boldsymbol{\nabla}\times\left(1/\varepsilon_r(\mathbf{r})\right)\boldsymbol{\nabla}\times$. Due to the periodicity of the system it does not matter if the field operator is applied or if the coordinates are shifted by the translation operator, then the field operator is applied, and then the coordinates are shifted back:

$$\hat{O}_{\mathbf{H}} = \hat{T}^{-1}\hat{O}_{\mathbf{H}}\hat{T}. \tag{35}$$

In the language of quantum mechanics these operators are said to commute, which entails the property that they share the same eigenvectors. This is very convenient, as the eigenvectors of the translation operator are typically more easily found than those of the field operator. According to Bloch's theorem the eigenfunctions of the translation operator have the form $\mathbf{u}_{\mathbf{k}}(\mathbf{r})e^{i\mathbf{r}\cdot\mathbf{k}}$, where $\mathbf{u}_{\mathbf{k}}(\mathbf{r})$ is a function that is again periodic with $\mathbf{R}$, $\mathbf{u}_{\mathbf{k}}(\mathbf{r}+\mathbf{R}) = \mathbf{u}_{\mathbf{k}}(\mathbf{r})$. This can easily be checked:

$$\hat{T}\mathbf{u}_{\mathbf{k}}(\mathbf{r})e^{i\mathbf{r}\cdot\mathbf{k}} = \mathbf{u}_{\mathbf{k}}(\mathbf{r}+\mathbf{R})e^{i(\mathbf{r}+\mathbf{R})\cdot\mathbf{k}} = e^{i\mathbf{R}\cdot\mathbf{k}}\mathbf{u}_{\mathbf{k}}(\mathbf{r})e^{i\mathbf{r}\cdot\mathbf{k}}, \tag{36}$$

which again takes the form of an eigenvalue problem with eigenvalues $e^{i\mathbf{R}\cdot\mathbf{k}}$. With this, we now know the form of the magnetic field modes,

$$\mathbf{H}_{\mathbf{k}}(\mathbf{r}) = \mathbf{u}_{\mathbf{k}}(\mathbf{r})e^{i\mathbf{r}\cdot\mathbf{k}}, \tag{37}$$

and we know that they are invariant up to a phase factor under translation by a lattice vector in real space. Moreover, when the field mode is shifted by $\mathbf{G}$ in reciprocal space,

$$\hat{T}\mathbf{H}_{\mathbf{k+G}}(\mathbf{r}) = \mathbf{u}_{\mathbf{k+G}}(\mathbf{r}+\mathbf{R})e^{i(\mathbf{r}+\mathbf{R})\cdot(\mathbf{k}+\mathbf{G})} = e^{i\mathbf{R}\cdot\mathbf{G}}e^{i\mathbf{R}\cdot\mathbf{k}}\mathbf{H}_{\mathbf{k+G}}(\mathbf{r}). \tag{38}$$

Since $\mathbf{R}\cdot\mathbf{G} = 2\pi N$ (and thus $e^{i\mathbf{R}\cdot\mathbf{G}} = 1$) the eigenvalues, and therefore the mode frequencies, are the same for $\mathbf{H}_{\mathbf{k}}(\mathbf{r})$ and $\mathbf{H}_{\mathbf{k+G}}(\mathbf{r})$. This means that all information about the mode frequencies can be obtained from a single unit cell in reciprocal space. This unit cell is the first Brillouin zone. Using similar arguments as above, it can be shown that rotational as well as mirror symmetries lead to additional redundancy, so the zone of k-vectors that need to be considered for a full description of the fields shrinks even further. The resulting volume (or area, in 2D) is the irreducible Brillouin zone (see Fig. 1D).

There is a very intuitive way to construct the Brillouin zone. After finding the reciprocal lattice, lines are drawn from the origin to all the neighboring lattice points. At the center of those lines an orthogonal plane (or line, in 2D) is drawn. The volume (area) that is bounded by these planes (lines) is the Brillouin zone. This is exactly analogous to the construction of the fundamental cell in real space, where it is called the Wigner-Seitz cell (see Fig. 1B). [25]

Photonic crystals are typically organized by their dimensionality, into 1D, 2D, and 3D photonic crystals. Probably *the* simplest photonic crystal is the Bragg mirror, which is a periodic arrangement of slabs of two or more different materials with a period a. Due to its simplicity, it is the ideal example structure to shed some light on the emergence of a photonic bandgap in photonic crystals.

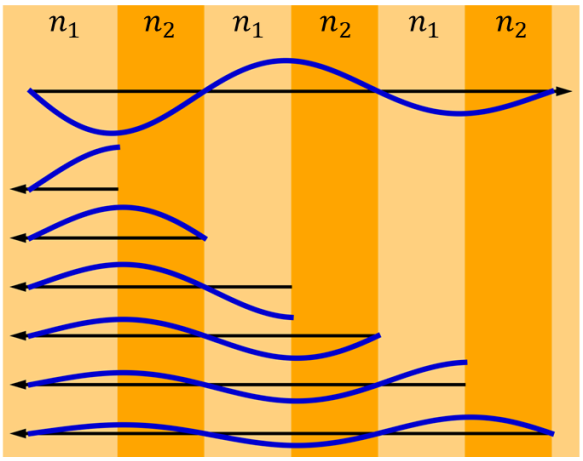


Fig. 2. Schematic depiction of a simple Bragg mirror and the Fresnel reflections at its material interfaces. The wave at the top depicts the incident wave, the ones below represent the reflected wave at the different material interfaces. For the refractive indices $n_2 > n_1$ holds, so that reflections at the n_1-n_2 boundary experience a phase shift of 180°. As a result, the reflections of the incident wave from all material interfaces interfere constructively while the incident wave decays exponentially.

The most intuitive way to find the optical transport properties of such a structure would be to first look at the interference of waves that are reflected at the slab interfaces (see Fig. 2). And in fact, this method will already yield interesting results. Assume, e.g., that the individual slab thicknesses of the Bragg mirror are one fourth of the material wavelength of the light. In that case, and considering the fact that there is a phase shift of 180° at the transition from the lower-refractive-index medium to the higher-refractive-index medium, the reflected and backward propagating light from all interfaces will be in phase. Therefore, the reflection will be very strong, while the transmission decreases exponentially. In fact, for an infinite thickness of the mirror, the reflection converges to 100% while the transmission drops to zero.

This simple situation is a first example of the behavior of light at a bandgap frequency in a photonic crystal. However, in analyzing more complex geometries this approach quickly becomes impractical. We will therefore use the band structure of photonic crystals, which is closely related to the band diagram for semiconductors, to describe the light propagation properties. Returning to the Bloch mode representation of the H-fields (Eq. (37)) and plugging it into the eigenvalue problem we get

$$\hat{O}_{\mathbf{H}}\mathbf{u}_{\mathbf{k}}(\mathbf{r})e^{i\mathbf{r}\cdot\mathbf{k}} = \boldsymbol{\nabla}\times\left(\frac{1}{\varepsilon_r(\mathbf{r})}\boldsymbol{\nabla}\times\mathbf{u}_{\mathbf{k}}(\mathbf{r})e^{i\mathbf{r}\cdot\mathbf{k}}\right) = \left(\frac{\omega(\mathbf{k})}{c}\right)^2\mathbf{u}_{\mathbf{k}}(\mathbf{r})e^{i\mathbf{r}\cdot\mathbf{k}}, \tag{39}$$

where the dependence of the mode frequency on the wave vector is now explicitly written. This equation can be rewritten for $\mathbf{u}_{\mathbf{k}}(\mathbf{r})$ by carrying out the derivatives of $e^{i\mathbf{r}\cdot\mathbf{k}}$ in the operator on the left-hand side and afterwards cancelling the $e^{i\mathbf{r}\cdot\mathbf{k}}$ out. We then obtain the expression

$$(i\mathbf{k}+\boldsymbol{\nabla})\frac{1}{\varepsilon_r(\mathbf{r})}(i\mathbf{k}+\boldsymbol{\nabla})\mathbf{u}_{\mathbf{k}}(\mathbf{r}) = \hat{O}_{\mathbf{k}}\mathbf{u}_{\mathbf{k}}(\mathbf{r}) = \left(\frac{\omega(\mathbf{k})}{c}\right)^2\mathbf{u}_{\mathbf{k}}(\mathbf{r}). \tag{40}$$

This new eigenvalue problem can now be solved numerically to obtain the field profiles $\mathbf{u}_{\mathbf{k}}(\mathbf{r})$ and especially the eigenvalues $\omega(\mathbf{k})$. The eigenvalues are continuous functions of $\mathbf{k}$, but for each $\mathbf{k}$ there is a discretely spaced set of modes. The plot of $\omega(\mathbf{k})$ over $\mathbf{k}$ within the irreducible Brillouin zone is the standard form of a photonic band diagram.

To understand the emergence of the bandgap, imagine a situation where the materials constituting the Bragg mirror have the same refractive indices. In this situation, which corresponds to a homogeneous medium, the dispersion relation will simply be linear, $\omega(k) = ck/\bar{n}$ (Fig. 3A). We neglect the vectorial nature of the wave vector here as we look at a 1D case. For the frequency at the edge of the Brillouin zone, the period of the optical wave in the material equals twice the period of the Bragg mirror.

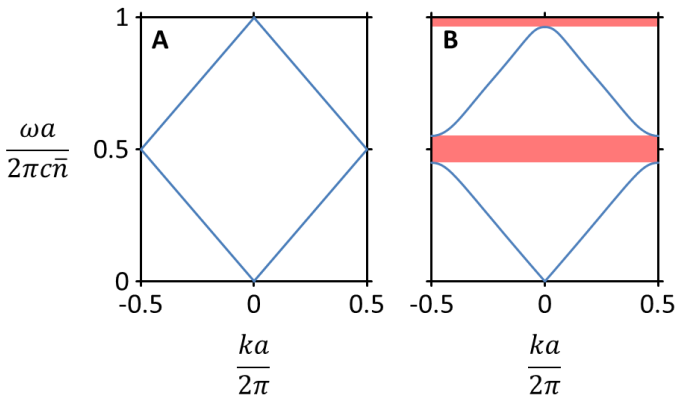


Fig. 3. Schematic band diagram of a simple Bragg mirror. The period of the Bragg mirror is a. In A the refractive indices of the media are the same, corresponding to a homogeneous medium. In B the refractive indices of the materials are different. The red shaded regions show the photonic bandgaps.

Now a small contrast in the refractive indices between the two materials is introduced. This leads to reflections at the material interfaces, as described above, which in the case of an infinitely extended structure superpose with the original wave to form a standing wave. In the band diagram this is represented by the slope of the dispersion relation, and therefore the group velocity $v_g = \partial\omega/\partial k$, converging to zero. There are now two distinct ways the fields of this standing wave can match the period of the Bragg mirror: The field extrema can be centered in either one or the other material. Due to the distinct refractive indices of the materials the effective refractive indices for the two field patterns differ. In consequence, the mode frequencies show a distinct separation as well, where the frequency range between them where no states exist is the bandgap (Fig. 3B). The state directly below the bandgap has its field maxima centered in the higher-refractive-index medium and is referred to as the dielectric band. The one directly above the bandgap has its maxima in the lower-refractive-index medium, which in many cases is air. It is therefore called the air band [1].

Moving towards two- and three-dimensional crystals, the Brillouin zone increases in dimensionality accordingly. As it becomes impractical to compute and plot the dispersion relation for the full areas or volumes, **k** is typically moved along the edges to the corners of the irreducible Brillouin zone, whereby the corners are given characteristic labels. As the extrema of the bands usually appear at the corners, this sufficiently represents the behavior of the crystal in most practical cases [1]. A comprehensive list of the Brillouin zones of typical crystal geometries and the labels for their corner points can be found in reference [26]. However, we are mostly going to use the nomenclature of the hexagonal lattice which is presented in Fig. 1D.

Staying with the example of the hexagonal lattice, the concepts introduced so far can easily be applied to the Γ-M edge (see Fig. 1D) by treating the crystal planes of the M-direction as a 1D crystal. Similarly, the behavior on the M-K edge can be understood by comparison to the Bragg scattering of a Bragg mirror (as in Fig. 2). As the angle towards the normal, θ, increases, the wavelength for which constructive interference and therefore the exponential suppression of the transmission is seen decreases as $\lambda = 2a\cos\theta$ according to Bragg's law [25]. The bandgap is consequently shifted to higher frequencies inversely proportionally to the cosine of the angle and thus proportionally to the length of the k-vector [9].

For most practical applications a directional bandgap is not sufficient; instead, structures should suppress light transport in all directions. For that, the different directional bandgaps need to overlap at least partly to form a frequency band where no states are found for any direction. We call such a frequency range an omnidirectional bandgap. If there is an omnidirectional bandgap even when all possible polarizations are considered, we call it complete. For the bandgap of the hexagonal lattice to persist in all directions the upper edge of its directional bandgap at the M-point needs to be above the lower edge at the K-point[4]. With the fixed geometry the only way to influence the overlap is by influencing the directional bandgap openings. And as the bandgap opening increases monotonously with the refractive-index contrast[5] this imposes a contrast minimum that is required for an omnidirectional or complete bandgap to open.

If the available refractive-index contrast is limited by the material choice, the only other option is to change the crystal geometry to one that has a more circular (2D) or spherical (3D) Brillouin zone. However, crystals are limited in their degree of symmetry by the crystallographic restriction theorem; the highest degree of rotational symmetry in 2D and 3D crystals is six [27]. With this restriction in place, the 2D crystal for which the Brillouin zone comes closest to a circle is the hexagonal lattice. The longest k-vector on the perimeter of the Brillouin zone at the K-point is by a factor $2/\sqrt{3}$ longer than the shortest one at the M-point, corresponding to a difference of about 15.5%. For 3D, the body-centered cubic (bcc) lattice in real space corresponds to the face-centered cubic (fcc) lattice in reciprocal space (and vice-versa). It therefore has the reciprocal lattice with the highest coordination number, i.e., the highest number of nearest-neighbor lattice sites of 12. However, the relative difference between the characteristic point[6] closest to (N) and the one furthest from the origin (H) is 41.4%. The most spherical Brillouin zone is instead

[4] A very similar condition is discussed in detail in chapter 4.3 and visualized in Fig. 17B (page 60).
[5] This statement is not clearly proven here. An indication is given by Eq. (26) and further, more rigorous calculations are done in chapter 4.3.
[6] The labels of the characteristic points are again based on reference [26].

found for the fcc lattice. The coordination number for its reciprocal bcc lattice is only eight, but there are six additional lattice sites close enough to truncate the Brillouin zone further. As a result, the relative difference between the closest (L) and the furthest point (W) of the fcc Brillouin zone is 29.1% – the smallest value possible for a 3D crystal, albeit still significant. A way to overcome the symmetry limitations of crystals and improve the sphericity of the Brillouin zone is found in the utilization of quasicrystals. This concept will be further expanded upon in the following chapter and especially in chapter 4.

2.3.2 Photonic quasicrystals

Atomic quasicrystals were only discovered in the early 1980s, and D. Shechtman was awarded the Nobel Prize in 2011 for their discovery [28]. They were first found in aluminum metal alloys as a metastable phase occurring upon rapid cooling [29]. Quasicrystals for photonic applications have not been as exhaustively investigated as their fully periodic counterparts. Apart from their far more recent date of discovery, a part of the reason for this is that they share a large amount of properties with photonic crystals, focusing further research on the differences between the two. However, one of the advantages of quasicrystals is that they can have a high degree of rotational symmetry, giving them far more flexibility in the number and positions of their Bragg peaks. For structural colors, to get a homogeneous appearance of the color material, a number of Bragg peaks significantly higher than those possible in crystal lattices is needed. Also, the high sphericity of the (effective) Brillouin zone[7] required for the opening of complete bandgaps at low refractive-index contrasts is facilitated by the added flexibility.

Mathematically, quasicrystals are self-similar functions that fill a space of any dimensionality with a pattern that has long-range order but that does not exhibit periodic patterns, i.e., it does not have translational symmetry. To make sense of this definition, one can imagine a periodic 1D series of points with unit distance that is superposed by another 1D series in the same direction, but with a period that is an irrational number. In this case, all points in that full 1D space are uniquely defined and directly correlate to the point pattern at any other place, so there is clearly a long-range order. However, due to the irrationality of the ratio of the two series' periods there can never be a periodic pattern. [30]

[7] Strictly speaking, there is no Brillouin zone for quasicrystals as they are not periodic. However, an equivalent construction based on the most pronounced Bragg peaks is often used to understand the formation of bandgaps in quasicrystals. Such constructions are referred to as effective Brillouin zones or pseudo-Jones zones [9].

In a wider sense the term quasicrystal also encompasses quasicrystalline patterns that are not atomic arrangements. Such patterns were known before the actual discovery of a quasicrystalline material. They are based on or described by aperiodic tiling algorithms that use a limited set of geometric shapes to tile a space with no gaps. The resulting structures again have long-range order without exhibiting periodic patterns. The most famous example of such a tiling, based on only two different kinds of tiles, is the Penrose tiling, named after Roger Penrose who discovered it in 1974 [31]. Especially in Islamic culture such tilings have a long and rich history with examples of quasicrystalline geometries in architecture and written scripts dating back to medieval times [32].

The typical "modern" method for generating quasicrystal patterns is, however, based on the so-called cut-and-project method. The basis for this method is a periodic structure in a higher-dimensional space, e.g., to get the aforementioned 1D quasicrystals a periodic structure in at least two dimensions is needed. The periodic structure is then intersected with a generalized hyperplane with an irrational slope. All cutting points between the hyperplane and a certain volume around the lattice points of the periodic structure are then projected into the lower-dimensional space of the hyperplane to obtain the quasicrystal pattern. [30]

How can we determine the optical transport properties of quasiperiodic structures? Due to the absence of periodicity, and therefore, of a definable unit cell, band simulations as described in the previous chapter are impossible. Several methods exist that can be used to circumvent this problem; however, they all do not provide the rich information that a bandgap simulation in a single unit cell of a periodic structure can provide. One possibility is to not simulate the exact quasicrystal, but instead a periodic approximant. Since it is periodic, the approximant can again be investigated with the tools introduced in the previous chapter [33]. For large unit cells, the approximant can get close to the actual structure. But to get a perfect approximation, an infinitely large unit cell would be required. Also, with the size of the unit cell increasing, the computational effort for the bandgap simulation increases rapidly, limiting the maximum size of the unit cell and therefore the accuracy of the approximation [30]. Other common methods are based on finite excerpts of the quasiperiodic structures. By scaling the size of the excerpt, important conclusions, e.g., on the bandgap formation can be drawn [33]. We will use this approach in chapter 4. Finally, for structures with low refractive-index contrasts and small spatial extent one can use scattering approaches instead of focusing on bandgap properties. E.g., the first-order Born approximation can be used to understand the scattering and propagation of light in such structures. We expand on this topic in chapter 3.2.

2.3.3 Short-range ordered photonic structures

The opposite extreme to the ordered structures in crystalline materials is a gas-like state, in which the constituents are loosely floating in space, with the only limitation to their positions being that two parts cannot occupy the same place. Such structures would look nearly homogeneous in reciprocal space and their scattering response would be purely diffuse. However, even when we limit our scope to condensed materials there are several degrees of disorder. E.g., Lévy glasses are composed of particles which are strongly polydisperse in size. Due to this, they feature a broad distribution of scattering mean free paths [34]. Also, typical white colors are made from strongly scattering particles that are polydisperse either in size or in shape [22]. However, there are several examples for mostly disordered materials which still feature some kind of order.

One of the prime examples for such a structure is photonic glass, which is a randomly packed, dense assembly of monodisperse spheres. Such structures typically do not produce sharp peaks in reciprocal space, but instead, assuming a representative volume, they form a ring in 2D or a spherical shell in 3D. This indicates that they do have a specific length-scale, but due to their positional disorder they appear similar in all spatial directions. The specific length scale a, like the period in ordered structures, is inversely proportional to the radius K of the ring or the spherical shell in k-space, $a = 2\pi/K$. Interestingly, the ring or spherical shell is found to correspond to an effective period of the structure of approximately 80% of the sphere diameter d, $a \approx 0.8d$ [35]. The width of the ring is inversely proportional to the correlation length of the structure.

In typical photonic glasses Mie resonances in the spherical constituents dominate large parts of the scattering spectrum. It is an issue of active discussion, whether they are detrimental to the color saturation of photonic-glass structural colors, or if they can even be utilized to improve it, which also depends on the refractive-index contrast of the used materials [35, 36]. The impact of Mie resonances can be weakened by either inverting the structure such that the matrix has a higher refractive index than the particles, or by using core-shell particles which can also be fine-tuned to optimize the reflection spectrum [35].

Another interesting structure that is locally ordered, yet overall disordered, is the polycrystal, a structure composed from small, randomly assembled crystallites. As in photonic glasses, a sufficiently extended polycrystal can cover all spatial directions to become effectively isotropic. Its range of spatial order is simply given by the extension of the crystallites.

Short-range ordered structures have been found to share many of the properties of their more ordered counterparts. Typically, the ring or spherical shell they possess is not as sharp as the peaks found in ordered structures since the length-scale of their order is far

lower. However, due to their lack of crystal symmetry they are completely direction-independent, which can be advantageous in applications where an angle-dependence of the optical response is not desired. E.g., the structural colors that are discussed in this work are supposed to function as a replacement for traditional pigment colors which show no angle-dependence as well.

2.3.4 Model structure

Throughout this work we will use different model structures which are all based on the same generation scheme: Several 1D sinusoidal gratings are superposed mathematically to form a continuous 2D or 3D distribution of abstract values, which are then mapped onto a range of refractive indices. All gratings have equal periods a so their Bragg peaks all lie on a circle or sphere with radius $2\pi/a$ in reciprocal space. The resulting structures are very close to quasicrystals in the sense that they have long-range order but are not periodic at the same time. However, since they cannot be described by a tiling and do not show the corresponding dense distribution of Bragg peaks in reciprocal space they do not match the traditional definition of a quasicrystal [37]. Thus, we will more generally refer to them as quasiperiodic structures. The specific implementations will be discussed in the corresponding chapters.

The approach is similar to the dual-beam exposure technique [38–42] but with random phase shifts between different exposures in our case [43, 44]. This randomization allows us to draw important conclusions about the connection between the total refractive-index contrast and the refractive-index modulation of single gratings which will be used for analytical modeling.

In principle it is possible to make fully periodic structures following the same scheme [45]. The periodicity condition in real space can be broken down to the relation

$$L = a\sqrt{w_1^2 + w_2^2 + w_3^2}, \tag{41}$$

where the w_i are integers that describe the number of oscillations on the edges of the cubic structure for each dimension. This condition is much more tangible in reciprocal space, where it simply becomes

$$\frac{2\pi}{a} = \frac{2\pi}{L}\sqrt{w_1^2 + w_2^2 + w_3^2}\,. \tag{42}$$

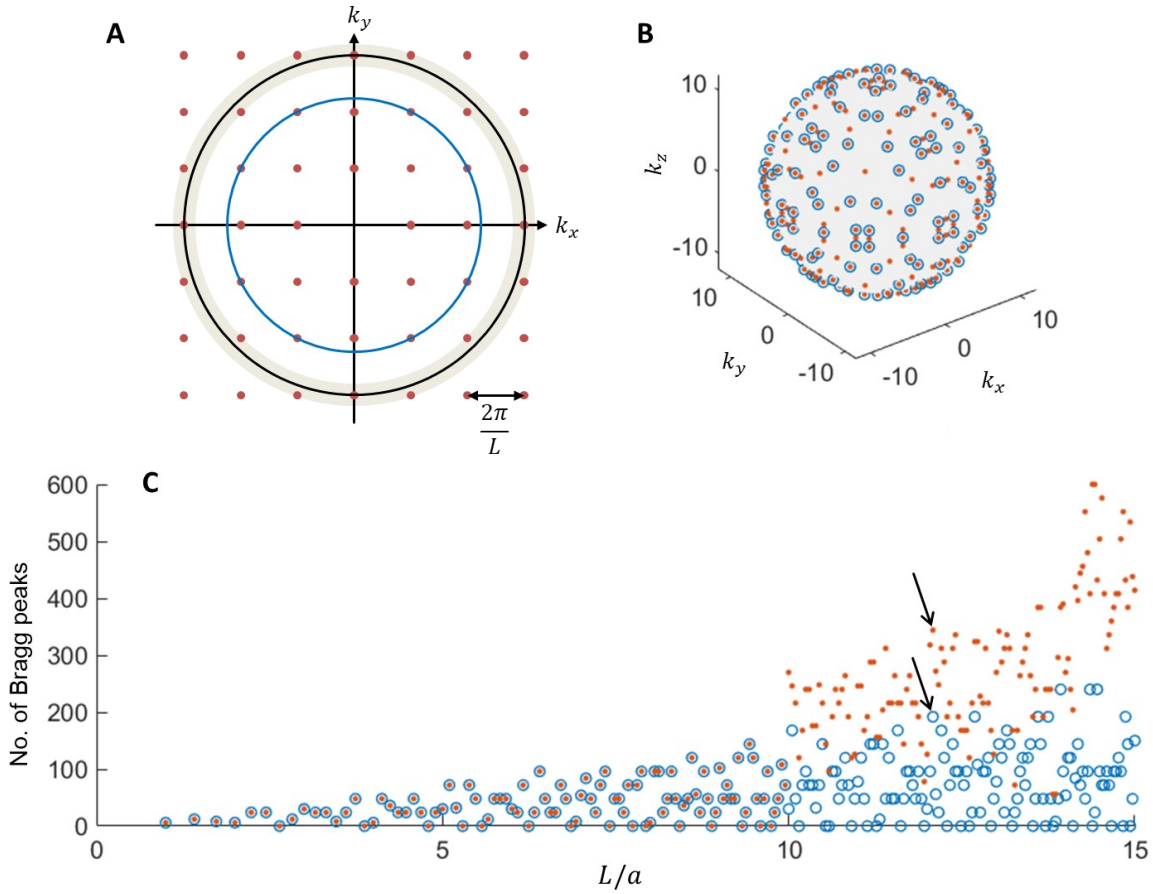


Fig. 4. Bragg peak distributions for periodic structures in 2D and 3D. A: Distributions for small relative structure sizes of $L/a = \sqrt{5}$ (blue circle) and $L/a = 3$ (black circle). The shadowed region around the black circle represents a possible tolerance window for the effective grating periods, which increases the number of Bragg peaks from four to 16. B: 3D distribution for $L/a = \sqrt{146} \approx 12$. The blue circles represent a structure where all grating periods are exactly equal, while the red dots correspond to one with a period tolerance of 1%. C: Number of Bragg peaks over the relative structure size. The blue circles and red dots correspond to the structure without and with period tolerance as in B. The black arrows show the structure size shown in B.

The right-hand side of this expression can be interpreted as spanning a grid of points with period $2\pi/L$. In this grid, a spherical shell of radius $2\pi/a$ is placed. The points where the spherical shell overlaps the grid points represent the Bragg peaks of the periodic gratings that can be placed inside the structure. The number of gratings is half of the overlapping points as the Bragg peaks of each grating are mirrored at the origin. A 2D example of this overlap is shown as the blue circle in Fig. 4A. In this example the w_i can be any combination of ± 1 and ± 2, yielding a total sphere radius of $2\pi/a = 2\pi\sqrt{5}/L$, or equivalently a relative structure size of $L/a = \sqrt{5}$. An example in 3D is shown by the blue circles in Fig. 4B. The relative structure size here is $L/a = \sqrt{146}$. By increasing L/a higher

numbers of overlaps become possible, but as shown in Fig. 4C for the 3D case, the function is by no means monotonous. The distribution of Bragg peaks obtained by this method is also strongly inhomogeneous.

A way to approach the problem of the inhomogeneous distribution is to allow not only gratings exactly on the $2\pi/a$-shell but also ones close to it. By this, unequal periods are allowed for the gratings. The result is a periodic approximant as already briefly introduced in chapter 2.3.2. An example is shown as the black circle in Fig. 4A. While the circle itself only intersects four points, allowing the shadowed region in addition this number is raised to 16. For the 3D example in Fig. 4B and C the red points indicate the periodic Bragg peaks when allowing a deviation of $\pm 1\%$ around $2\pi/a$. It can be seen that this does indeed add Bragg peaks in some of the obvious gaps in the distribution of the ideal structure. However, the resulting distribution remains highly inhomogeneous and now has the added drawback of allowing other grating periods, both of which are not compatible with the applications we are discussing within this work. We will therefore only consider truly quasiperiodic structures.

2.4 FIT simulations

All numerical simulations shown in this work were conducted using the time-domain solver of CST Studio Suite, which is now part of Dassault Systemes' SIMULIA package [46]. The software uses the Finite Integration Technique (FIT), the functionality of which will briefly be summarized in this chapter. All information presented here is based on the software documentation as well as the introductory papers by T. Weiland, the founder of the method [47, 48]. The specific applications of the software to the problems discussed in this work are described in more detail in the corresponding sections.

As for all field solvers, the objective of FIT is to solve Maxwell's equations for a given geometry. In contrast to the commonly used Finite Difference Time-Domain (FDTD) method, which is based on Maxwell's equations in their differential form, FIT uses their integral form:

$$\oint_{\partial A} \mathbf{E} d\mathbf{s} = -\iint_{A} \frac{\partial \mathbf{B}}{\partial t} d\mathbf{A}, \tag{43}$$

$$\oint_{\partial A} \mathbf{H} d\mathbf{s} = \iint_{A} \left(\frac{\partial \mathbf{D}}{\partial t} + \mathbf{J} \right) d\mathbf{A}, \tag{44}$$

$$\oiint_{\partial V} \mathbf{B} d\mathbf{A} = 0, \tag{45}$$

$$\oiint_{\partial V} \mathbf{D} d\mathbf{A} = \iiint_{V} \rho d\mathbf{V}. \tag{46}$$

The simulation domain is then discretized on a system of two intersecting grids, i.e., a Yee grid [49]. Such a setup for a single cell of the grating is shown in Fig. 5. On the edges of the primary grid, the electric fields as well as their influence on the magnetic flux are evaluated, while the magnetic fields and the electric flux are evaluated on the dual grid.

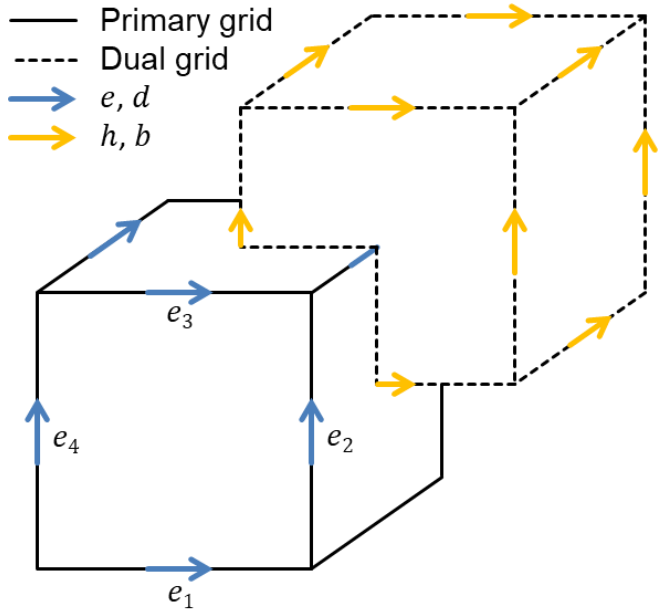


Fig. 5. Primary and dual grid used in the FIT method for one exemplary mesh cell. The electric fields are shown in blue. From one loop of E-fields, the magnetic flux can be found, from which then the magnetic field can be calculated. From one loop of magnetic fields, the electric flux and therefore the E-field can be calculated. This procedure is repeated throughout the mesh and throughout time to obtain the corresponding fields for the full simulation domain.

For each cell, Maxwell's equations can now be solved in a discretized form, e.g., for the front facet of the cell shown in Fig. 5, Eq. (43) would simplify to

$$e_1 + e_2 - e_3 - e_4 = (1 \quad 1 \quad -1 \quad -1) \begin{pmatrix} e_1 \\ e_2 \\ e_3 \\ e_4 \end{pmatrix} = -\frac{\partial}{\partial t} b. \tag{47}$$

Similarly to this, all of Maxwell's equations can be rewritten into their discretized form:

$$\mathbf{Ce} = -\frac{d}{dt}\mathbf{b}, \tag{48}$$

$$\tilde{\mathbf{C}}\mathbf{h} = \frac{d}{dt}\mathbf{d} + \mathbf{j}, \tag{49}$$

$$\tilde{\mathbf{S}}\mathbf{d} = \mathbf{q}, \tag{50}$$

$$\mathbf{Sb} = 0, \tag{51}$$

where $\mathbf{C}$ and $\mathbf{S}$ are discretized versions of the curl and the divergence operator, respectively, with $\tilde{\mathbf{C}}$ and $\tilde{\mathbf{S}}$ representing the corresponding operators on the dual grid. The equations can now be connected via the material relations, which can as well be discretized:

$$\mathbf{d} = \mathbf{M}_\varepsilon \mathbf{e}, \tag{52}$$

$$\mathbf{b} = \mathbf{M}_\mu \mathbf{h}, \tag{53}$$

$$\mathbf{j} = \mathbf{M}_\sigma \mathbf{e} + \mathbf{j}_s. \tag{54}$$

We assume from now on that the conductivities of all materials used in the grid are negligible so that $\mathbf{M}_\sigma \approx 0$. The time derivatives in Eq. (48) and Eq. (49) can be rewritten using their central difference approximations and then all equations can be combined to yield the update equations for the E- and B-field:

$$\mathbf{e}^{n+1/2} = \mathbf{e}^{n-1/2} + \Delta t \mathbf{M}_\varepsilon^{-1}\left(\tilde{\mathbf{C}}\mathbf{M}_\mu^{-1}\mathbf{b}^n - \mathbf{j}_s^n\right), \tag{55}$$

$$\mathbf{b}^{n+1} = \mathbf{b}^n - \Delta t \mathbf{C}\mathbf{e}^{n+1/2}. \tag{56}$$

Starting from some initial condition (e.g., fields equal to zero everywhere) and using some kind of excitation source in a specified region of the mesh, the fields for each step can be calculated based on the fields from the previous steps, e.g., the E-field at time $n + 1/2$ depends on the E-field from the previous step $n - 1/2$ and the B-field at time n. As the E- and B-fields have to be calculated consecutively for each step this is called a leapfrog scheme. With each time step the fields propagate a distance of one mesh cell. The time step must therefore be chosen such that the fields do not propagate faster than physically possible, i.e., not faster than the speed of light in the material found inside the mesh cell:

$$\Delta t \leq \frac{\sqrt{\varepsilon\mu}}{\sqrt{\left(\frac{1}{\Delta x}\right)^2 + \left(\frac{1}{\Delta y}\right)^2 + \left(\frac{1}{\Delta z}\right)^2}}, \tag{57}$$

where $\Delta x, \Delta y, \Delta z$ are the respective mesh cell sizes. Since the material discretization is the main source of error in this procedure, this equation summarizes the main trade-off when facing FIT simulations: The physical problem can be approximated increasingly well the finer the mesh is, but on the other hand the simulations also need increasingly small time steps, and therefore take longer until a defined final state is reached. The final state in CST is typically signified by the total energy inside the simulation domain. This energy falling under -40 dB with respect to the total energy inserted during the excitation marks the typical steady-state criterion used in this thesis.

3 Ewald sphere for structural colors

This chapter covers the first of the two major blocks of original work presented in this thesis. The main results of this work were published in reference [44]. The results and figures presented here are partly taken from the publication.

The derivation presented in chapter 3.2.1 was in its original form done by Slawa Lang and is available in reference [50].

3.1 Introduction to structural colors

The term structural color refers to colors which are not a result of selective absorption but of constructive and destructive interference generated by structural features. Structural coloration is found widely in nature [51–54], especially in insects [55–62] and bird feathers [63–74], but also in animal skin [75–77] and plants [78]. Many examples from nature are based on ordered nanostructures and therefore show strong iridescence, i.e., their perceived color strongly depends on the observation angle (e.g., [55, 62]). There are, however, also examples for structural colors which show only very weak or no iridescence under daylight illumination. It has been shown that the structures responsible for this effect often exhibit an isotropic shape of their Fourier transform. These isotropic Fourier transforms can, e.g., be broadband, corresponding to white structural color [57], or they can be spherically shell shaped, which leads to wavelength selectivity in the reflectivity spectrum. This shell shape indicates that there is a characteristic length in such structures. As introduced before, this may be caused by disordered structures with short-range order [63–70, 74, 75] or by random arrangements of small ordered substructures, i.e., polycrystals [56, 58, 61]. Non-iridescent colors produced by such structural features are mostly short- and intermediate-wavelength colors like violet, blue and green. Examples for longer wavelength colors solely produced by structure are very rare [75, 79]. While such colors may comprise influences from structural features, they also usually contain selective absorbers influencing their color appearance [54, 63–65, 73–75].

Non-iridescent structural colors are highly interesting for decoration purposes since they allow for producing diverse colors with one single material system by simple scaling of the structure geometry. Since, in contrast to regular pigments, the required features of

such a material system comprise no complex absorption properties, simple and environmentally friendly material systems could be envisaged. As structural colors can be realized from almost non-absorbing dielectric materials, photo-bleaching can easily be avoided, making them very long-lived in comparison to conventional organic pigments. The choice regarding the material entails the option of highly temperature-stable materials like ceramics. By this, structural colors can help to avoid toxic pigments used for the coloration of materials processed under high temperatures, where organic alternatives degrade. E.g., the pigment cadmium red is now banned in the EU for most applications due to environmental and health risks. However, since there is no suitable replacement for high-temperature-processed materials, the use of cadmium pigments in several polymers (e.g., Nylon), ceramics, glasses, and enamels is currently not restricted [80–82].

Current research on structural colors focuses mainly on photonic glasses (see chapter 2.3.3), which are disordered assemblies of monodisperse spherical particles [22, 83, 84]. The monodispersity of the touching particles leads to short-range order. To increase the color saturation of photonic-glass films, the introduction of broadband absorbers [85–91], optimization of film thickness and background [92, 93] and the usage of more complex particles, e.g., core-shell particles [35, 89, 94, 95] have been discussed. However, the gamut of structural coloration is still limited. Just like in nature, so far there is no procedure known to produce highly saturated long-wavelength colors like red or yellow [79].

To describe the light scattering of structural colors, different approaches have been discussed [66, 79, 96]. However, the first-order Born approximation [15] has not been used to its full potential. It is the basis for the Ewald sphere construction which is well known in X-ray scattering [97, 98] and has also found uses in optics, e.g., in holography [99, 100], photonic quasicrystals [101], light extraction from LEDs [102], and nonlinear optics [103]. Yet, its implications on structural colors have not been studied in detail. We published our work on this topic in order to fill out this gap [44]. The main results of our work are presented and discussed in this chapter.

3.2 Ewald sphere construction

The Ewald sphere construction is a well-known and commonly used tool in X-ray diffraction and crystallography. While its application to structural colors was mentioned before [96] and similar approaches based on the spatial Fourier transform of the structure have been used (e.g., [56, 104]) there has not been a detailed analysis of its implications for structural coloration so far. Also, especially when talking about flat, colored films,

Fresnel reflection at the film surface may influence the color impression significantly. With the usual presentation of the first-order approximation [15] it is impossible to take this into consideration as the Fresnel reflection is a strong effect. For these reasons we use a quantitative approach that shall be outlined here. The full derivation is also shown in reference [50], an alternative derivation is presented in the supplementary materials of [35].

3.2.1 Derivation

Let us start the discussion by recalling Maxwell's curl equation governing the electric field, $\boldsymbol{\nabla} \times \boldsymbol{\nabla} \times \mathbf{E}(\mathbf{r}) = (\omega/c)^2 \varepsilon_r(\mathbf{r})\mathbf{E}(\mathbf{r})$ (Eq. (15)). We want to expand the electric fields into a series approximation in order to separate the different scattering orders and then solve for the first-order scattered field using a Green's function method. While this can be done right from this point, and is done like this in reference [50], it leads to a mathematically very complex expression for the Green's function. We will here instead present a simplified version of the derivation which is mathematically much more concise but still conveys the main thoughts going into the derivation. The only thing that we are missing out on by this simplification are polarization effects. We will add them in the end by a more intuitive argument.

As a first step, we rewrite the above-mentioned curl equation in a slightly different way using the vector calculus identity $\boldsymbol{\nabla} \times \boldsymbol{\nabla} \times \mathbf{A} = \boldsymbol{\nabla}(\boldsymbol{\nabla} \cdot \mathbf{A}) - \boldsymbol{\nabla}^2\mathbf{A}$:

$$\boldsymbol{\nabla}^2\mathbf{E}(\mathbf{r}) + \left(\frac{\omega}{c}\right)^2 \varepsilon(\mathbf{r})\mathbf{E}(\mathbf{r}) - \boldsymbol{\nabla}\big(\boldsymbol{\nabla} \cdot \mathbf{E}(\mathbf{r})\big) = 0. \tag{58}$$

We then use Eq. (9) and the vector calculus identity $\boldsymbol{\nabla} \cdot \psi\mathbf{A} = \psi\boldsymbol{\nabla} \cdot \mathbf{A} + \mathbf{A} \cdot (\boldsymbol{\nabla}\psi)$ as well as the fact that $\boldsymbol{\nabla}\psi/\psi = \boldsymbol{\nabla} \ln \psi$ to obtain

$$\boldsymbol{\nabla} \cdot \mathbf{E}(\mathbf{r}) = -\mathbf{E}(\mathbf{r}) \cdot (\boldsymbol{\nabla} \ln \varepsilon(\mathbf{r})), \tag{59}$$

which can be plugged into Eq. (58) to get

$$\boldsymbol{\nabla}^2\mathbf{E}(\mathbf{r}) + \left(\frac{\omega}{c}\right)^2 \varepsilon(\mathbf{r})\mathbf{E}(\mathbf{r}) + \boldsymbol{\nabla}\big(\mathbf{E}(\mathbf{r}) \cdot (\boldsymbol{\nabla} \ln \varepsilon(\mathbf{r}))\big) = 0. \tag{60}$$

The last term in this expression can be neglected, assuming that the permittivity in the scatterer is slowly changing with position [15]. For our application, this assumption is somewhat unjustified, bearing in mind that in structural colors it is not unusual to have the full dynamic range of the refractive index variation inside the length scale of a single wavelength. It can be shown, however, that for the first-order scattering the only parts of

the solution affected by this omission are again the polarization effects. The remaining terms yield what is commonly known as the Helmholtz equation.

The cartesian field components in Eq. (60) are no more coupled after omitting the last term. Therefore, they can be treated as individual scalar fields. The scalar Helmholtz equation can simply be written as

$$\boldsymbol{\nabla}^2 E(\mathbf{r}) + \left(\frac{\omega}{c}\right)^2 \varepsilon(\mathbf{r}) E(\mathbf{r}) = 0. \tag{61}$$

As in previous chapters (esp. chapter 2.1.2) we will write the spatial dependence of the dielectric permittivity $\varepsilon(\mathbf{r})$ as a superposition of a constant part $\bar{\varepsilon}$ with the spatially varying part $\Delta\varepsilon(\mathbf{r})$. The electric field (component) in the Helmholtz equation can then be expanded in a Taylor series with respect to the amplitude of $\Delta\varepsilon$:

$$E = E_0 + \widehat{\Delta\varepsilon}\tilde{E}_1 + \widehat{\Delta\varepsilon}^2\tilde{E}_2 + \cdots = E_0 + E_1 + E_2 + \cdots. \tag{62}$$

The spatial dependencies of $\Delta\varepsilon$ and E are not written explicitly. Eq. (61) can then be split up by the orders of $\widehat{\Delta\varepsilon}$:

$$\boldsymbol{\nabla}^2 E_0 + k^2 E_0 = 0, \tag{63}$$

$$\boldsymbol{\nabla}^2 E_1 + k^2 E_1 = -\left(\frac{\omega}{c}\right)^2 \Delta\varepsilon E_0, \tag{64}$$

$$\boldsymbol{\nabla}^2 E_2 + k^2 E_2 = -\left(\frac{\omega}{c}\right)^2 \Delta\varepsilon E_1, \tag{65}$$

and so on. Here, $k = \sqrt{\bar{\varepsilon}}(\omega/c)$ is the material wave number. The physical significance of these expressions can be interpreted as follows: The first, zeroth order equation describes the incident field which is considered as unperturbed. The second (third, …) equation describes the first-order (second-order, …) scattered field, that results from the scattering of the zeroth-order (first-order, …) field at the permittivity perturbation. If scattering is weak, the first-order expression can be used as an estimation of the total scattered field, so from now on we will neglect all higher-order terms.

We will moreover assume that the excitation is a simple plane wave, $E_0 = \hat{E}_0 \exp(i\mathbf{k}_0\mathbf{r})$, where a harmonic time dependence with angular frequency ω is again implicitly assumed. More complex excitations can be treated as a superposition of several plane waves. To solve Eq. (64) we use the Green's function formalism, according to which E_1 is found by convolving the source term on the right side with the appropriate Green's function:

$$E_1(\mathbf{r}) = \left(\frac{\omega}{c}\right)^2 \hat{E}_0 G(\mathbf{r}) * \Delta\varepsilon(\mathbf{r}) \exp(i\mathbf{k}_0\mathbf{r}). \tag{66}$$

The convolution is turned into a multiplication by Fourier transforming the whole problem:

$$E_1(\mathbf{k}) = \left(\frac{\omega}{c}\right)^2 \hat{E}_0 G(\mathbf{k})\Delta\mathcal{E}(\mathbf{k}) * \delta(\mathbf{k}-\mathbf{k}_0) = \left(\frac{\omega}{c}\right)^2 \hat{E}_0 G(\mathbf{k})\Delta\mathcal{E}(\mathbf{k}-\mathbf{k}_0), \tag{67}$$

where δ denotes the Dirac delta function and $\Delta\mathcal{E}(\mathbf{k})$ is the Fourier transform of $\Delta\varepsilon(\mathbf{r})$.

The Green's function for the Helmholtz operator is typically written as [105]

$$G(\mathbf{r}) = \frac{\exp(ik|\mathbf{r}|)}{4\pi|\mathbf{r}|} \multimap\bullet\ G(\mathbf{k}) = \frac{1}{|\mathbf{k}|^2 - k^2}. \tag{68}$$

It should be mentioned, though, that the reciprocal space expression is incomplete [105]. In its above written form, it allows outgoing waves as well as incoming waves, acting simultaneously as a source and a sink – the latter being unphysical for the description of scattering. There are two ways to remedy this situation: The first and obvious one would be to complement the reciprocal Green's function with an added part that restores physicality. This is the path chosen in reference [105]. The added part is a shifted Dirac pulse, corresponding to a negative incoming wave that compensates for the existing incoming wave part. The second option that is chosen by most authors, and that we are going to choose as well, is to allow the incoming waves for now, and then eliminate them by correctly choosing the integration contour later. With this, the Green's function can be plugged into Eq. (67) and the full expression can be inversely Fourier transformed to gain back the real space expression:

$$E_1(\mathbf{r}) = \frac{\hat{E}_0\omega^2}{(2\pi)^3 c^2} \iiint \frac{\Delta\mathcal{E}\left(\tilde{\mathbf{k}}-\mathbf{k}_0\right)\exp\left(i\tilde{k}_z z\right)}{\left|\tilde{\mathbf{k}}\right|^2 - k^2} \exp\left(i\tilde{\mathbf{k}}_\rho\boldsymbol{\rho}\right) d\tilde{k}_z d^2\tilde{k}_\rho. \tag{69}$$

We will now assume that the permittivity perturbation is an infinitely extended film with a certain thickness. Here, $\boldsymbol{\rho}$ denotes the directions along the film (x and y) and z is the coordinate orthogonal to the film surface such that $\mathbf{r} = [\boldsymbol{\rho}, z]^T$. Accordingly, $\tilde{\mathbf{k}} = \left[\tilde{\mathbf{k}}_\rho, \tilde{k}_z\right]^T$ are the corresponding directions in k-space. The integration over $\tilde{k}_z$ includes two singularities at $\pm k_z$ but can be carried out using the residue theorem. The contour over which the integration is performed is chosen such that it only contains the pole at positive k_z. This corresponds to the limitation to outgoing waves mentioned above. The integration then becomes

$$\begin{aligned} E_1(\mathbf{r}) &= \frac{\hat{E}_0\omega^2}{(2\pi)^3c^2}\iint 2\pi i \operatorname*{Res}_{\tilde{k}_z\to k_{1,z}}\left\{\frac{\Delta\mathcal{E}(\tilde{\mathbf{k}}-\mathbf{k}_0)\exp(i\tilde{k}_z z)}{(\tilde{k}_z-k_{1,z})(\tilde{k}_z+k_{1,z})}\right\}\exp(i\mathbf{k}_{1,\rho}\boldsymbol{\rho})\,d^2k_{1,\rho} \\ &= \frac{i\hat{E}_0\omega^2}{2^3\pi^2c^2}\iint \frac{\Delta\mathcal{E}(\mathbf{k}_1-\mathbf{k}_0)}{k_{1,z}}\exp(i\mathbf{k}_1\mathbf{r})\,d^2k_{1,\rho}, \end{aligned} \tag{70}$$

where $\mathbf{k}_1 = \left[\mathbf{k}_{1,\rho}, k_{1,z}\right]^T$ is the wave vector of the scattered wave, with its z-component $k_{1,z} = \sqrt{k^2 - k_{1,\rho}^2}$ and $k_{1,\rho} = \left|\mathbf{k}_{1,\rho}\right|$. We also made the substitution $\tilde{\mathbf{k}}_\rho = \mathbf{k}_{1,\rho}$ to show that it changed its meaning from a purely abstract integration variable to a component of an actual, physical wave vector.

We can now see that the E-field is a superposition of plane waves which are weighted by the shifted Fourier transform of the scatterer. We will only allow k_z to be real, i.e., we will ignore evanescent waves which do not carry power away from the scatterer. By this, we limit the integration domain to a disk of radius k_ρ. The integral can be performed over the spherical shell spanned by $|\mathbf{k}_1|$ by changing the integration variable to $d^2k_1 = (k_z/k)d^2k_\rho$. Since we limited our scope to outgoing "plane waves", only half of the scattering directions can actually affect the field in point $\mathbf{r}$, so we can limit the integration domain to that hemisphere:

$$E_1(\mathbf{r}) = \frac{i\hat{E}_0\omega}{2^3\pi^2c\sqrt{\bar{\varepsilon}}}\iint_{\text{half of sphere } |\mathbf{k}_1|=k} \Delta\mathcal{E}(\mathbf{k}_1-\mathbf{k}_0)\exp(i\mathbf{k}_1\mathbf{r})\,d^2k_1. \tag{71}$$

In this expression, the half sphere over which we are integrating corresponds to half of the Ewald sphere which is going to be discussed in detail soon. However, when looking at color films we are usually not interested in the scattered electric field, but in the scattered power. To get there, we need the magnetic field, which can be found using Eq. (13), $\boldsymbol{\nabla}\times\mathbf{E}(\mathbf{r}) = i\omega\mu_0\mathbf{H}(\mathbf{r})$. We now run into problems as the cross product is not defined for scalar fields, so at this point we will have to make the transition back to a vector field and finally add in the polarization terms that we missed out on due to our initial simplifications.

The $\mathbf{k}_1$-vectors describe the scattering wave vectors. As discussed in chapter 2.2, the incident field can be thought of as exciting dipolar oscillations in each point of the scatterer, which then emit light with a Hertzian dipole characteristic. We can characterize the polarization of the emission from these dipoles by means of the plane spanned by $\mathbf{k}_1$ and the film normal $\mathbf{e}_z$. The direction orthogonal to this plane will be denoted as $\mathbf{e}_1^s = \mathbf{k}_1\times\mathbf{e}_z/|\mathbf{k}_1\times\mathbf{e}_z|$ and the one parallel to it $\mathbf{e}_1^p = \mathbf{k}_1\times\mathbf{e}_1^s/|\mathbf{k}_1\times\mathbf{e}_1^s|$. Then the $\mathbf{e}_1^s$-component of the scattered field depends on the projection of the polarization vector

of the incident field onto $\mathbf{e}_1^s$ itself, $\mathbf{e}_0 \cdot \mathbf{e}_1^s$, just like in a Hertzian dipole. The same holds true for the p-polarization. The terms then just need to be multiplied to the corresponding scattered plane waves to restore the full vectorial field:

$$\begin{aligned}\mathbf{E}_1(\mathbf{r}) = \frac{i\hat{E}_0\omega}{2^3\pi^2 c\sqrt{\bar{\varepsilon}}} \iint\limits_{\text{half of sphere } |\mathbf{k}_1|=k} \Delta\mathcal{E}(\mathbf{k}_1 - \mathbf{k}_0)\Big((\mathbf{e}_0 \cdot \mathbf{e}_1^s)\mathbf{e}_1^s \\ + \left(\mathbf{e}_0 \cdot \mathbf{e}_1^p\right)\mathbf{e}_1^p\Big) \exp(i\mathbf{k}_1\mathbf{r})\, d^2k_1.\end{aligned} \tag{72}$$

As noted before, the rigorous derivation of this expression can be found in reference [50].

From the knowledge of the electric field, the magnetic field can then be found using Eq. (13):

$$\begin{aligned}\mathbf{H}_1(\mathbf{r}) &= \frac{1}{i\mu_0\omega}\boldsymbol{\nabla} \times \mathbf{E}_1(\mathbf{r}) \\ &= \frac{i\hat{E}_0\omega}{2^3\pi^2 Z_0 c} \iint\limits_{\text{half of sphere } |\mathbf{k}_1|=k} \Delta\mathcal{E}(\mathbf{k}_1 - \mathbf{k}_0)\Big((\mathbf{e}_0 \cdot \mathbf{e}_1^s)\mathbf{e}_1^p \\ &\quad - \left(\mathbf{e}_0 \cdot \mathbf{e}_1^p\right)\mathbf{e}_1^s\Big) \exp(i\mathbf{k}_1\mathbf{r})\, d^2k_1,\end{aligned} \tag{73}$$

where $Z_0 = \sqrt{\mu_0/\varepsilon_0}$ is the free space wave impedance and $c = 1/\sqrt{\mu_0\varepsilon_0}$ was used. The power scattered into the upper half space is then

$$\begin{aligned}P_{1,z} &= \iint \frac{1}{2}(\mathbf{E} \times \mathbf{H}^*) \cdot \mathbf{e}_z dxdy \\ &= \frac{I_0\omega^2}{2^4\pi^2 c^2\bar{\varepsilon}} \iint\limits_{\text{half of sphere } |\mathbf{k}_1|=k} |\Delta\mathcal{E}(\mathbf{k}_1 - \mathbf{k}_0)|^2 \Big((\mathbf{e}_0 \cdot \mathbf{e}_1^s)^2 \\ &\quad + \left(\mathbf{e}_0 \cdot \mathbf{e}_1^p\right)^2\Big)\, d^2k_1,\end{aligned} \tag{74}$$

where $I_0 = \sqrt{\bar{\varepsilon}}\left|\hat{E}_0\right|^2/(2Z_0)$ is the intensity of the incident wave. The integration over x and y here only affects the phases of the plane waves, but as we integrate over the whole x-y-plane all interferences vanish.

3.2.2 Geometrical interpretation

The scattered power can be seen to mainly depend on the Fourier transform of the perturbation forming the scatterer. The Fourier transform is shifted by $\mathbf{k}_0$ and then evaluated on the sphere formed by $|\mathbf{k}_1| = k$. Directions where the shifted Fourier transform has large values correspond to directions of strong scattering. This

interpretation is in line with the standard representation of the Ewald sphere as it is known in X-ray scattering of atomic crystals [97], with the only difference being the shift of the coordinate system by $\mathbf{k}_0$. However, since the two are equivalent, and the standard representation makes it easier to show the scattering of different wavelengths and incidence directions of the incoming wave, we will adopt the standard representation for most of the following discussion.

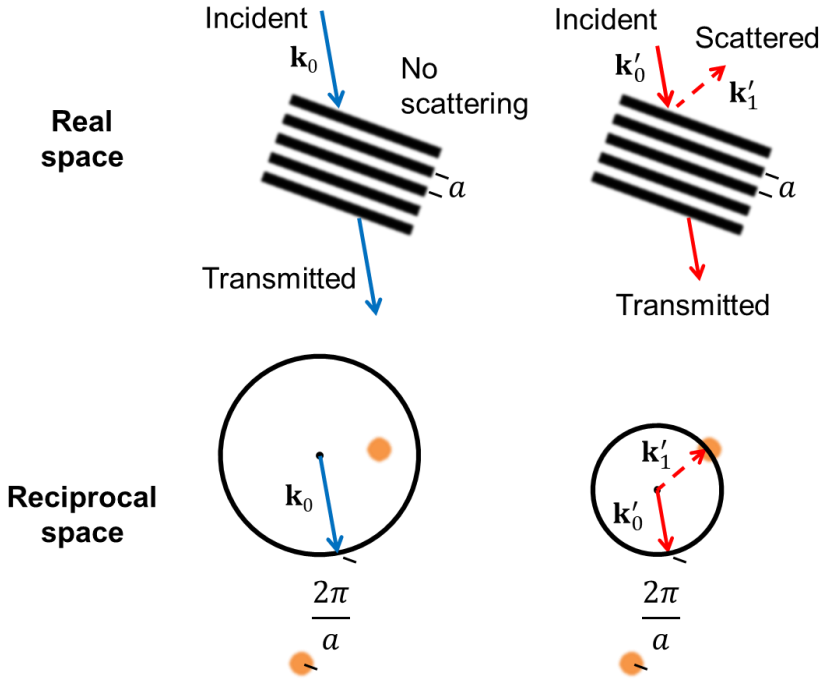


Fig. 6. Ewald sphere construction for the example of a Bragg mirror with a low refractive-index contrast. The Bragg mirror with period a in real space corresponds to two mirror-symmetric spots at $\pm 2\pi/a$ along the Bragg mirror's normal in reciprocal space. Incident waves with wave vectors $\mathbf{k}_0$ and $\mathbf{k}_0'$ (solid arrows) with equal directions but different wavelengths are incident on the Bragg mirror. The left, short-wavelength case is off Bragg resonance while the right, long-wavelength case shows a k-vector for which Bragg reflection and thus a scattered wave vector $\mathbf{k}_1'$ (dashed arrows) occurs. In reciprocal space, the Ewald sphere overlaps with the non-zero Fourier-transform spots in which case light is scattered back in the corresponding direction (right), or it does not overlap with the spots in which case no scattering is observed and all light is transmitted (left).

The Ewald sphere construction can be exemplified schematically with a Bragg mirror with a weak refractive-index contrast, as illustrated in Fig. 6. A simple Bragg mirror is comprised of a sinusoidal variation of the refractive index. The Fourier transform of the sinusoidal refractive-index distribution in real space (top panel) produces two symmetric spots in k-space (bottom panel) at $\pm 2\pi/a$ on the axis defined by the direction of the refractive-index modulation, where a is the lattice constant. The figure also shows the

k-vectors of two waves with different wavelengths impinging on the Bragg mirror under the same angle. In order to draw the Ewald sphere, the k-vector of an incident wave is drawn in reciprocal space such that it points at the origin of reciprocal space. The Ewald sphere is then the sphere around the starting point of the k-vector with its radius corresponding to the length of the k-vector. It thereby represents all potential directions of elastic scattering. Then the directions from the center of the Ewald sphere to where it intersects the Fourier transform represent the actual directions of scattering. The value of the Fourier transform in the intersection point defines the scattering strength. For the scattered power, according to Eq. (74) the absolute square value of the Fourier transform needs to be used.

In the right case of Fig. 6 the Ewald sphere intersects with the Fourier transform of the mirror, which leads to scattering. The direction of scattering is defined by the connection of the Ewald sphere's center to the intersection region which results in the only[8] existing scattered wave vector $\mathbf{k}_1$. In the left case no light is scattered since the Ewald sphere only occupies regions in reciprocal space where the Fourier transform is practically zero. The findings are consistent with Bragg's law.

3.2.3 Application to k-shell structures

In the following we will focus on structures for which the reciprocal space representation takes the form of a spherical shell (k-shell). Examples for this include photonic glasses or the structures found in natural structural colors. As mentioned before, this shape indicates that there is a characteristic length a in the structure which is found along all directions, and which is connected to the radius K of the k-shell by $K = 2\pi/a$. The Ewald sphere construction can be used to predict the wavelength- and angle-dependent scattering of such a structure under plane-wave illumination.

A schematic depiction of this is shown in Fig. 7. For short wavelengths, light is scattered forward (i.e., into the lower half space) such that the wave vectors of scattered light lie on the surface of a cone (Fig. 7A). The opening angle of this cone increases when longer wavelengths, thus shorter wave vectors, are considered, until the situation in Fig. 7B is reached, where light is perpendicularly scattered. For even longer wavelengths the Ewald sphere shrinks further, leading to scattered wave vectors lying on the surface of a cone that is now directed upwards (i.e., backscattering). At the point where the length of the incident wave vector, and therefore the radius of the Ewald sphere, equals half the radius

[8] Due to the finite size of the Bragg mirror the spots in reciprocal space are of finite size as well, so in principle there is a distribution of scattering k-vectors in a narrow angle interval. Summarizing them into one does make sense with respect to the visualization, though.

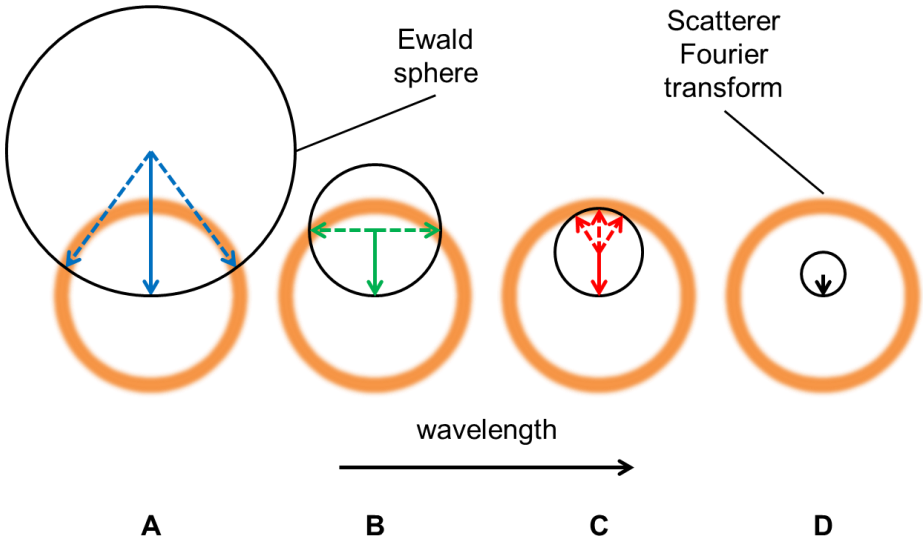


Fig. 7. 2D cut through the Ewald sphere construction for the scattering from a structure with a spherical-shell shaped Fourier transform. A: Short wavelength, leading to forward scattering; B: intermediate wavelength, leading to perpendicular scattering; C: long wavelength, leading to backscattering; and D: very long wavelength, leading to no scattering. Solid arrows indicate the wave vectors of the incident waves, dashed arrows indicate wave vectors of scattered waves.

of the k-shell, backscattering into a small solid angle should be observed. The scattering for this situation is shown in Fig. 7C; the scattering cone is filled with wave vectors due to the finite thickness of the k-shell. For even longer wavelengths the Ewald sphere eventually does not intersect with the Fourier transform anymore and all incident light is transmitted. It should be noted that even structural colors that are found to be non-iridescent under diffuse illumination show some iridescence under directional illumination [66]. Hence it is not surprising that with the Ewald sphere construction a change in scattering directions depending on the wavelength is predicted.

From this it is already possible to draw conclusions on the reflectivity spectrum of the scattering structure. There must be a reflectivity cutoff towards long wavelengths at the point where the Ewald sphere stops intersecting with the k-shell. Such a cutoff towards longer wavelengths is especially desirable for short-wavelength colors like blue or green. In fact, we showed in reference [35] that the optimization of this cutoff can lead to a significantly enhanced color saturation of a blue structural color. This is also in line with the observation that natural structures having a shell-shaped Fourier transform often exhibit pure blue colors [63].

In the other direction, i.e., towards shorter wavelengths, the situation is more complex. Different wavelengths are scattered into different angles, but down to the perpendicular scattering case (Fig. 7B) they all seem to contribute to the reflectivity. Moreover, even

wavelengths shorter than that are still significantly scattered; and while they initially travel into a forward direction (with respect to the incident wave's direction), they may be subject to multiple scattering or diffusion if the refractive-index perturbation is strong enough. This would again open paths for backscattering, allowing these wavelengths to influence the reflectivity. This complexity already hints at the problems encountered when dealing with longer-wavelength structural colors. We will discuss this topic further in chapter 3.5 in the light of the presented simulation results.

The Ewald sphere construction can be used to make simple geometrical calculations of the scattering angles at certain wavelengths. E.g., the long-wavelength edge of the direct backscattering peak corresponds to the wavelength where the length k of the k-vector equals half the radius K of the k-shell, $k = K/2$. The radii of the Ewald sphere and the k-shell are $k = 2\pi\bar{n}/\lambda_0$ and $K = 2\pi/a$, respectively, with $\lambda_0 = 2\pi c_0/\omega$ being the free space wavelength. It follows that the back reflection sets in at $\lambda_0 = 2a\bar{n}$. Another simple example is the scattering at 90°. This corresponds to the case where the length of the incident wave's k-vector is by a factor $\sqrt{2}$ smaller than the radius of the k-shell, and therefore to a vacuum wavelength of $\lambda_0 = \sqrt{2}a\bar{n}$.

Another slightly more involved but still purely geometrical approximation can be made regarding the scattering strength in the backscattering regime, i.e., between the long-

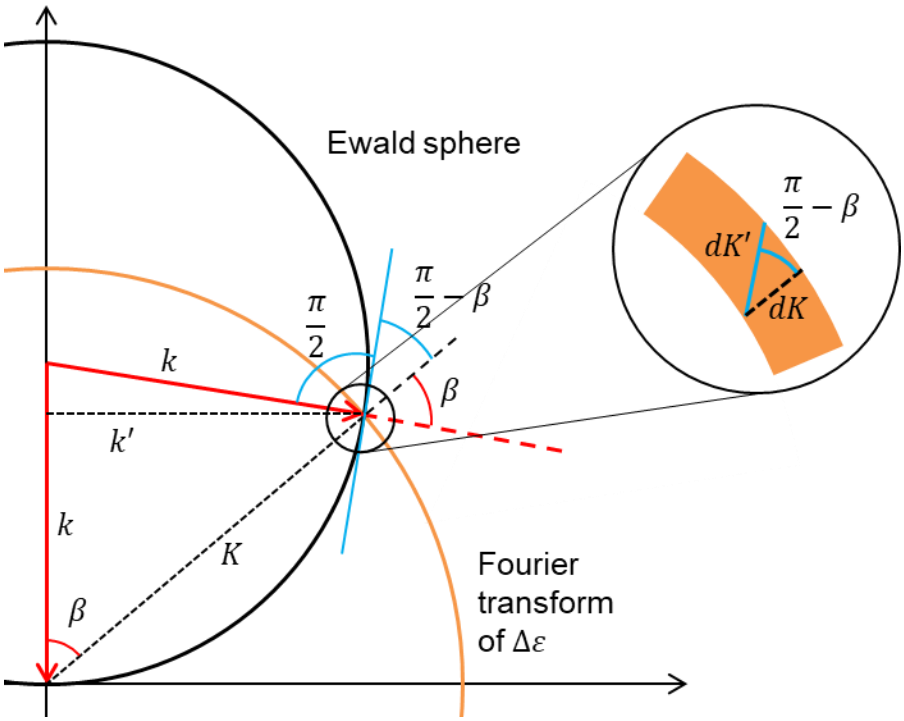


Fig. 8. Schematic visualization of the intersection between the Ewald sphere and an infinitesimally thin k-shell. From the geometry it can be shown that the overlap area does not depend on the wavelength.

wavelength cutoff and the perpendicular scattering case for which we just found the corresponding wavelengths. For this part of the spectrum, it can be shown that the overlap area of the Ewald sphere and the k-shell is independent of the Ewald sphere's radius, and therefore of the light wavelength.

The radially symmetric Fourier transform of the scatterer can generally be described by a superposition of infinitesimally thin spherical shells with different weightings. For one of such rings the Ewald sphere construction is shown in Fig. 8. The absolute value of the incident and scattered wave vector is k, the radius of the spherical Fourier transform is K and its width is dK.

From the sketch in Fig. 8 it can be seen that the overlap area has the form of a ring with radius k' and width dK'. Thus, the overlap area is $dA = 2\pi k' dK'$. It is then found that $dK' = dK/\cos(\pi/2 - \beta) = dK/\sin(\beta)$ and $k' = K\sin(\beta)$. Therefore, the overlap area is $dA = 2\pi K dK$, which is independent of k. In consequence, the integral in Eq. (74) does not depend on k. Thus, the scattered power in the backscattering regime scales only with the ω^2 in front of the integral.

3.2.4 Scattering from a film

When discussing color, a typical geometry to be considered is an infinitely extended film. However, for an infinite film the incident power, and by consequence the scattered power, is infinite. Therefore, we will have to normalize the scattered power to a certain (finite) incident power falling onto a finite excerpt of the film. If a representative excerpt of the film is considered, i.e., if the excerpt is chosen so large that for an even larger excerpt the statistical properties of the excerpt are largely the same, few adjustments to the previous equation are necessary: The scatterer Fourier transform is now only calculated for the scattering volume, and the power is normalized by the area of the excerpt. Naming the edge length of the excerpt l, we can write the average power density of the scattered light as

$$\bar{S}_{1,z} = \frac{I_0 \omega^2}{2^4 \pi^2 c^2 l^2 \bar{\varepsilon}} \iint_{\text{half of sphere } |\mathbf{k}_1|=k} |\Delta\mathcal{E}_l(\mathbf{k}_1 - \mathbf{k}_0)|^2 \left((\mathbf{e}_0 \cdot \mathbf{e}_1^s)^2 + \left(\mathbf{e}_0 \cdot \mathbf{e}_1^p\right)^2 \right) d^2 k_1. \tag{75}$$

In a last step we can then normalize by the incident power and include the Fresnel reflections at the surface of the film to get the aggregated reflection spectrum of a color film:

$$R = R_{\mathrm{af}} + \frac{T_{\mathrm{af}}\omega^2}{2^4\pi^2c^2l^2\bar{\varepsilon}} \iint_{\text{half of sphere } |\mathbf{k}_1|=k} |\Delta\mathcal{E}_l(\mathbf{k}_1 - \mathbf{k}_0)|^2 \left(T_{\mathrm{fa}}^s(\mathbf{e}_0 \cdot \mathbf{e}_1^s)^2 + T_{\mathrm{fa}}^p\left(\mathbf{e}_0 \cdot \mathbf{e}_1^p\right)^2\right) d^2k_1. \tag{76}$$

Here, R and T are the reflectivity and transmissivity of the film surface, respectively. The subscripts "af" and "fa" represent the transition from air into the film and vice-versa. Note that the transmission of the scattered wave into air is polarization-dependent, which is denoted by the superscripts *s* and *p* in the respective transmissivities. The reflectivity at the air-film interface at normal incidence is simply

$$R_{\mathrm{af}} = \left|\frac{(\bar{n}-1)}{(\bar{n}+1)}\right|^2 \tag{77}$$

and $T_{\mathrm{af}} = 1 - R_{\mathrm{af}}$. The coefficients for film-air transmission depend on the scattering angle, so the full Fresnel equations (Eq. (29) and (30)) are needed. In this case, it is convenient to rewrite them using the k-vectors directly,

$$T_{\mathrm{fa}}^s = 1 - \left|\frac{\left(k_{1,z}^{\mathrm{air}} - k_{1,z}\right)}{\left(k_{1,z}^{\mathrm{air}} + k_{1,z}\right)}\right|^2 \tag{78}$$

and

$$T_{\mathrm{fa}}^p = 1 - \left|\frac{\left(\bar{n}^2k_{1,z}^{\mathrm{air}} - k_{1,z}\right)}{\left(\bar{n}^2k_{1,z}^{\mathrm{air}} + k_{1,z}\right)}\right|^2, \tag{79}$$

where $k_{1,z}^{\mathrm{air}} = \sqrt{(\omega/c)^2 - k_{1,\rho}^2}$. The half sphere over which the integral is formed corresponds to the upper half space above the film.

The angle-dependent transmissivity of the film surface, in combination with the wavelength-dependent scattering angles discussed before (see Fig. 9), bears important consequences for the reflection spectrum: With an increasing opening angle of the scattering cone for decreasing wavelengths the backscattered light will be increasingly strongly reflected at the film-air surface, up to the angle of total internal reflection. This brings about a wavelength-selective trapping of light and provides an additional cutoff towards short wavelengths. Such a second cutoff would be required to prevent shorter wavelengths from being reflected and added to the color mix, thus compromising the purity of long-wavelength colors. Additionally, depending on the thickness of the scattering volume as well as on the direction of scattered light, the light path can become

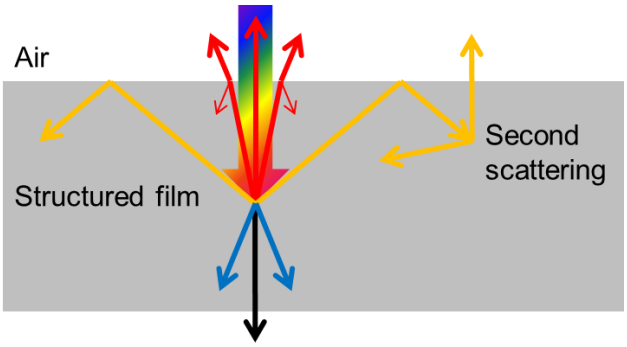


Fig. 9. Schematic 2D representation of the scattering in a film as a function of wavelength. The film is structured in such a way that its Fourier transform is a spherical shell (not shown here, see Fig. 7). Short wavelengths (shown as blue) are scattered in a forward direction. Intermediate wavelengths (orange) are backscattered in a large angle. Due to their scattering angle, they may be reflected at the film surface. Also, their probability for a second scattering event is high due to a long propagation path inside the structure. Long wavelengths (red) are directly scattered back, and very long wavelengths (infrared, shown as black) are not scattered at all and will be transmitted into the downward direction.

long enough to make an additional scattering event highly probable [67]. Such doubly scattered light of shorter wavelengths may then be redirected in such a way that it is not totally internally reflected anymore, thus can be coupled out and will add to the color mix seen by the observer.

Assume, e.g., that for the borderline case in Fig. 7B there is a secondary scattering event. This can be modeled by just another Ewald sphere construction where the incident wave is now the original scattered one travelling parallel to the film surface. This results in the same relative scattering directions, perpendicular to the incidence direction, meaning 50% of the double-scattered light is scattered to the upper half space. This light is again subject to Fresnel reflection and partly to total internal reflection, but a considerable part may now be coupled out. The outcoupled, double-scattered light therefore adds to the reflectivity of the whole structure and thus to the color mix. While the total internal reflection within thin films helps to create a second cutoff at shorter wavelengths, the higher-order scattering makes the generation of long-wavelength, non-iridescent structural colors such as yellow and red much more difficult. This may also indicate why there are hardly any examples of those in nature. The multiple scattering can be suppressed by broadband absorption in the film, as light scattered multiple times accumulates large optical paths. This explains why broadband absorption can help to improve structural color at longer wavelengths [90, 91].

3.3 Model structure

Our model structure is generated by the superposition of several 1D gratings. The structure is mathematically described by a gradual function:

$$n_g(\mathbf{r}) = \bar{n} + \Delta n_g(\mathbf{r}) = \bar{n} + \sum_{i=1}^{N} \Delta n_i \cos(\mathbf{b}_i \cdot \mathbf{r} + \phi_i), \tag{80}$$

where $\bar{n}$ is the mean refractive index and $\Delta n_g(\mathbf{r})$ is the perturbation. N is the total number of gratings, Δn_i is the amplitude of the refractive-index modulation of a single grating, $\mathbf{b}_i$ are the reciprocal lattice vectors defining the grating periods and directions and ϕ_i are the corresponding phases. The same period a, and thus wave vector length $K = |\mathbf{b}_i| = 2\pi/a$, as well as the same amplitude Δn_i is used for each grating. The phases ϕ_i and the grating directions $\mathbf{b}_i/|\mathbf{b}_i|$ are chosen randomly in order to obtain a homogeneous structure. An example structure is shown in Fig. 10. Incidentally, structures generated following this scheme look very similar to the spongy nanostructures that are found in the feather barbs of many bird species and that were found to be responsible for the short-wavelength structural colors in these. However, while the underlying gratings in our model structures give them a long-range correlation, this is not the case in natural structures [63]. For practical applications such structures could be created in a

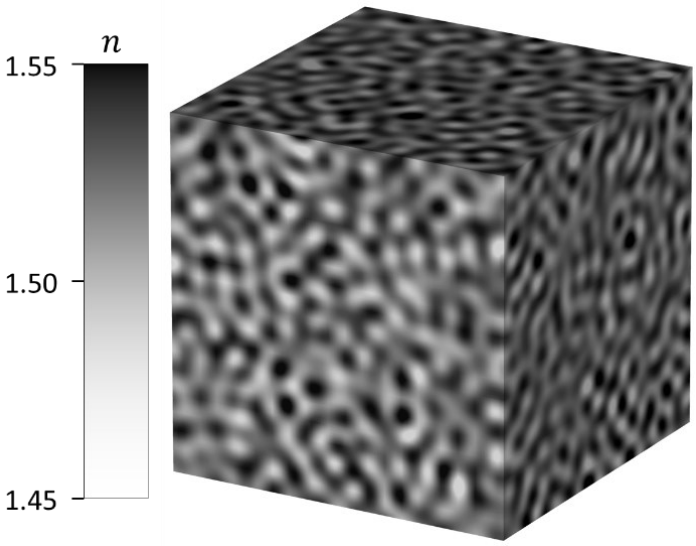


Fig. 10. Real-space representation of the investigated structure. The figure shows a $3 \times 3 \times 3$ µm^3 excerpt from the model structure made by an overlap of 10,000 sinusoidal gratings with 220 nm period. The refractive-index distribution in the structure is scaled such that its standard deviation is $\sigma_g = 0.025$. The shown refractive-index range is limited to 1.45 to 1.55 in order to make the structure more distinguishable, the full refractive-index range considered in the calculations and simulations shown later is from 1.40 to 1.60.

photoreactive material by holographic recording of standing plane waves created by the superposition of two counter-propagating laser beams.

To obtain a suitable model structure for a structural color there are two main objectives: First, the radial thickness of the structure's k-space representation should be as narrow as possible. Judging from the Ewald sphere application discussed so far, this leads to the narrowest reflection peak and therefore to the purest color. Indeed, this conjecture also matches observations in natural structures [63]. Second, the structures should create a non-iridescent color, so they should be directionally isotropic. The optimal structure would therefore have an infinitesimally thin, homogeneously filled spherical shell as its Fourier transform.

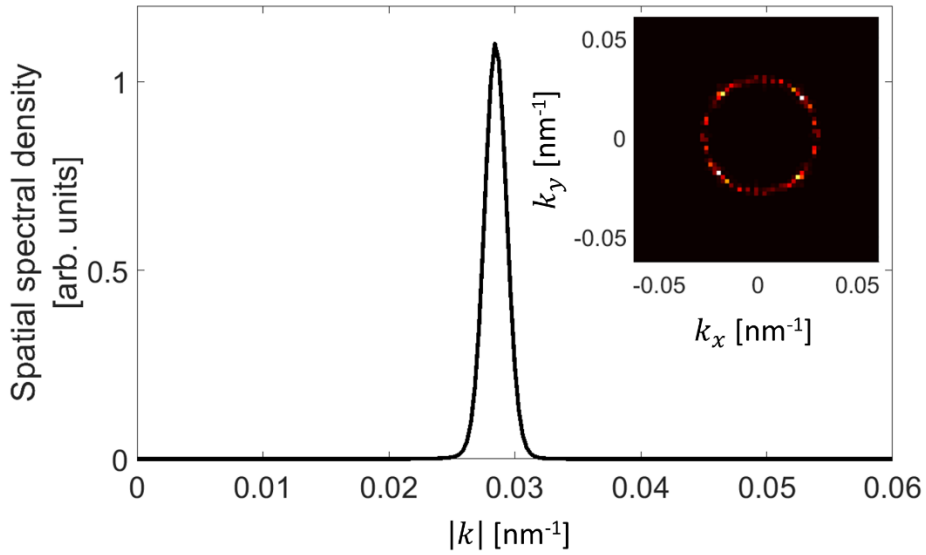


Fig. 11. Fourier-space representation of the investigated structure. Inset: Cut through the spatial spectral density of the Fourier transform of the $3 \times 3 \times 3$ µm^3 refractive-index perturbation shown in Fig. 10. The plane $k_z = 0$ is shown. Main panel: Average of the spatial spectral density as a function of the distance to the origin of reciprocal space.

Since the Fourier transform is a linear operation, the summation of 1D gratings corresponds to a summation of the Fourier transforms of each grating. In this case, the cosine functions making up the individual gratings correspond to two Dirac delta functions, Bragg peaks, at $\pm\mathbf{b}_i$ in reciprocal space. Thus, we generate not a continuous shell in reciprocal space but rather a set of discrete points at equal distance to the origin of k-space. For finite, cuboidal segments of such a structure the Dirac functions are convoluted with sinc-functions in all spatial dimensions, leading to a broadening of the spots. This leads to a dependence of the shell thickness on the structure size, but it also means that with an increasing number of gratings the Fourier transform converges to a

spherical shell. As an example of this, Fig. 11 shows the Fourier transform of the structure shown in Fig. 10. A clear peak with a finite width is seen when averaging over all directions. However, due to the randomness of the phases and directions of the gratings there are some density variations on the spherical shell.

For a large number of gratings, the resulting distribution of refractive-index values turns out to have a Gaussian distribution with mean $\bar{n}$. Thus, we can characterize the structure by the standard deviation σ_g of its refractive-index distribution. The standard deviation can be shown to be proportional to the modulation strength of the individual gratings, Δn_i. To derive the proportionality factor, we first rewrite the total phase as $\theta_i = \mathbf{b}_i \cdot \mathbf{r} + \phi_i$, yielding

$$\Delta n_g = \Delta n_i \sum_{i=1}^{N} \cos(\theta_i). \tag{81}$$

The absolute square of this can be split into self-interacting and co-interacting grating terms:

$$\begin{aligned} \left|\Delta n_g\right|^2 &= \Delta n_i^2 \sum_{j=1}^{N} \cos(\theta_j) \sum_{k=1}^{N} \cos(\theta_k) \\ &= \Delta n_i^2 \left(\sum_{\substack{j,k=1 \\ j=k}}^{N} \cos^2(\theta_j) + \sum_{\substack{j,k=1 \\ j\neq k}}^{N} \cos(\theta_j)\cos(\theta_k) \right). \end{aligned} \tag{82}$$

Averaging over this distribution, the first term has an expectation value of $N/2$ while the second term has an expectation value of zero, resulting in the standard deviation

$$\sigma_g^2 = \langle \left|\Delta n_g\right|^2 \rangle = \Delta n_i^2 \frac{N}{2}. \tag{83}$$

The relation between the individual grating refractive-index amplitude and the standard deviation of the refractive-index perturbation is therefore given by the factor $\sqrt{N/2}$. We confirmed this factor on several structures with different grating numbers and phase realizations.

The model structure we used for simulation was produced as described in Eq. (80) with $N = 10{,}000$ gratings, a period of $a = 220$ nm and an average refractive index of $\bar{n} = 1.5$. The grating refractive index was set to $\Delta n_i \approx 3.53 \cdot 10^{-4}$ to obtain a standard deviation of $\sigma_g = 0.025$. This very low contrast is needed so the first-order Born approximation holds,

as will be shown later. We decided to truncate the refractive-index values at $\bar{n} \pm 4\sigma_g$ in order to exclude on the one hand values that are smaller than one and on the other hand extremely high-refractive-index points that could dominate the overall scattering. With the assumption of a Gaussian distribution this range contains more than 99.99% of all refractive-index values so only very few points are affected by this.

The structure corresponds to a spherical shell in the Fourier spectrum with its maximum at $|k| = |\mathbf{b}_i| = 0.0284\ \mathrm{nm}^{-1} \approx K$ (cf. Fig. 11). We chose these parameters to get a long-wavelength reflectivity edge at a free-space wavelength of $\lambda_0 = 2\bar{n}a = 660$ nm which is in the red wavelength range. By scaling the geometrical parameters of the structure, the whole spectrum could also be shifted to arbitrary other wavelengths. The scaling applies to the whole spectrum, however, so a structure producing, e.g., a pure blue color cannot generally be scaled to produce other pure colors as other reflection peaks may be shifted into or out of the visible wavelength range. We will actually see that this is a very relevant restriction to our structures, which would make a great blue color by shifting unwanted parts of the reflection spectrum into the invisible UV range, but which also struggle to produce a bright red due to those unwanted parts.

3.4 Simulation method

Next, we choose a specific implementation of the presented model structure and calculate its reflectivity spectrum. For this structure we apply both the first-order approximation and numerical simulation using FIT.

A volume of $6 \times 6 \times 40\ \mu\mathrm{m}^3$ was used. The lateral (x- and y-) dimensions (see Fig. 12A) are big enough to be representative of a film-like structure. The rather large thickness of 40 µm along the z-direction was chosen in order to obtain a significant reflectivity while keeping the refractive-index contrast low, which is a prerequisite for the application of the first-order approximation. We assume that there is air above the film and below is a material that does not allow any reflection. The latter can either be an absorber or a lower half space filled with a material matched to the mean refractive index of the scattering structure. We use these asymmetric top and bottom boundary conditions to resemble a structural-color film as a coating on another material with similar refractive index as a typical arrangement for a structural color.

As a reference for the scattering behavior predicted with the first-order approximation we performed FIT simulations of the same system using the time-domain solver of CST Microwave Studio [46]. The structure is excited by a plane wave that is normally incident and polarized in x-direction (coordinates defined as in Fig. 12A). The lateral boundary

conditions are defined as perfect electric and magnetic conductors in a way such that the incident wave is not disturbed. By this, the boundaries act as perfect mirrors and thus again emulate the behavior of an infinitely extending film. We found the error induced by using mirror boundary conditions to be negligible for the simulated width of 6 µm as no major changes in the spectrum occurred after changing the width[9]. Below the structure there is an additional block of material with a refractive index matched to the mean refractive index of the structure to minimize reflection and ensure a controlled transition to the bottom boundary of the simulation volume. For the top and bottom of the simulation volume open boundaries were used which act as reflection-free terminations. The time-resolved reflected and transmitted fields are monitored in plane areas close to the upper and lower boundary of the simulation volume, respectively. The time signals are then converted into the frequency domain using a discrete Fourier transform. From the fields in the frequency domain the powers can be calculated. Finally, by normalization to the intensity of the incident wave and integration over the respective monitor planes the reflectivity and transmissivity are found. Using the spatial Fourier transform of the field distribution in a plane above the simulated structure we can also obtain the 2D distribution of the in-plane components of the scattered k-vectors which directly correspond to the angle distribution of scattered waves for the specified wavelength.

As a final note, we want to emphasize that the reflectivity spectra shown in this work do not exactly represent the color expected from a realistic structural color. We acquired the reflectivity by integrating over the whole upper half space, whereas in realistic scenarios the recipient typically receives light reflected into very small solid angles, only. Furthermore, all simulations were considering normal incidence, while in practical applications colors are often subject to diffuse illumination. So some caution should be exercised when interpreting the results.

3.5 Results and discussion

Fig. 12 compares the reflectivity spectra of the idealized model structure as predicted by FIT and by first-order approximation without and with Fresnel reflection. The FIT simulation is represented by the black curve and shall be discussed first. It shows a relatively strong reflectivity at wavelengths between approximately 620 and 665 nm. The steep edge on the long-wavelength side of this peak fits to the expected cutoff of the overlap between the Ewald sphere and the Fourier transform of the structure, leading to

[9] The fine structure of the noise does change, but the peak levels and positions are the same.

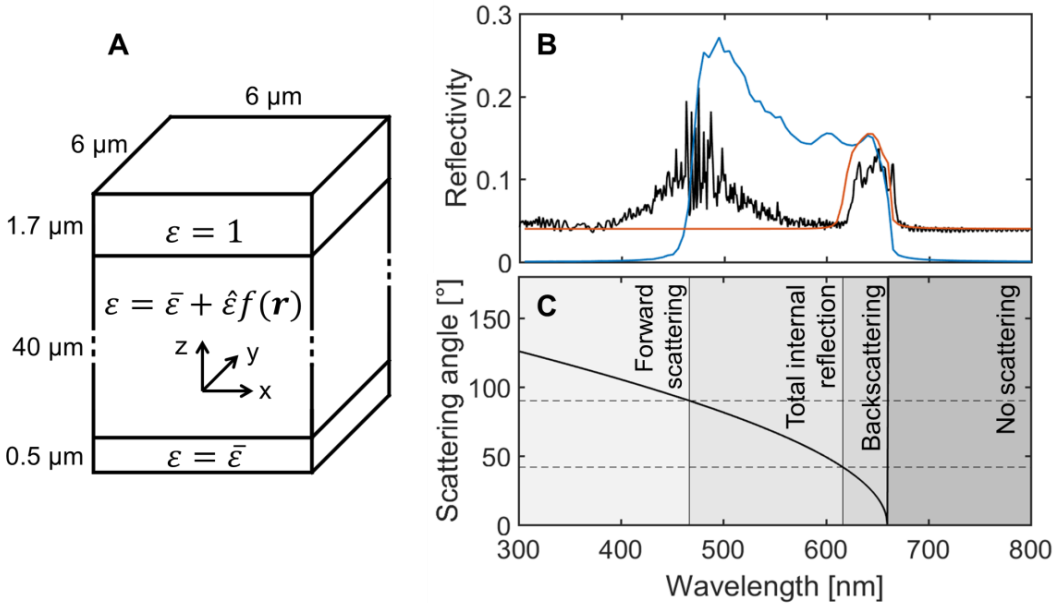


Fig. 12. Simulation results and their connection to the theoretical considerations based on the Ewald sphere. A: Schematic of the simulated volume. B: FIT-simulated reflectivity spectrum of the model structure with 40 µm thickness, a mean refractive index of 1.5 and a refractive-index standard deviation of $\sigma_g = 0.025$ (black curve). In comparison to that, the first-order approximation calculated without (blue curve) and with (red curve) consideration of interface reflections is shown. The incident wave impinges normally onto the film from the top. C: Scattering angle for first-order scattering with respect to the normal for a scattering structure that exhibits a perfect spherical shell in k-space with radius $K = 0.0286\ \mathrm{nm}^{-1}$. The horizontal, dashed lines mark the 90°-angle and the angle of total internal reflection at the film-air interface.

all wavelengths longer than 665 nm being transmitted. The residual reflectivity for these wavelengths is only due to Fresnel reflection at the interface, which for air and the used material with mean refractive index of 1.5 has a value of 0.04. The steep slope at the short-wavelength side of this peak is defined by the angle of total internal reflection. Scattered light of wavelengths shorter than 617 nm is impinging on the film interface from inside the film at angles larger than the critical angle. Thus, it is reflected back into the film via total internal reflection (orange arrows in Fig. 9) and then has a high chance to leave the structure at the bottom boundary.

Using the Ewald sphere construction, the scattering direction for incident light at a free-space wavelength of about 467 nm turns out to be perpendicular to the normal direction of incidence (as in Fig. 7B). As discussed in chapter 3.2.3, this is just the designed peak wavelength of 660 nm divided by $\sqrt{2}$. At this wavelength the transition from the backscattering regime happens and all shorter wavelengths are scattered in forward directions. The blue curve in Fig. 12B, which is discussed next, shows the backscattering

efficiency inside the material without consideration of any interface reflections (i.e., Fresnel reflections, including total internal reflection). In this case, the short-wavelength cutoff at around 467 nm is only caused by the above-mentioned transition from backward to forward scattering. The long-wavelength edge is found at approximately 660 nm as expected. In the regime between the two cutoffs the reflectivity increases with decreasing wavelength.

When reflections from interfaces are considered, the red curve in Fig. 12B results. For normal incidence, and given the effective refractive index of $\bar{n} = 1.5$, the red curve shows that total internal reflection of the scattered wave sets in at a wavelength of about 617 nm. This finding corresponds very well with the decrease of the reflectivity at the short-wavelength side of the peak from FIT simulation (black curve). The calculated peak in the red curve matches the peak in the simulated black curve in shape and – at least roughly – in amplitude. This confirms the validity of our approach and shows that total internal reflection may play a significant role for the selectivity of structural-color films.

At shorter wavelengths we observe deviations between the calculated red curve and the simulated black curve in Fig. 12B. As discussed before, these are due to multiple scattering which occurs for shorter wavelengths. Naturally, this is not included in our first-order calculation, but shows up in the brute force FIT-simulation. Specifically, there is a peak at wavelengths around 467 nm which is likely due to light scattered twice. The high relative strength of this secondary scattering can be explained by the film geometry. Light scattered at 90°, due to the infinite horizontal propagation path inside the film, has a probability of one to be scattered again eventually. Then half of that doubly scattered light will go upwards, thus potentially coupling out and adding to the reflected signal, and the other half will go downwards into the forward direction, either being absorbed or transported away reflection free. Wavelengths shorter than 467 nm are increasingly scattered into the forward direction which goes along with limiting of the propagation path again, thus reducing the probability for a second scattering event before the light can exit the film in the forward direction. Eventually, for very short wavelengths, where scattering only leads to small changes in the propagation direction of the wave, even multiple scattering events will not lead to reflections anymore.

We further obtain the cutoff wavelengths on both sides of the broad secondary peak by consecutively using the Ewald sphere construction twice (see Fig. 13). The total internal reflection preventing the coupling out of doubly scattered light in the backward direction (reflection regime) sets in at 374 nm for light that was initially scattered into a forward direction and at 544 nm wavelength for light that was initially scattered into a backward direction. These two wavelengths match the limits of the secondary scattering peak seen in the simulated reflectivity spectrum.

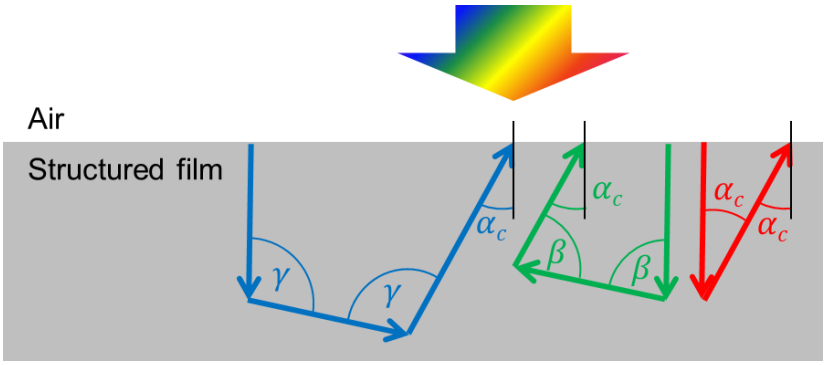


Fig. 13. Different ways of reaching the critical reflection angle after double or single scattering. The maximum (blue) and minimum (green) scattering angle where light after two scattering events hits the film interface under the angle of total internal reflection are shown. The wavelengths where scattering in the angles β and γ is expected can be calculated based on geometrical considerations. The results precisely match the edges of the second-order scattering peak observed in the simulated reflection spectrum (black curve in Fig. 12B). The red arrows indicate light of the wavelength where the reflection cutoff in the first-order scattering peak is observed due to total internal reflection at the inner film interface.

Whether the mechanisms described here might be responsible for the double-peaked reflectivity spectra often observed in bird feathers (e.g., [63]) remains to be clarified in future research. The main differences between the structures considered here and biological ones are the refractive-index contrast and their geometry. The biological structures are usually binary structures from keratin or chitin filled with air. The refractive-index contrast of $n_1/n_2 = 1.55$ [106] would lead to a stronger contribution of higher-order scattering than what is observed in our structures which makes the differentiation of the peaks more difficult.

Next, we investigate the use of the Ewald sphere construction in predicting the directions of the scattered light. We do so by comparing it to the scattering directions above the film calculated using FIT. To obtain the scattered intensities, for one wavelength the fields E_x, E_y, and E_z in an x-y-plane above the structure are Fourier transformed. Then the squared field amplitude in the k_x-k_y-plane can be found calculating

$$\hat{E}^2(k_x, k_y) = |\mathfrak{F}\{E_x\}|^2 + \left|\mathfrak{F}\{E_y\}\right|^2 + |\mathfrak{F}\{E_z\}|^2, \tag{84}$$

where $\mathfrak{F}$ denotes the 2D Fourier transform in the x-y-plane. From this, the scattered intensity distribution is found as $I = \hat{E}^2/(2Z_0)$.

The distributions for four different wavelengths are shown in Fig. 14. The Fourier transform decomposes the fields into a sum of plane waves. Each point in the diagram

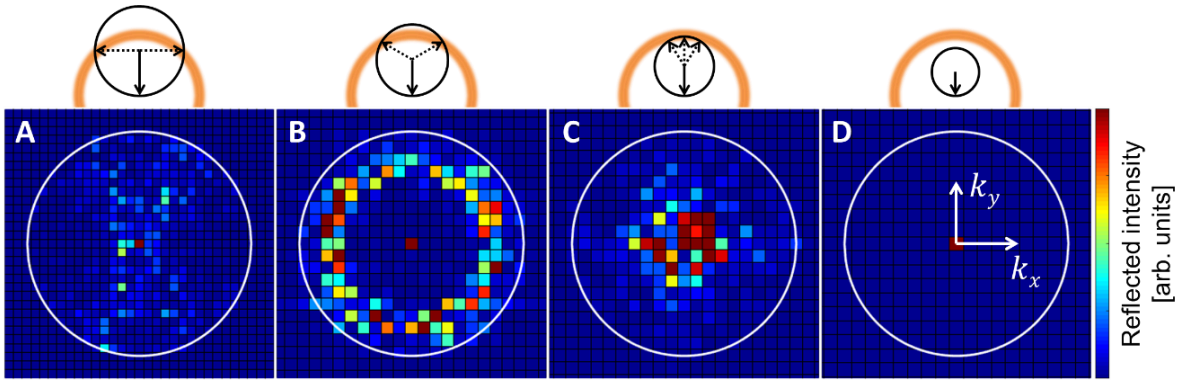


Fig. 14. Wavelength-dependent scattering directions of the simulated structure. The heatmap plots show the distribution of the backscattered intensity in the k_x-k_y-plane. Those k-vectors parallel to the film surface mark the maximum spatial frequency which is indicated by the white circle. The center points represent the incident and the Fresnel-reflected waves. They are propagating normally to the film interface and therefore correspond to a spatial frequency of zero in the k_x-k_y-plane. The shown wavelengths are A: 465 nm, B: 645 nm, C: 665 nm and D: 750 nm. They are selected to lie, respectively, in the second-order scattering peak, in the conical reflection regime, at the long-wavelength reflectivity edge of the main peak, and in the scattering-free spectral regime (cf. Fig. 12B). At the top the corresponding Ewald sphere construction for each case is shown schematically.

therefore corresponds to a plane wave with a direction of propagation given by the respective k_x and k_y. With this, k_z is implicitly given by $k_{\text{air}}^2 = k_x^2 + k_y^2 + k_z^2$, where k_{air} is the wave number of the incident and reflected waves in air, $k_{\text{air}} = |\mathbf{k}_0|/\bar{n} = |\mathbf{k}_1|/\bar{n}$. The white circle in each plot has a radius of k_{air} and therefore indicates the maximum possible k-vector length for propagating waves. Wave vectors on this circle correspond to directions parallel to the film surface, i.e., $k_{\text{air}}^2 = k_x^2 + k_y^2$ and $k_z = 0$. On the other hand, the center of the circle represents propagation normal to the film surface, i.e., $k_{\text{air}} = k_z$ and $k_x = k_y = 0$. The graphs are normalized to the length of k_{air} such that the radius of the white circles is the same for each graph. Note that the scattering angles in air and inside the film material are related to each other via Snell's law. With respect to the normal, light scattered inside the structure into the angular range between zero degree and the angle of total internal reflection is refracted into the full angular range between zero and 90° in air.

From the Ewald sphere construction a diffusive distribution of k-vectors is expected in the secondary scattering peak because after two scattering events there is hardly a preferential direction anymore [67]. The simulated k-vector distribution at a wavelength of 465 nm is shown in Fig. 14A. The slight anisotropy in the distribution can be attributed to the polarized excitation and polarization-dependent Fresnel reflection. Towards longer

wavelengths single scattering predominates, and the scattered wave vectors are expected to lie on the surface of a gradually closing cone. Fig. 14B shows the k-vector distribution at 645 nm where a clear ring is seen. This means that light is mainly scattered for a certain $k_r^2 = k_x^2 + k_y^2$ which corresponds to a scattering angle α with respect to the plane normal, $k_r = k_0 \sin\alpha$. At 660 nm or slightly above, where the Ewald sphere just touches the k-shell, a filled spot in the wave vector distribution is observed, corresponding to a narrower but fully filled cone of scattering angles (Fig. 14C at 665 nm). For even longer wavelengths, neither backward nor forward scattering occurs anymore, and all light is transmitted. In this case the Ewald sphere does no longer intersect with the k-shell due to its decreased radius. The residual reflectivity is only caused by the weak Fresnel reflection from the film surface in normal backward direction, which corresponds to the origin in the k_x-k_y-plane (Fig. 14D at 750 nm). With these results being in line with the predictions of the Ewald sphere construction, we show that it can serve as a useful tool to predict the scattering directions in structural colors.

3.6 Chapter conclusions

We have shown the applicability of the first-order Born approximation and the Ewald sphere construction to effectively describe scattering in disordered structures used to realize structural colors. We have applied them to predict several features in the scattering of light normally incident on a structural-color film, such as a sharp reflectivity edge towards long wavelengths, an opening scattering angle towards shorter wavelengths and finally the transition into multiple scattering. We further showed that total internal reflection of scattered light at the film surface leads to a suppression of backscattered light even for wavelengths where the scattering as such would still admit backscattering. This effect leads to the formation of a narrow spectral peak with a sharp edge on the short-wavelength side and thus increases the spectral selectivity of the reflection. With our approach the peak position and amplitude could be well predicted. The remaining mismatches towards shorter wavelengths could be explained by double scattering, emphasized by the film geometry. The vivid geometrical representation of the Ewald sphere and its simple numerical applicability thus make the Ewald sphere construction an excellent tool to study structural colors and other scattering problems.

As stated before, we only consider normal incidence of light on the scattering film, but in realistic situations the illumination is often diffuse. While the full numerical simulation of such a scenario poses quite a challenge, it should be much simpler to add up the reflectivity predicted by the first-order approximation for several incidence directions to

get a good approximation of the total scattering. This is, however, beyond the scope of this work and remains to be investigated.

Another thing to note is that the presented approach works best for weak overall scattering. However, the directions of scattering in dependence on the wavelength can still roughly be estimated by the Ewald sphere construction even for structures which scatter light more strongly. E.g., we used this for the optimization of artificial structural colors based on photonic glasses [35]. For a thick, disordered structure with weak local scattering, a combined approach could be implemented, where the Ewald sphere construction is used to predict the angular distribution of each scattering event in a Monte Carlo ray tracing simulation. Such an approach could also be used for structures producing strong reflectivity contrasts. A similar direction was followed after the publication of our work and will be further commented on in the final chapter of this thesis.

4 Complete photonic bandgaps in quasiperiodic structures

This chapter covers the second of the two major blocks of original work presented in this thesis. The main results of this work were published in reference [107]. The results and figures presented here are partly taken from the publication.

The experimental part of the work presented in chapter 4.6 was done by Mikhail S. Sidorenko and Ruslan R. Yafyasov from Mikhail V. Rybin's group at the ITMO university, St. Petersburg, before 2022. The contributions are again described in more detail at the beginning of that chapter.

Some initial results of this work were obtained by Timo Sommer in the framework of his bachelor thesis "Localization of Light in Isotropic Omnidirectional Bragg Gratings" under my supervision.

4.1 Introduction

In the previous chapter we considered disordered quasiperiodic structures where the directions of the gratings generating the underlying distribution are randomly distributed. In this part now, we want to increase the control over the randomness of the considered structures by imposing stricter limitations on these directions.

As already mentioned in the introduction (chapter 2.3.1) one of the main properties of photonic crystals is their photonic bandgap (PBG) [1, 24, 108, 109]. Photonic crystals can open a PBG for certain directions with a low refractive-index contrast. However, it is often required that a PBG exists in all directions (omnidirectional PBG), or additionally for all polarizations (complete PBG, CPBG). For this, the different directional bandgaps need to overlap. There are two main mechanisms to achieve this: The first one is to increase the width of the directional gaps. While this can be achieved by an increase of the refractive-index contrast, it is strictly limited by the available materials. The other one is to make the Brillouin zone as circular or spherical as possible, corresponding to an as high as possible degree of symmetry for crystals (but not necessarily for non-crystalline structures) [9, 110, 111]. To increase the range of available materials to be used in PBG applications, there have been considerable efforts to minimize the required refractive-index contrast.

In simple photonic crystals based on Bravais lattices the rotational symmetry is fundamentally limited. The lowest refractive-index contrast where a CPBG was found is $n_1/n_2 = 2.63/1 = 2.63$ for hexagonal 2D structures [1, 112]. In 3D structures based on a face-centered cubic lattice even a refractive-index contrast of 3.5 was not sufficient [113]. Optimization of the permittivity distribution in the unit cell of the photonic crystal can be used to modify the distribution of the Bragg peaks in reciprocal space and thereby to shape a more circular or spherical effective Brillouin zone [35]. The minimal contrast numerically demonstrated for such a modified photonic crystal in 2D is 1.16 for an omnidirectional bandgap for transverse magnetic (TM) polarization in a holographic structure [40], and 2.1 for a CPBG in honeycomb-based structures [111]. For 3D structures a minimal contrast of 1.88 was obtained in an optimized diamond structure [1, 110, 113].

To overcome the symmetry limitations of photonic crystals, photonic quasicrystals have been investigated [42, 114, 115]. 2D quasicrystals based on aperiodic tilings with up to 14-fold symmetry have been shown [116]. The realization of a CPBG in a 2D quasicrystal with 12-fold symmetry at a refractive-index contrast down to 1.45 has been controversially discussed [33, 101, 117]. It was later stated that such a 12-fold quasicrystal still requires a contrast of 2.65 [117], which is no improvement over the 2D triangular photonic crystal. On the other hand, an omnidirectional PBG for a single polarization was found at an extremely low contrast of approximately 1.1 in 10-fold (called 5-fold by the authors) and 12-fold quasicrystals [42].

For 3D, quasicrystals based on an icosahedral tiling with 30 Bragg peaks have been shown [9]. However, the strength of the corresponding 15 Bragg gratings was not sufficient to open up a CPBG with a refractive-index contrast of 1.61 [9]. Though localization was discussed later for a similar structure with refractive-index contrast of 1.64 no CPBG was demonstrated [118].

A CPBG can also be obtained in disordered structures without long-range order at a sufficient refractive-index contrast. A disordered 3D arrangement of monodisperse spheres shows an exponential suppression of the local density of states (LDOS) for refractive-index contrasts down to 2.4 [119]. Similarly, in 2D hyperuniform disordered structures a CPBG with a contrast of 3.4 [120] as well as an omnidirectional bandgap for the transverse electric (TE) polarization at a contrast of 1.6 [121] have been shown.

Especially in 2D, structures with a strongly position-dependent mode density can be envisaged. E.g., an onion-like structure of concentric dielectric shells provides a strong suppression of the spontaneous emission of light emitters placed in its center [122]. Also, aperiodic structures around a certain origin like Fermat's spiral can be shown to possess

wide frequency ranges of strong emission suppression for an emitter placed close to their origin [123]. However, the use of such structures is limited to a small volume around their center. We will therefore not discuss them in further detail.

In contrast to the aforementioned approaches, our model structure based on overlapping gratings is mostly homogeneous regarding its optical properties[10] and fully flexible regarding the number of Bragg peaks and their orientation. This allows us to position the peaks at equal distances to the origin of reciprocal space and in an angular distribution that fills the spherical shell of peaks as homogeneously as possible. Based on this, we present a mathematical first-order approximation for the bandgap that yields two important results: that there is a finite optimal number of gratings for any finite available refractive-index contrast, and that a CPBG can be obtained for any, even arbitrarily small refractive-index contrast. The predictions of the model are confirmed by numerical simulations in 2D. The same design rule proves successful in 3D where an unprecedented emission suppression of $-10\,\mathrm{dB}$ is shown with a refractive-index contrast of $n_1/n_2 = 1.38$ A strong suppression of light transport is also confirmed in microwave transmission measurements conducted on a 3D-printed structure with RI contrast $n_1/n_2 = 1.59$. The main results of our work were published in reference [107].

4.2 Model structure

The quasiperiodic structures we used for the realization of a CPBG are again generated by a superposition of sinusoidal 1D gratings. However, in this case it is of particular importance that the grating directions are distributed over the whole angular range as homogeneously as possible. For the 2D case this can easily be realized by a uniform distribution over the azimuthal angle. 3D structures need a more complex distribution of gratings, which will be discussed later. As before, the structure is mathematically described by a gradual function:

$$n_g(\mathbf{r}) = \bar{n} + \Delta n_g(\mathbf{r}) = \bar{n} + \sum_{i=1}^{N} \Delta n_i \cos(\mathbf{b}_i \cdot \mathbf{r} + \phi_i). \tag{85}$$

As for the structural-color model structure, the same period a and amplitude Δn_i is used for each grating, and the phases ϕ_i are chosen randomly.

In the next step we want to obtain a binary structure that can be represented by two materials. This makes manufacturing of the structure much easier and also makes our

[10] When probing the emission suppression of the structure we do see some dependence on the probe's local environment and its polarization. The relative suppression is very homogeneous, though.

results more comparable to previous studies. The sum in Eq. (85) is therefore binarized by a sign function (cf. [38–40, 42, 43]):

$$n_b(\mathbf{r}) = \bar{n} + \Delta n_b(\mathbf{r}) = \bar{n} + \Delta n \,\mathrm{sgn}\left(\Delta n_g(\mathbf{r})\right), \tag{86}$$

where Δn is the refractive-index perturbation from the average value $\bar{n}$ such that $n_1 = \bar{n} + \Delta n$ and $n_2 = \bar{n} - \Delta n$. Two examples of the structure in 2D and 3D are presented in Fig. 15.

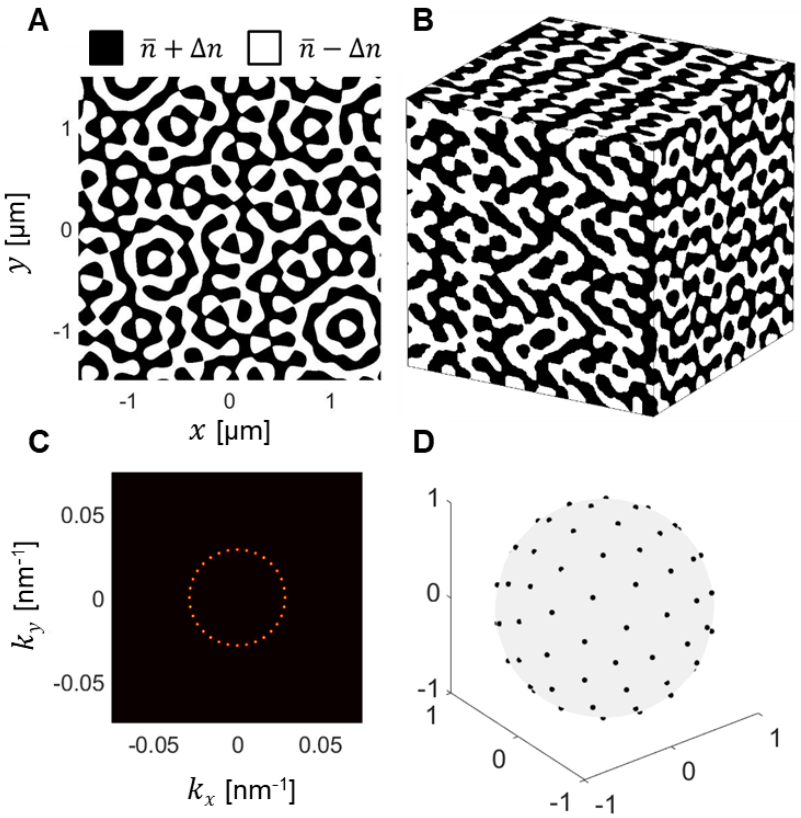


Fig. 15. Quasiperiodic structures in real and reciprocal space. A, B: Examples of the investigated structures in 2D and 3D, respectively. The side lengths in both cases are approximately 13 periods a. The 2D image was generated based on an overlap of 16 gratings; the 3D image is based on 46 gratings. C: Squared Fourier transform of a circular excerpt of a 2D structure. D: Schematic representation of the Bragg peaks used for the 3D structure.

Before the binarization step, all energy in reciprocal space is in the Bragg peaks only. To find how much energy is left in the Bragg peaks after binarization we calculate the correlation integral of $\Delta n_g(\mathbf{r})$ and $\Delta n_b(\mathbf{r})$ over a large volume V:

$$C = \int_V \Delta n_g(\mathbf{r})\, \Delta n_b(\mathbf{r}) d\mathbf{r} = \Delta n \int_V \left|\Delta n_g(\mathbf{r})\right| d\mathbf{r}. \tag{87}$$

We may now choose to integrate over the possible values of the refractive index weighted by their probability $P(\Delta\tilde{n}_g)$ instead:

$$\begin{aligned} C &= \Delta n \int_V \left|\Delta n_g(\mathbf{r})\right| d\mathbf{r} = V\Delta n \int_{-\infty}^{+\infty} \left|\Delta\tilde{n}_g\right| P(\Delta\tilde{n}_g)\, d\Delta\tilde{n}_g \\ &= 2V\Delta n \int_0^{+\infty} \Delta\tilde{n}_g P(\Delta\tilde{n}_g)\, d\Delta\tilde{n}_g. \end{aligned} \tag{88}$$

As introduced in chapter 3.3, for the graded structure with a large number of gratings the deviation of the refractive index from the mean refractive index $\bar{n}$ is normally distributed with a mean value of zero and a standard deviation of σ_g, i.e.,

$$P\left(\Delta\tilde{n}_g\right) = \frac{1}{\sigma_g\sqrt{2\pi}} \exp\left(-\frac{\left(\Delta\tilde{n}_g\right)^2}{2\sigma_g^2}\right). \tag{89}$$

The integral in Eq. (88) can then be solved and yields

$$C = \sqrt{\frac{2}{\pi}}\sigma_g \Delta n V. \tag{90}$$

If we, in contrast, look at the self-correlation function of $\Delta n_g(\mathbf{r})$, we find that

$$C_0 = \int_V \left|\Delta n_g(\mathbf{r})\right|^2 d\mathbf{r} = \sigma_g^2 V. \tag{91}$$

The grating amplitudes of the graded structure can be freely chosen, and we set $\sigma_g = \Delta n$. In this case the self-correlation integrals of the graded and the binarized structure have the same value. Comparing Eq. (90) and (91) it can be seen that the binarization leads to a structure that has a $\sqrt{2/\pi} \approx 80\%$ similarity with the graded structure. Due to Parseval's theorem, a similar argument can be made in reciprocal space. Then it becomes clear that this similarity can only be evaluated in the main Bragg peaks since the Fourier transform of the graded structure is otherwise zero. If we look at the square of the Fourier transforms instead, which is the relevant parameter to evaluate the scattering in the quasiperiodic structure, we get $2/\pi \approx 64\%$ energy inside the Bragg peaks of the binarized structure.

We looked at the Fourier transforms of actual structures that we numerically generated and could confirm this estimation. Fig. 16 shows the ratio of the Fourier transforms of a

graded and a binary structure. The range around 0.8 is highlighted in red. We see that in all peaks the ratio is inside the red range.

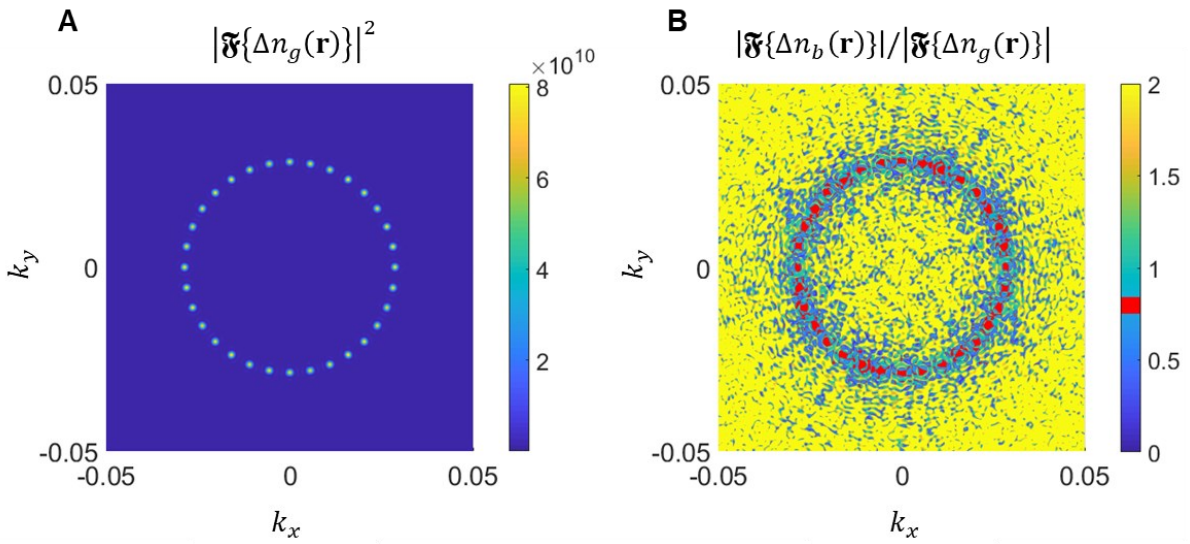


Fig. 16. Influence of the structure binarization on the Bragg peak strength. A: Squared Fourier transform of the graded structure clearly showing the positions of the Bragg peaks. B: Ratio of the Fourier transforms of the graded and the binarized structure. The value range of approximately 0.75 to 0.84 is highlighted in red. The ratio in all the Bragg peaks lies in this range which is close to the expected $\sqrt{2/\pi}$.

Combining this estimation with the factor of $\sqrt{N/2}$, found in chapter 3.3 for the relation of the individual grating contrast to the overall structure contrast, each grating underlying the binarized structure effectively has an amplitude equal to $\Delta n_{i,b} = 2\Delta n/\sqrt{\pi N}$. The binarization also introduces additional Bragg peaks in Fourier space that take the residual approximate 36% of the energy. However, for a large number of gratings these peaks are so densely distributed that for a finite structure size they cannot be differentiated anymore (see Fig. 15C). Thus, we efficiently utilize the refractive-index contrast of the binarized structure to generate the required Bragg peak distribution.

4.3 Bandgap estimation

While every individual grating has a bandgap in its normal direction, other directions see an upshifted bandgap, corresponding to the Bragg condition. Thus, in the direction in between two Bragg peaks the bandgap is at a slightly larger frequency. An omnidirectional bandgap for one polarization is achieved when the directional bandgaps have a sufficient opening to overlap.

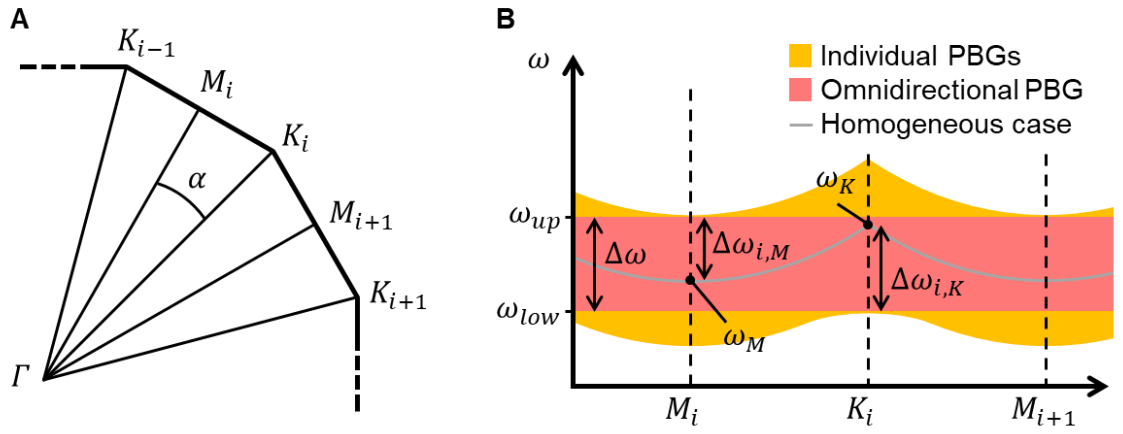


Fig. 17. Formation of the CPBG from several individual grating bandgaps. A: Schematic representation of a section of the effective Brillouin zone of the 2D quasiperiodic structures. B: Schematic band diagram showing the effective bandgaps in different directions. The bands depicted in gray show the band positions for the empty lattice case, when the grating contrast converges to zero. The orange shaded area represents the bandgap opening when a finite contrast is assumed. The red shaded area represents the omnidirectional PBG.

The effective Brillouin zone of our structure is schematically shown in Fig. 17A. We label the direction towards the Bragg peak of the grating with index i as ΓM_i and the direction in between the two Bragg peaks with indices i and $i+1$ as ΓK_i. Scanning the band diagram along the edge of the effective Brillouin zone, the omnidirectional PBG opening can be evaluated (Fig. 17B). To achieve an omnidirectional PBG, the upper edge of the PBG in ΓM_i-direction should be above the lower edge of the PBG in ΓK_i-direction.

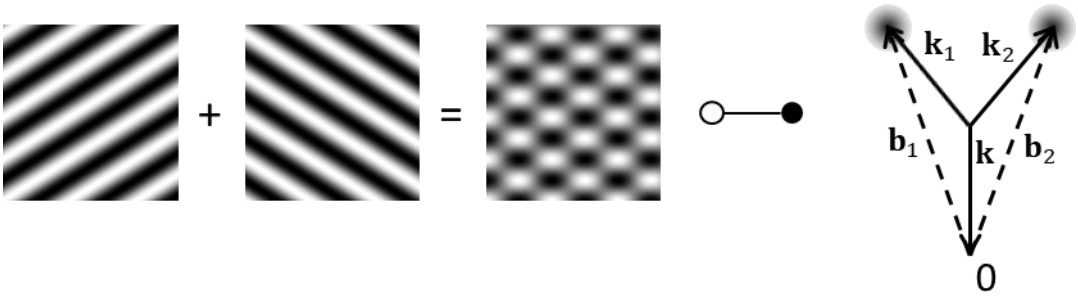


Fig. 18. Connection of grating directions and scattering directions. Two overlapping gratings with directions $\mathbf{b}_1$ and $\mathbf{b}_2$ in real (left) and reciprocal (right) space lead to scattering in the directions depicted as $\mathbf{k}_1, \mathbf{k}_2$.

At the M-points we neglect the interaction with other gratings in the calculation of the directional bandgap of the single grating. At the K-points the neighboring gratings are equally contributing to the bandgap opening. The influence of their interaction can be estimated analytically using a simplified structure with only two gratings and analyzing

the bandgap opening for light propagating in the central direction between the grating vectors. This situation is depicted in Fig. 18. Further gratings at larger angles would primarily scatter at higher frequencies and are therefore omitted.

The frequency shift due to a small perturbation $\Delta\tilde{\varepsilon}(\mathbf{r})$ of an otherwise constant permittivity $\bar{\varepsilon}$ can be described as (see Eq. (26) or reference [1])

$$\Delta\omega = -\frac{\omega}{2}\frac{\int \Delta\tilde{\varepsilon}(\mathbf{r})\mathbf{E}(\mathbf{r})\mathbf{E}^*(\mathbf{r})d^3\mathbf{r}}{\int \bar{\varepsilon}\mathbf{E}(\mathbf{r})\mathbf{E}^*(\mathbf{r})d^3\mathbf{r}}. \tag{92}$$

The $\Delta\tilde{\varepsilon}$-term is the superposition of the two gratings $\Delta\tilde{\varepsilon}_1$ and $\Delta\tilde{\varepsilon}_2$ and can be written as

$$\Delta\tilde{\varepsilon} = \Delta\tilde{\varepsilon}_1 + \Delta\tilde{\varepsilon}_2 = \Delta\varepsilon_1 \cos(\mathbf{b}_1\mathbf{r} + \phi_1) + \Delta\varepsilon_2 \cos(\mathbf{b}_2\mathbf{r} + \phi_2). \tag{93}$$

As for the actual model structure, we set the perturbation strength of the gratings to be equal, i.e., $\Delta\varepsilon_1 = \Delta\varepsilon_2$. The Bragg condition is fulfilled for both gratings in K-direction and the scattered light is propagating with wave vectors $\mathbf{k}_1$ and $\mathbf{k}_2$ as depicted in Fig. 18. The total electric field can now be described as a superposition of the different components,

$$\mathbf{E} = \mathbf{E}_0\left(\exp(i\mathbf{k}\mathbf{r}) + \frac{1}{\sqrt{2}}\exp\big(i(\mathbf{k}_1\mathbf{r} + \gamma_1)\big) + \frac{1}{\sqrt{2}}\exp\big(i(\mathbf{k}_2\mathbf{r} + \gamma_2)\big)\right). \tag{94}$$

The angle between the gratings is assumed to be very small. Therefore, the factors of $1/\sqrt{2}$ in the second and third term represent the fact that no power is transported at frequencies near the band-edge (zero group velocity).

The $\mathbf{E}\mathbf{E}^*$-terms in Eq. (92) can now be written as

$$\begin{aligned}
\mathbf{E}\mathbf{E}^* = \mathbf{E}_0^2\Big(&1 + \frac{1}{2} + \frac{1}{2} \\
&+ \frac{1}{\sqrt{2}}\exp\big(i(\mathbf{k}\mathbf{r} - \mathbf{k}_1\mathbf{r} - \gamma_1)\big) + \frac{1}{\sqrt{2}}\exp\big(i(\mathbf{k}\mathbf{r} - \mathbf{k}_2\mathbf{r} - \gamma_2)\big) \\
&+ \frac{1}{\sqrt{2}}\exp\big(-i(\mathbf{k}\mathbf{r} - \mathbf{k}_1\mathbf{r} - \gamma_1)\big) + \frac{1}{\sqrt{2}}\exp\big(-i(\mathbf{k}\mathbf{r} - \mathbf{k}_2\mathbf{r} - \gamma_2)\big) \\
&+ \frac{1}{2}\exp\big(i(\mathbf{k}_1\mathbf{r} + \gamma_1 - \mathbf{k}_2\mathbf{r} - \gamma_2)\big) + \frac{1}{2}\exp\big(-i(\mathbf{k}_1\mathbf{r} + \gamma_1 - \mathbf{k}_2\mathbf{r} - \gamma_2)\big)\Big) \\
= \mathbf{E}_0^2\big(&2 + \sqrt{2}\cos(\mathbf{k}\mathbf{r} - \mathbf{k}_1\mathbf{r} - \gamma_1) + \sqrt{2}\cos(\mathbf{k}\mathbf{r} - \mathbf{k}_2\mathbf{r} - \gamma_2) \\
&+ \cos(\mathbf{k}_1\mathbf{r} - \mathbf{k}_2\mathbf{r} + \gamma_1 - \gamma_2)\big) \\
= \mathbf{E}_0^2\big(&2 + \sqrt{2}\cos(\mathbf{b}_1\mathbf{r} + \gamma_1) + \sqrt{2}\cos(\mathbf{b}_2\mathbf{r} + \gamma_2) \\
&+ \cos\big((\mathbf{k}_1 - \mathbf{k}_2)\mathbf{r} + \gamma_1 - \gamma_2\big)\big),
\end{aligned} \tag{95}$$

where the vector relations depicted in Fig. 18 were used. Together with Eq. (93) and using the fact that the phase of the fields will be matched with the gratings ($\phi_m = \gamma_m$ for $m \in \{1,2\}$) we can write the integral in the numerator of Eq. (92) as

$$\begin{aligned}\int_V \Delta\tilde{\varepsilon}\mathbf{E}\mathbf{E}^* d^3\mathbf{r} = \Delta\varepsilon_1 \int_V \big(&2\cos(\mathbf{b}_1\mathbf{r}+\phi_1) + 2\cos(\mathbf{b}_2\mathbf{r}+\phi_2) \\ &+ \sqrt{2}\cos^2(\mathbf{b}_1\mathbf{r}+\phi_1) + \sqrt{2}\cos(\mathbf{b}_1\mathbf{r}+\phi_1)\cos(\mathbf{b}_2\mathbf{r}+\phi_2) \\ &+ \sqrt{2}\cos^2(\mathbf{b}_2\mathbf{r}+\phi_2) + \sqrt{2}\cos(\mathbf{b}_2\mathbf{r}+\phi_2)\cos(\mathbf{b}_1\mathbf{r}+\phi_1) \\ &+ \cos(\mathbf{b}_1\mathbf{r}+\phi_1)\cos\big((\mathbf{k}_1-\mathbf{k}_2)\mathbf{r}+\phi_1-\phi_2\big) \\ &+ \cos(\mathbf{b}_2\mathbf{r}+\phi_2)\cos\big((\mathbf{k}_1-\mathbf{k}_2)\mathbf{r}+\phi_1-\phi_2\big)\big) d^3\mathbf{r}.\end{aligned} \tag{96}$$

When the integration is carried out over a large volume V, all terms in the integral except for the $\cos^2$-terms average out to zero. The result after integration is

$$\int_V \Delta\tilde{\varepsilon}\mathbf{E}\mathbf{E}^* d^3\mathbf{r} = \sqrt{2}\mathbf{E}_0^2 V \Delta\varepsilon_1. \tag{97}$$

With the same reasoning we find the denominator to be

$$\int_V \bar{\varepsilon}\mathbf{E}\mathbf{E}^* d^3\mathbf{r} = 2\mathbf{E}_0^2 V \bar{\varepsilon}. \tag{98}$$

Plugging this into Eq. (92) yields

$$\frac{\Delta\omega_K}{\omega} = \frac{\sqrt{2}}{4}\frac{\Delta\varepsilon_1}{\bar{\varepsilon}} = \frac{\sqrt{2}}{2}\frac{\Delta n_1}{\bar{n}}. \tag{99}$$

Note that the $\Delta\omega_K$ here just represents the one-sided shift of one of the bands due to the perturbation, i.e., half of the bandgap. This deviates from the expression for the band shift of a single grating by the factor $\sqrt{2}$.

If we do the same calculation as above for a 3D structure where three instead of two gratings interact, we find a factor of $\sqrt{3}$ and the same considerations would hold true for higher dimensions. We therefore conclude that the PBG opening is by a factor $\sqrt{m}$ larger than for a single grating, where m is the number of interacting gratings (2 or 3 for 2D or 3D structures, respectively).

With this basis, we are now equipped to find an expression for the bandgap opening $\Delta\omega = \omega_{up} - \omega_{low}$, as depicted in Fig. 17B. The approach is similar to the one presented in reference [41] for a graded-index structure. The upper bandgap edge is found at

$$\omega_{up} = \omega_M + \frac{1}{2}\frac{\Delta n_{i,b}}{\bar{n}}\omega_M, \tag{100}$$

where $\omega_M = k_{\Gamma M}c/\bar{n}$ is the zero-contrast band frequency in the M-point. Accordingly,

$$\omega_{low} = \omega_K - \frac{\sqrt{m}}{2}\frac{\Delta n_{i,b}}{\bar{n}}\omega_K, \tag{101}$$

where $\omega_K = k_{\Gamma K}c/\bar{n}$ is the zero-contrast band frequency in the K-point. Now the absolute bandwidth can be expressed as

$$\Delta\omega = \omega_M + \frac{1}{2}\frac{\Delta n_{i,b}}{\bar{n}}\omega_M - \left(\omega_K - \frac{\sqrt{m}}{2}\frac{\Delta n_{i,b}}{\bar{n}}\omega_K\right). \tag{102}$$

Applying the relation $k_{\Gamma K} = k_{\Gamma M}/\cos\alpha$, where α is the angle between ΓM_i- and ΓK_i-directions (see Fig. 17A), we obtain

$$\frac{\Delta\omega}{\omega_M} = 1 + \frac{1}{2}\frac{\Delta n_{i,b}}{\bar{n}} - \frac{1}{\cos\alpha} + \frac{\sqrt{m}}{2}\frac{\Delta n_{i,b}}{\bar{n}}\frac{1}{\cos\alpha}. \tag{103}$$

For small α the cosine term can be expressed by the series expansion $1/\cos\alpha \approx 1 + \alpha^2/2$:

$$\frac{\Delta\omega}{\omega_M} = \left(\frac{1+\sqrt{m}}{2}\right)\frac{\Delta n_{i,b}}{\bar{n}} - \frac{\alpha^2}{2} + \frac{\sqrt{m}}{2}\frac{\Delta n_{i,b}}{\bar{n}}\frac{\alpha^2}{2}. \tag{104}$$

Since we assume that many gratings are used for the generation of the structure, we may set $\omega_M \approx \omega$, where ω is the midgap frequency of the bandgap. Since α and $\Delta n_{i,b}$ are both assumed to be small, the last term can be neglected:

$$\frac{\sqrt{m}}{2}\frac{\Delta n_{i,b}}{\bar{n}}\frac{\alpha^2}{2} \approx 0. \tag{105}$$

With this, and using $\Delta n_{i,b} = 2\Delta n/\sqrt{\pi N}$ as derived previously, the following general expression for the relative bandgap opening can be obtained:

$$\frac{\Delta\omega}{\omega} = \left(\frac{1+\sqrt{m}}{2}\right)\sqrt{\frac{4}{\pi}}\frac{\Delta n}{\bar{n}\sqrt{N}} - \frac{\alpha^2}{2}. \tag{106}$$

Now the angle α can be expressed in terms of the grating number N, leading to an expression solely depending on the refractive-index values and the number of gratings. We need to treat the 2D and 3D case separately, as they show different relations between

the angle α and the grating number N. In 2D a uniform distribution of the grating directions, and therefore of the Bragg peaks, over the half circle is straight-forward and leads to the relation $\alpha = \pi/(2N)$. Plugging this into Eq. (106) yields an expression for the relative bandgap opening:

$$\frac{\Delta\omega_{2D}}{\omega} = \left(\frac{1+\sqrt{2}}{2}\right)\sqrt{\frac{4}{\pi}}\frac{\Delta n}{\bar{n}\sqrt{N}} - \frac{\pi^2}{8N^2}. \tag{107}$$

This function has a maximum at a grating number of

$$N_{2D,opt} = \pi^{\frac{5}{3}}\left(\frac{1}{2+2\sqrt{2}}\right)^{\frac{2}{3}}\left(\frac{\bar{n}}{\Delta n}\right)^{\frac{2}{3}} \approx 2.359\left(\frac{\bar{n}}{\Delta n}\right)^{\frac{2}{3}}, \tag{108}$$

and the bandgap opening at this grating number is

$$\frac{\Delta\omega_{2D}}{\omega}\left(N_{opt}\right) = \frac{3}{8}\left(\frac{2}{\pi}\left(1+\sqrt{2}\right)\right)^{\frac{4}{3}}\left(\frac{\Delta n}{\bar{n}}\right)^{\frac{4}{3}} \approx 0.665\left(\frac{\Delta n}{\bar{n}}\right)^{\frac{4}{3}}. \tag{109}$$

Significantly, the bandgap opening will converge to zero as the contrast goes to zero, but for finite contrast values there will always be a finite omnidirectional PBG.

The grating distribution in 3D is, just like the distribution in 2D, supposed to cover all available directions as evenly as possible in order to maximize the width of the bandgap. To achieve this, we used an icosahedral distribution aiming for optimal coverage. This is described in more detail in the 3D results section below (chapter 4.5.2). The distribution we used is a numerically found one and as such impossible to describe analytically. Since we want to analytically relate the angular separation of grating directions to the number of gratings, we need an approximation for the angle distribution.

We used a simple approximation that tends to slightly underestimate the maximum angular separation of Bragg peaks by assuming that the Bragg peaks are homogeneously distributed in a hexagonal pattern. In this case every Bragg peak has six neighboring Bragg peaks at equal distance, and the effective Brillouin zone is approximated by a polyhedron with equal hexagonal facets. In reality, the distribution closest to this approximation would be one with a Goldberg polyhedron as its effective Brillouin zone, which would also have 12 pentagonal faces and differently sized hexagons [124, 125]. Thus, the maximum angular separation is slightly larger in a real situation. For a large number of gratings, we disregard this deviation.

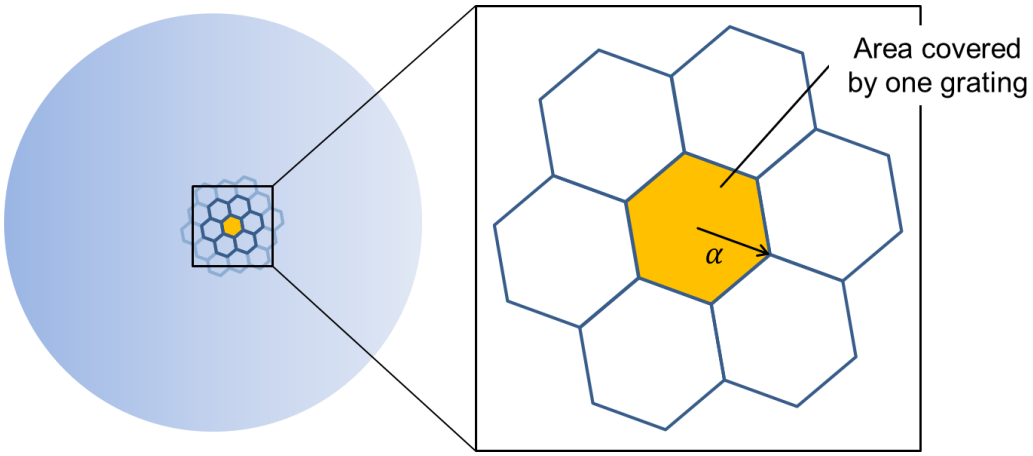


Fig. 19. Schematic representation of the effective 3D Brillouin zone approximated with only hexagonal facets.

The solid angle of each hexagonal facet can then be estimated as $\Omega = 4\pi/(2N)$. This solid angle is connected to the angle α between a Bragg peak and the center point between the Bragg peak and its neighbors (Fig. 19) as

$$\Omega = \frac{3\sqrt{3}}{2}\alpha^2. \tag{110}$$

Combined, these equations yield

$$\alpha^2 = \frac{4\pi}{3\sqrt{3}N}. \tag{111}$$

With this result and Eq. (106) we again obtain the expressions for the relative bandgap opening, the optimum grating number as well as the optimum bandgap opening:

$$\frac{\Delta\omega_{3D}}{\omega} = \left(\frac{1+\sqrt{3}}{2}\right)\sqrt{\frac{4}{\pi}}\frac{\Delta n}{\bar{n}\sqrt{N}} - \frac{2\pi}{3\sqrt{3}N}, \tag{112}$$

$$N_{3D,opt} = \frac{1}{2+\sqrt{3}}\frac{8\pi^3}{27}\left(\frac{\bar{n}}{\Delta n}\right)^2 \approx 2.462\left(\frac{\bar{n}}{\Delta n}\right)^2, \tag{113}$$

$$\frac{\Delta\omega_{3D}}{\omega}(N_{opt}) = \left(1+\frac{2}{\sqrt{3}}\right)\frac{9}{4\pi^2}\left(\frac{\Delta n}{\bar{n}}\right)^2 \approx 0.491\left(\frac{\Delta n}{\bar{n}}\right)^2. \tag{114}$$

Again, the predicted bandgap persists for any finite refractive-index contrast.

We now have the theoretical basis to describe the generation of an omnidirectional bandgap. However, for a PBG to be complete it needs to inhibit propagation for all possible light polarizations. In 2D, the polarizations are fully described by an orthogonal basis of

TE and TM polarizations. For low-refractive-index media the shift between the bandgaps observed in TE and TM excitation is mainly caused by the different effective mean refractive index of the structure.

For TM polarized light the E-field is always tangential to the material boundaries and therefore continuous. The electric displacement D however is averaged between the two different permittivities:

$$\bar{\varepsilon}_{TM} = \frac{\bar{D}}{\bar{E}} = \frac{\frac{1}{2}\varepsilon_1 E + \frac{1}{2}\varepsilon_2 E}{E} = \frac{\varepsilon_1 + \varepsilon_2}{2} = \varepsilon_1 + \Delta\varepsilon, \tag{115}$$

where $\Delta\varepsilon = (\varepsilon_2 - \varepsilon_1)/2$.

For TE polarized light E and D can have all orientations towards the boundaries. However, in order to calculate the maximum difference between the effective permittivities for the two polarizations we may assume that all fields are normal to the boundaries. For that case we obtain:

$$\bar{\varepsilon}_{TE} = \frac{\bar{D}}{\bar{E}} = \frac{D}{\frac{D}{2\varepsilon_1} + \frac{D}{2\varepsilon_2}} = \frac{2\varepsilon_1\varepsilon_2}{\varepsilon_1 + \varepsilon_2} = \frac{\varepsilon_1 + 2\Delta\varepsilon}{1 + \frac{\Delta\varepsilon}{\varepsilon_1}}, \tag{116}$$

which can then be expressed into a Taylor series,

$$\bar{\varepsilon}_{TE} \approx (\varepsilon_1 + 2\Delta\varepsilon)\left(1 - \frac{\Delta\varepsilon}{\varepsilon_1} + \left(\frac{\Delta\varepsilon}{\varepsilon_1}\right)^2 - \cdots\right) \approx \varepsilon_1 + \Delta\varepsilon - \frac{(\Delta\varepsilon)^2}{\varepsilon_1}, \tag{117}$$

where terms containing third or higher powers of $\Delta\varepsilon$ were neglected. The difference in effective permittivities for the two polarizations is thus found to be

$$\Delta\varepsilon_p = \bar{\varepsilon}_{TM} - \bar{\varepsilon}_{TE} = \frac{(\Delta\varepsilon)^2}{\varepsilon_1} \approx \frac{(\Delta\varepsilon)^2}{\bar{\varepsilon}}. \tag{118}$$

Since the difference is very small, $\Delta\varepsilon_p = 2\Delta n_p \bar{n}$ as well as $\Delta\varepsilon = 2\Delta n \bar{n}$ hold. The relative difference between the bandgap positions for the different polarizations is then found as

$$\frac{\Delta\omega_p}{\omega} = \frac{\Delta n_p}{\bar{n}} = \frac{\Delta\varepsilon_p}{2\bar{n}^2} = 2\left(\frac{\Delta n}{\bar{n}}\right)^2. \tag{119}$$

In the 2D case the discrepancy between the bandgap positions for TM and TE polarization decreases faster than the maximal bandgap width for decreasing refractive-index contrast. Thus, for low refractive-index contrasts a better overlap of the bandgaps and thus a CPBG can be expected. For 3D structures the scaling power law with an exponent

of 2 is the same and a better estimation is required to predict the existence of a CPBG. At the same time, the assumption that electric fields are only either parallel or orthogonal to interfaces represents an extreme case that will not be present in real field distributions. Therefore, in reality the birefringence will be smaller in the 3D structures, and it might be that obtaining a CPBG is still possible.

4.4 Simulation method

Simulations were done using the time domain solver of CST Studio Suite [46]. A short linear dipole emitter was placed in the center of the proposed structure. Several other positions next to the center were also checked. While this changes the overall emission level depending on the local environment of the dipole, the relative suppression inside the bandgap itself is hardly influenced. In 2D, by orienting the dipole in the direction normal to the slab, TM modes are excited, while an orientation parallel to the slab leads to TE excitation. Accordingly, the vertical boundaries of the simulation volume must be terminated by perfect electric or magnetic conductors for TM or TE, respectively. The lateral directions are terminated by open boundaries acting as perfect absorbers. For 3D simulations, all boundaries of the simulation volume are terminated by open boundaries so a change in the dipole orientation merely leads to a concentration of the fields on different parts of the structure. To probe the LDOS and therefore the dipole emission we evaluate the real part of the dipole's radiation impedance, Z. The results are then normalized to the radiation impedance Z_0 of the same dipole placed inside a homogeneous medium of the mean refractive index of the structure. Since the emitted power of the dipole is proportional to its radiation impedance, the relative radiation impedance equals the relative emitted power, $P/P_0 = Z/Z_0$ [126–128]. A suppression of the LDOS and the power emission is expected for frequencies inside the PBG. It is also expected that the emission of the dipole at these frequencies is decreasing exponentially with the lateral side length L of the simulation volume [119, 129, 130]. As the results are scale-independent we present the side lengths normalized to the grating period, L/a.

4.5 Results and discussion

4.5.1 2D structures

The normalized TM power emission spectrum of the dipole for four different structure sizes with 16 gratings and a small refractive-index contrast of $n_1/n_2 = 1.58/1.42 \approx 1.11$

is shown in Fig. 20. An emission suppression band is seen in the spectra at a normalized frequency of about 0.493. The maximum suppression shows the expected exponential decay with increasing side length of the square-shaped simulated structure (inset in Fig. 20).

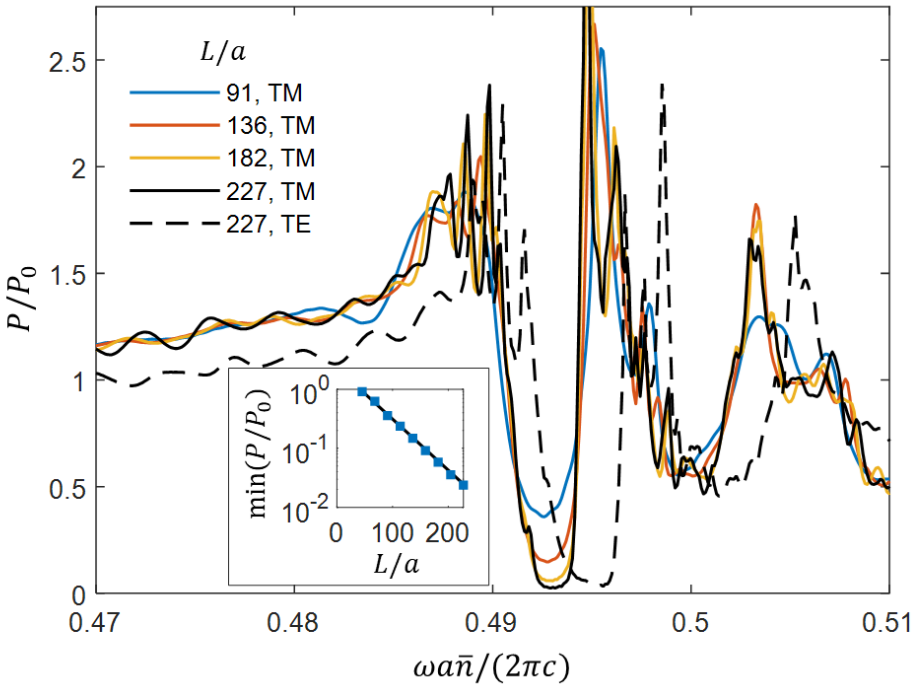


Fig. 20. Normalized power emission of a dipole placed inside a square-shaped 2D quasiperiodic structure. The power emission of the dipole placed inside the structured medium, P, is normalized to the emission in a homogeneous medium with the average refractive index of the structured material, P_0. The L/a-values specifying the side length of the structure are rounded to integer values. The solid lines represent emission for TM excitation; the dashed line represents TE excitation. The structure has a refractive-index contrast $n_1/n_2 = 1.58/1.42 \approx 1.11$ and $N = 16$ underlying gratings. Inset: Semi-logarithmic plot of the minima of the normalized TM power emission over the edge length. The black line is an exponential fit showing as a straight line in the semi-logarithmic plot.

Additionally, for a CPBG the suppression experienced by different polarizations should coincide spectrally. Although a slight spectral shift between the TM and TE positions of the emission gap is observed there is a clear overlap region corresponding to a polarization-independent CPBG. The overlap should further improve for smaller refractive-index contrasts as the polarization shift (Eq. (119)) converges more rapidly than the individual bandgap openings for each polarization (Eq. (109)). In combination, these results unambiguously confirm the opening of a CPBG.

To further validate our model the predicted bandgap widths shall be compared to the numerical results. In Fig. 21 we compare the PBG width predicted by the analytical model

(Eq. (109)) to values obtained by simulation. We simulated grating numbers N between 5 and 25. For some of the grating numbers the values for different structure realizations are shown. For a given N, these differ only in the seed of the random number generator defining the phases of the gratings.

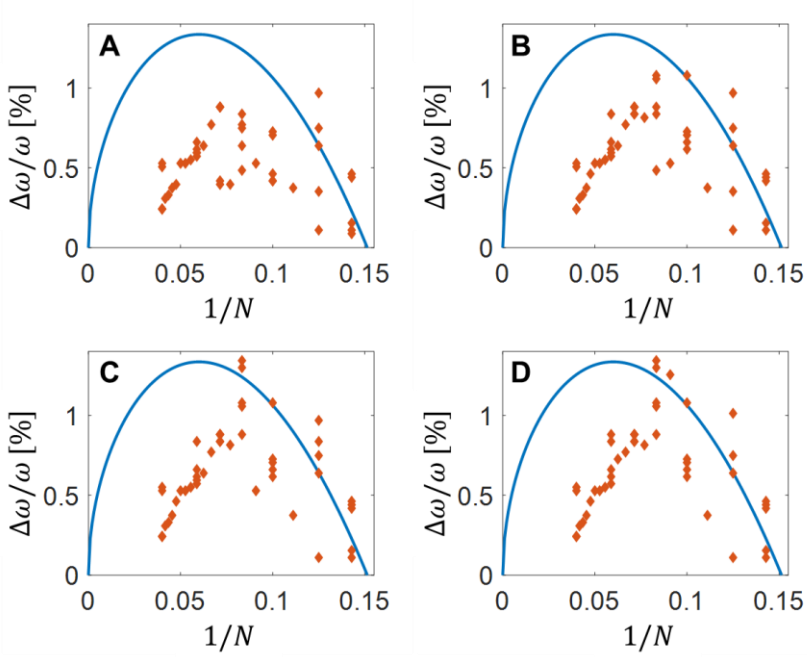


Fig. 21. Comparison of the relative omnidirectional bandgap width in theory and simulation. The blue curves represent the bandwidth expected from our theory while the bandwidths found in simulation are shown as the red diamonds. The simulation values were obtained using the 2D TM case. The refractive-index contrast is $n_1/n_2 = 1.58/1.42$. In the simulations, a lateral structure size of approximately 227 periods was used. The different graphs were found for peak prominence limits of 0.05 (A), 0.1 (B), 0.15 (C) and 0.2 (D).

Since the emission spectra sometimes show spurious peaks inside the bandgap, we had to make decisions on which parts of the spectra belong to the bandgap and which do not. We used the following algorithm to determine the bandwidths: First, the global minimum of the curve is found. From this point, the algorithm looks for the maxima which are closest to the minimum. Maxima that do not exceed a certain peak prominence (see definition below) are neglected. The width of the bandgap is then defined as the distance between the frequencies where the emission reaches half of the power of the lower maximum. The peak prominence is the height of the peak with respect to the higher of the two neighboring minima. A MATLAB algorithm was used to find it, the detailed documentation can be found in reference [131]. Bandgap widths for different choices of minimum peak prominence have been derived from the simulated spectra (Fig. 21). They only lead to minor changes in the detected bandwidths while the trend of the points stays similar.

Overall, the trend seen in the simulation results matches the behavior predicted by our theory. However, for most of the simulated realizations the bandgap is narrower than the theoretically predicted width. Especially for large numbers of gratings (small values of $1/N$), the omnidirectional PBG seems to disappear much faster than predicted, which also shifts the optimum bandgap opening to smaller grating numbers in simulation. A potential explanation for this behavior could be that for these grating numbers grating interactions beyond the next neighbors cannot be neglected. Nevertheless, an omnidirectional PBG opening in the range of 0.5% is observed for grating numbers in the range of 10 to 20.

4.5.2 3D structures

The gratings for the 3D structures need to be arranged such that the Bragg peaks are homogeneously distributed on the spherical surface with radius $b = 2\pi/a$ and the maximum distance from any point on the sphere to the closest Bragg peak is minimized. This task is a special type of a sphere covering problem where no exact solution exists for an arbitrary number of points [125]. There are, however, solutions available in table form that are putatively optimal [132]. Since each grating produces two Bragg peaks on opposite sides of the sphere, a point symmetric distribution is necessary. The arrangements used for this work were the icosahedral solutions to the covering problem calculated in reference [132]. For the results shown here the distributions of 92 and 162 points were used, corresponding to 46 and 81 gratings, respectively. The former value corresponds to the optimum for the used refractive-index values as calculated by Eq. (113). The latter is used for a structure with a lower refractive index contrast. The number is slightly adjusted to a lower grating number than the predicted optimum in accordance with the deviations seen between the 2D theoretical model and the simulation results.

The simulation of low-contrast 3D structures requires large simulation volumes, quickly leading to unbearable computing efforts. We therefore had to limit our considerations to structures with relatively large refractive-index contrasts of $n_1/n_2 = 1.6/1$ and $1.38/1$ with a maximum cube side length of 100 periods. The simulation yields a clear gap in the emission spectrum of the dipole (see Fig. 22). We did not observe an exponential decay of the emitted power over the side length L, though. Instead, based on extrapolation of the structure size, the emission suppression in both cases saturates at approximately -10 dB relative to the low-frequency level. The normalized power emission P/P_0 at low frequency is different for the two structures due to different local dipole positions and

orientations. These local properties do, however, not change the relative suppression scaling with the size of the structure.

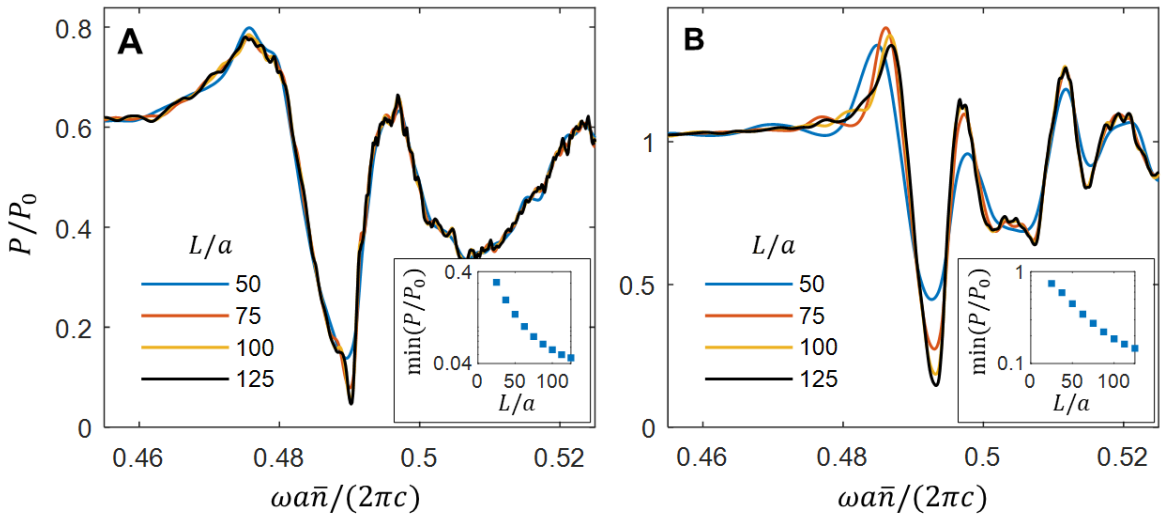


Fig. 22. Normalized emitted power spectrum of a dipole placed inside a 3D quasiperiodic structure. The structure is based on an icosahedral distribution of the underlying gratings. For the simulation in A, a refractive-index contrast of $n_1/n_2 = 1.6/1$ and a grating number of $N = 46$ were used. For the simulation in B, the contrast was 1.38/1 and the grating number 81. The spectra are normalized to the dipole emission in a homogeneous medium with the mean refractive index, $\bar{n} = 1.3$ in A and 1.19 in B. Insets: Semi-logarithmic plot of the minima of the normalized power emission over the edge length.

The theory predicts a CPBG, and thus unlimited LDOS suppression, which is not seen in 3D simulations. Apparently, in the presented 3D structure some channels are still present where energy propagates without evanescent decay. To investigate this further we looked at the far-field emission patterns of a structure with the same underlying grating distribution as the one used in simulations at a contrast of 1.6. However, this time we used a spherical excerpt of the structure to obtain a homogeneous far-field pattern. The structure had a diameter of 80 lattice constants and a contrast of 1.58. In Fig. 23 the results in the bandgap as well as approximately 0.8% above and below the expected CPBG are displayed. For the frequency below the expected CPBG a partial correlation of the emission directions and the Bragg peaks can be seen. Power is primarily emitted into K-directions between gratings. However, some emission at other directions is also observed, which is not explained by our theory. Inside the bandgap a similar behavior is still seen, but the overall power emission is significantly weakened, as is expected from the emission spectra. The emitted power can be partly explained by evanescent modes that tunnel to the boundary of the simulated volume. But some bright spots are also observed in directions not explained by the theory. At the frequency above the bandgap,

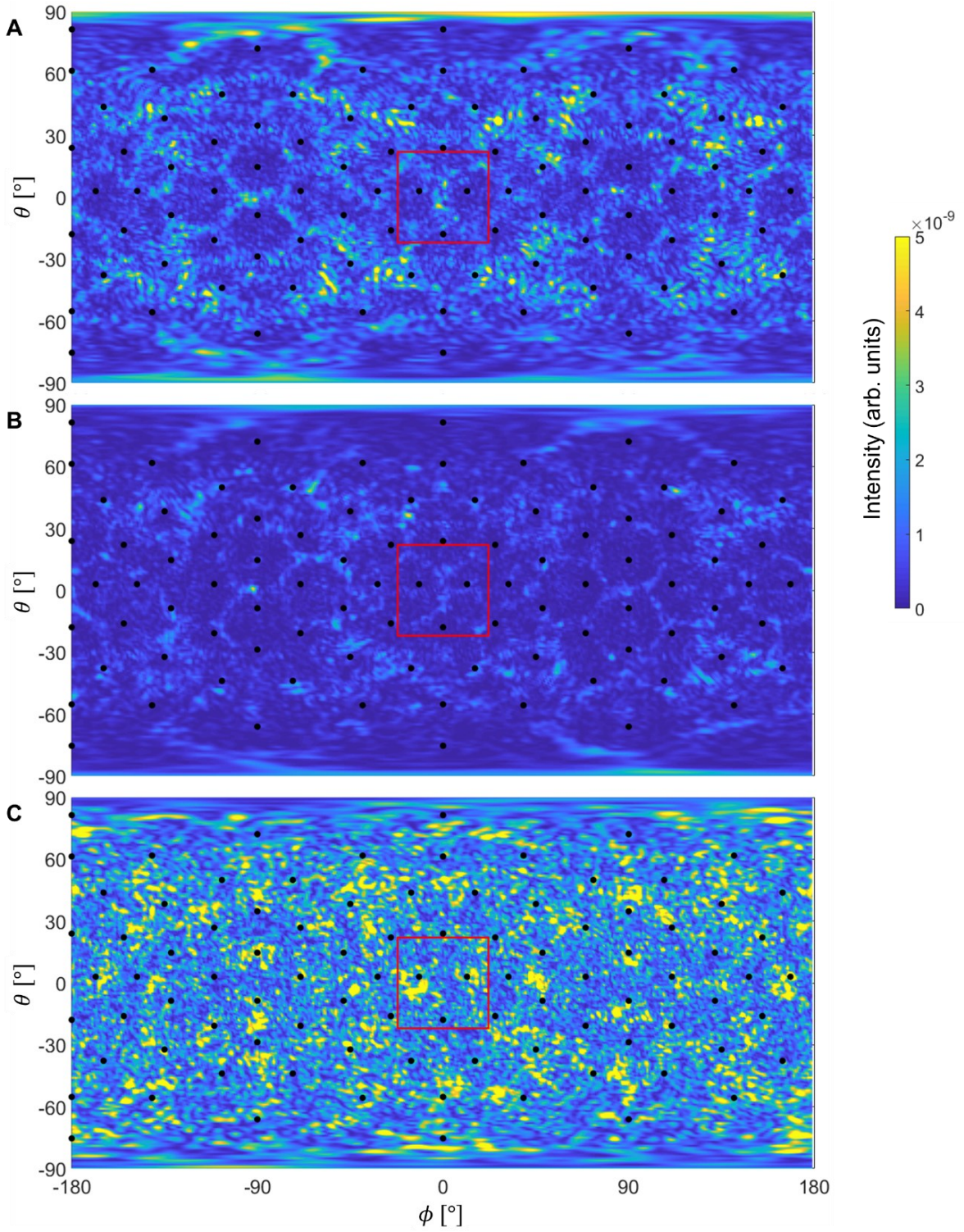


Fig. 23. Far-field simulation results from a spherical 3D structure. The structure had a diameter of 80 lattice constants and a refractive-index contrast of 1.58/1. The color represents angle-dependent power per solid angle in arbitrary units. The displayed results were obtained at a frequency 0.8% below the expected bandgap frequency (A), at the bandgap frequency (B), and 0.8% above the bandgap frequency (C). The directions of the Bragg gratings underlying the structure are shown as black spots. The red squares mark the angle range measured experimentally in transmission.

it is expected that power is primarily emitted into the grating directions. While this can be seen for some of the directions, the overall result is not conclusive for this case.

These deviations could be due to several reasons. First, the chosen refractive-index contrast might still be too large for the analytical approximation to be fully applicable. Second, the interaction between gratings beyond neighbors might not be negligible. A higher-order theory is required to take these effects into account. Third, it might also be that polarization effects are the limiting factor. According to the estimation the polarization effects can close the PBG as the bandgap opening and the polarization splitting both scale with the square of the refractive-index contrast in 3D structures (Eq. (114) and (119)). The effect of polarization could be further studied by simulations using the scalar wave approximation and therefore eliminating the influence of polarization effects in the proposed structures.

4.6 Experimental realization

The 3D structures were also realized and measured experimentally in the microwave range. This part of the project was done in cooperation with the Department of Physics and Engineering of the ITMO University, St. Petersburg, before 2022. While we provided the theoretical background and most of the experiment planning, they performed all experimental tasks – the 3D printing of the structure, the construction of the measurement setup, as well as all microwave measurements. They also performed transmission simulations and provided preliminary evaluations of the data. We then provided feedback on preliminary results and did the final analysis and visualization of the data.

The sample was created by means of an additive 3D printing method. A commercial 3D printer Raise3D Pro 2 Plus was used with the original Raise3D Premium printing filament of polylactide (PLA) plastic with a nozzle diameter of 0.2 mm. The sample voxel model was cut into six slabs along the z-direction prior to printing to make the procedure easier and to reduce the cost in case of a process failure. Each slab was then printed layer-by-layer from bottom to top with an individual layer height of 0.25 mm. No auxiliary structures were used, and each slab was printed directly in its final form. The printing of all six slabs took about 15 days of continuous 3D printer operation. After the printing process, all slabs were stacked together in the correct order to form the whole sample. The final 3D-printed structure has a size of $13.75 \times 13.75 \times 6.875$ cm^3 with a period of $a = 2.825$ mm. That corresponds to a slab with approximately $50 \times 50 \times 25$ periods. The underlying grating distribution is exactly the same one as was used in the simulation with contrast 1.6. A photograph of the printed structure is shown in Fig. 24.

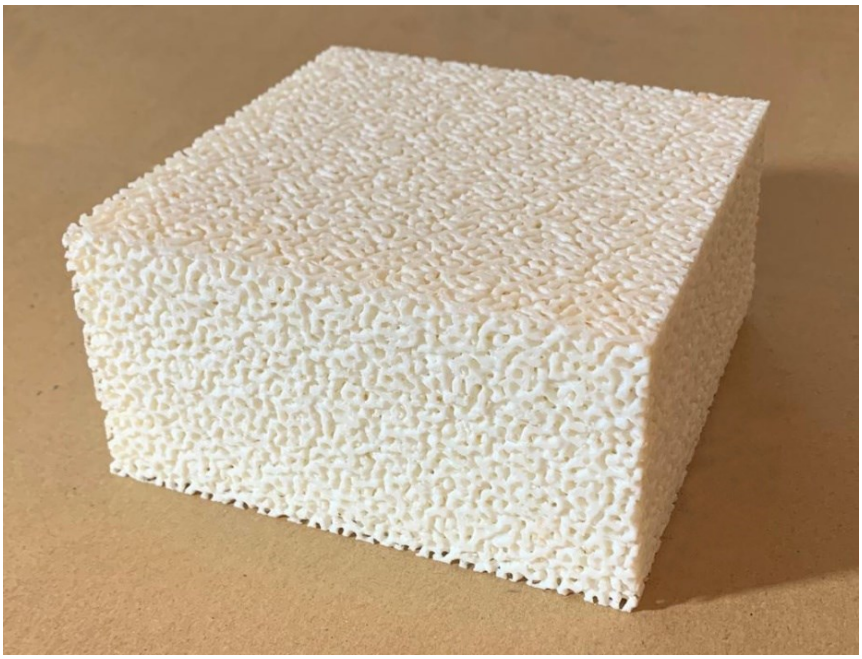


Fig. 24. Photograph of the 3D-printed structure. The structure has a quadratic footprint with 13.75 cm edge lengths and a height of 6.875 cm. The period of the underlying gratings is $a = 2.825$ mm.

PLA has low losses ($\tan(\delta) \approx 10^{-2}$) and a permittivity of about 2.54 ($n \approx 1.59$) in the microwave range [133]. With the filling fraction of 50% the mean refractive index of the structure is therefore $\bar{n} \approx 1.3$. With the given dimensions this roughly corresponds to an expected bandgap position of $c/(2a\bar{n}) \approx 40.8$ GHz, or a vacuum wavelength of about 7.3 mm.

As in previous publications [9, 101, 121], transmission instead of emission was measured. Emission measurements require an antenna to be placed inside the structure and a corresponding feed line. This is difficult to achieve without creating additional channels for emission. In order to measure the transmission coefficient through the sample a setup consisting of two wideband ridged horn antennas DRH50 by RFSpin with an operational band of 4–50 GHz (corresponding to vacuum wavelengths between 6 and 75 mm) was used. The antennas were controlled using a Keysight PNA-X N5247B vector network analyzer (VNA). A schematic of the setup as well as a photograph of the setup inside the anechoic chamber where the measurements were carried out are presented in Fig. 25.

The θ-angle for both antennas was set manually, and the sample was rotated around the vertical axis by means of a stepper motor, which is equivalent to changing the ϕ-angle of the antennas. The rotations did not change the distance between the antennas, which was always 20.75 cm. The angles θ and ϕ were varied with step widths of 1° and 0.5°,

respectively. For each pair of θ, ϕ within $\pm 30°$ around the structure normal[11] the S-parameter S21 was measured in a frequency range of 30–50 GHz. All the measured transmission spectra were then normalized to the transmission spectrum of the antenna pair without the sample.

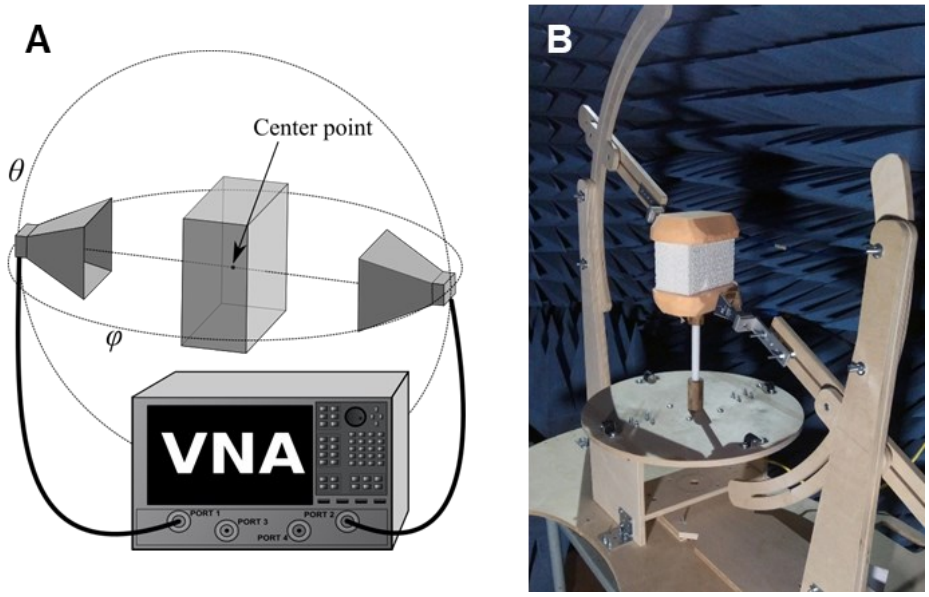


Fig. 25. Scheme (A) and photograph (B) of the experimental setup for transmission measurement. Both antennas are simultaneously rotated around the center point of the sample such that they always face each other. The S-parameters are measured by means of a vector network analyzer (VNA). As seen in the photo, the antennas are rotated in θ-direction. Rotation in ϕ-direction is realized by rotation of the sample mount around its vertical axis, which is equivalent to the simultaneous rotation of both antennas in φ-direction.

Fig. 26 shows an average transmission spectrum, where for each frequency point the transmission was averaged over the full angular range. By this, we get a representative average over different crystallographic directions. The graph shows a clear edge at approximately 38 GHz, which is close to the expected bandgap position. The transmission does not have a peak close to the transmission gap and does not recover at higher frequencies, which is an expected difference to the emission spectra. Emission is sensitive to the density of states in the structured material. It increases at the band edges due to slow light propagation and decreases in the bandgaps. Transmission is low in the bandgap, too, but in contrast to emission it is also low when the group velocity is small or when light is deflected by the structure. Thus, there are no peaks at the band edges. On

[11] The $\pm 30°$ outside the structure correspond to angles of $\approx \pm 22°$ inside the structure when corrected for refraction.

the high-frequency side of the bandgap there is reflection due to higher-order bandgaps and reflection and deflection due to group velocity effects.

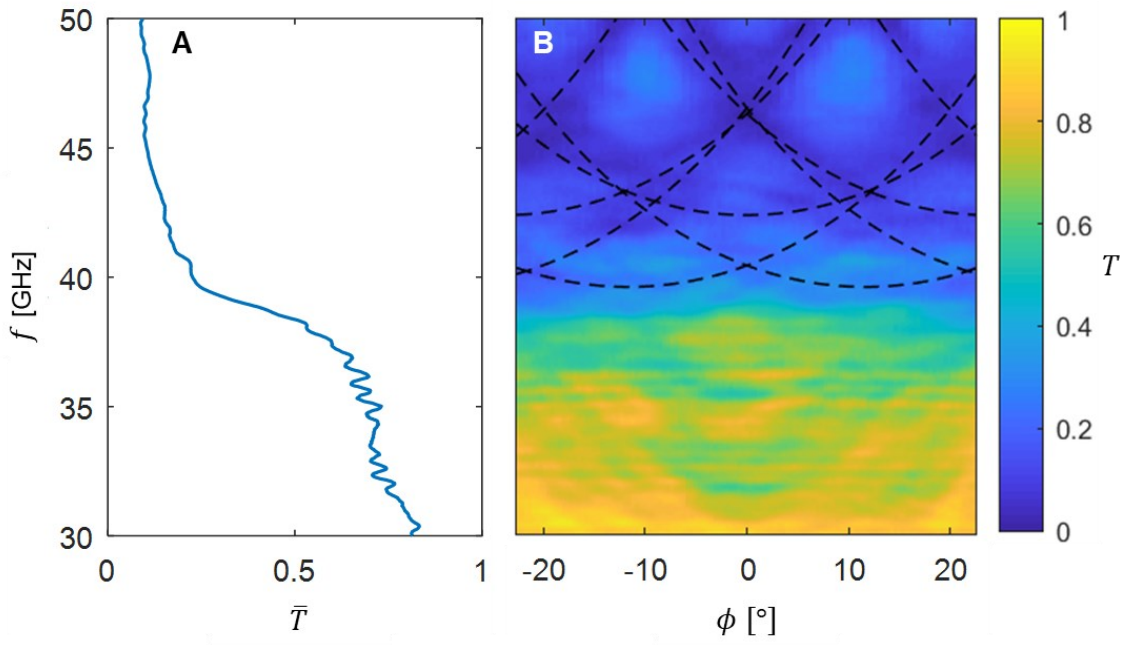


Fig. 26. Measured transmission spectrum of the 3D-printed structure. A: Transmission of the structure averaged over the full measured angular range of $\pm 30°$ in azimuth and elevation. A transmission suppression of about -6 dB is seen at the transition around 40 GHz. B: Measured transmission at $\theta = 0$ over frequency and ϕ. The ϕ-values inside the structure are shown, corrected for refraction at the interface. The dashed black lines represent the Bragg condition of neighboring gratings for an assumed mean refractive index of $\bar{n} = 1.34$.

Since the emission simulations and the transmission experiments are somewhat difficult to directly compare, we also aimed to substantiate the experimental results further by transmission simulations. For this, two horn antennas were placed diametrically facing each other. The transmission was simulated with the structure and normalized to the transmission without the structure. The structure was set up to exactly mimic the structural and material parameters of the experimental realization. The resulting transmission spectrum for normal incidence is shown in Fig. 27. For comparison, the experimentally measured data for normal incidence is plotted. The spectra are overall very similar.

The relative suppression at the bandgap frequency in emission simulations and transmission measurements is found by comparison to the corresponding values at lower frequencies. From Fig. 26A a transmission suppression of about -6 dB is seen at 41 GHz compared to the transmission at 30 GHz. In emission simulations we expect a comparable

suppression by taking a volume with a distance between the dipole and the boundary of the simulation volume which equals the slab thickness in the transmission measurement. This is the case for the structure with $L/a = 50$ in Fig. 22A. A comparable suppression of about -6 dB in the minimum is observed relative to the emission level at a normalized frequency of 0.46. We conclude that the quasiperiodic structure constitutes an almost angle-independent low-pass filter for microwave radiation.

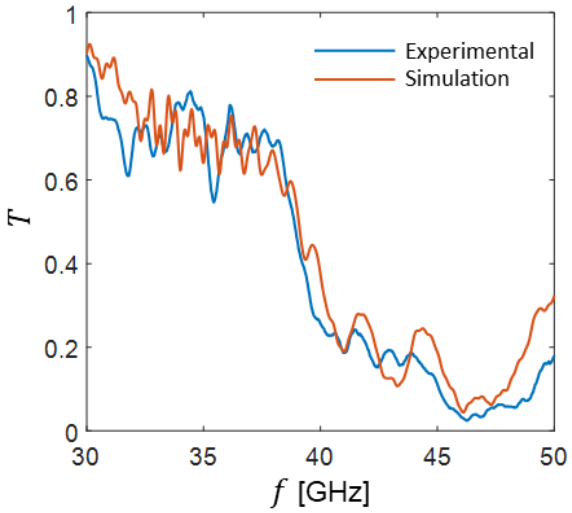


Fig. 27. Comparison of the transmission spectra seen in experiment and simulation. In both cases, a pair of antennas was positioned normal to the slab surface ($\phi = \theta = 0$). The simulation data was obtained with a structure in between the antennas that equals the experimentally realized structure in geometry and material parameters. As in the experimental result, the simulation spectrum is normalized to the case with no structure between the antennas.

The residual angle dependence in the stop band can be traced back to the neighboring Bragg peaks. The dashed black lines in Fig. 26B represent the Bragg condition of the several Bragg peaks close to normal direction. They fit the measured data very well for an assumed mean refractive index of 1.34. This is slightly above the expected value of 1.3. We assign this deviation to a slightly higher solid filling fraction of the structure caused by the model preparation during the 3D printing procedure.

The angle-resolved measurement also confirms the effective Bragg gratings underlying the seemingly disordered structure. When measuring the transmission at frequencies slightly below and above the expected CPBG range, light should only be transmitted in certain identifiable directions. At frequencies slightly below the CPBG (below ω_{low}, see Fig. 17B), transmission in the Bragg grating directions (corresponding to the *M*-directions, see Fig. 17A) is already blocked, while light can still propagate in the directions in between the Bragg peaks (*K*-directions). At frequencies slightly above the

CPBG (above ω_{up}) this behavior is inverted: In between the Bragg peaks, transmission should now be blocked, while in the grating directions no bandgap is available. This behavior is well visible in measurements at 39 and 40.5 GHz, respectively. The measurement data in comparison to the Bragg peak positions is shown in Fig. 28A and D. For frequencies inside the bandgap the transition between these two cases can be seen (Fig. 28B and C). The results also compare well to the far-field emission simulations shown in Fig. 23, where the angle range covered by the experiments is shown by the red squares.

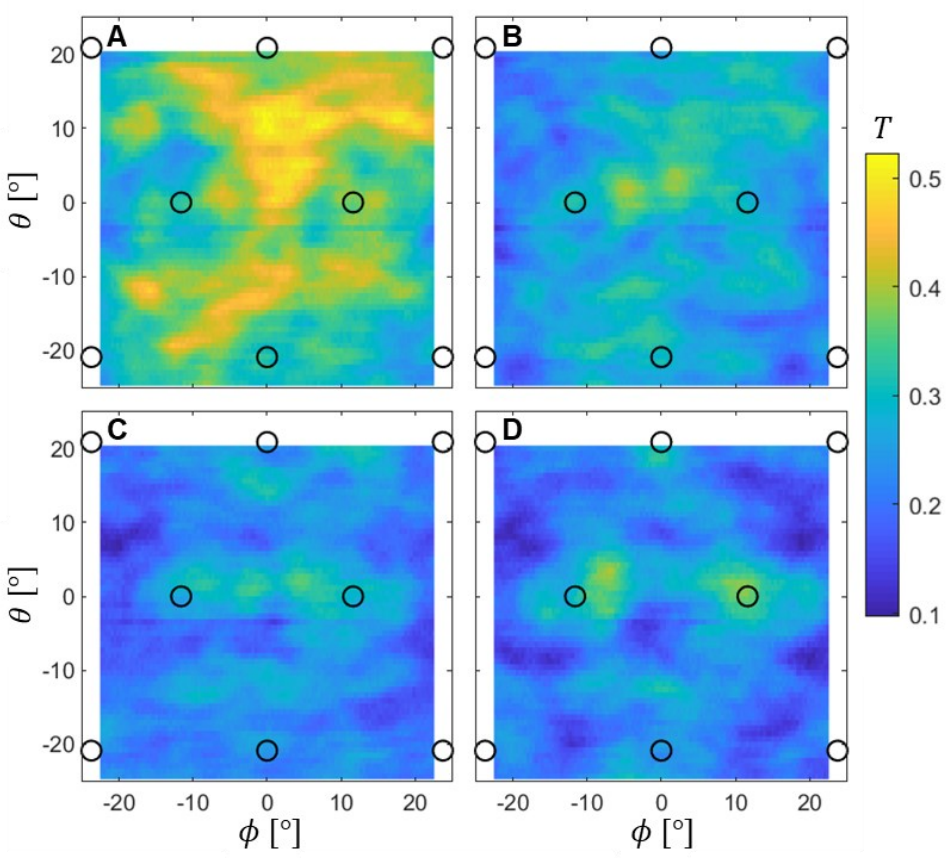


Fig. 28. Angle mapping of the measured transmission at wavelengths around the bandgap. The transmission at frequencies 39 (A), 39.5 (B), 40 (C), and 40.5 GHz (D) is shown, which is slightly below (A), inside (B and C), and above (D) the expected CPBG frequency range, respectively. The black circles show the expected Bragg peaks of the gratings underlying the measured structure. Angles inside the structure are shown, corrected for refraction at the interface.

4.7 Chapter conclusions

We have proposed a distributed quasiperiodic structure with an efficient utilization of the refractive-index contrast to block emission in all directions. An analytical model is

presented which predicts optimum conditions for the maximum bandgap opening for both the 2D and the 3D case. At these optimum conditions a bandgap opening for an arbitrarily small refractive-index contrast is expected. We show numerically that it is possible to obtain a 2D CPBG with a refractive-index contrast as low as 1.11. This is the smallest refractive-index contrast producing a CPBG that was demonstrated so far. The numerical confirmation for even smaller refractive-index contrasts requires even larger simulation volumes but should be equally possible. The 2D structures shown in this work can readily be manufactured, e.g., by e-beam lithography or direct laser writing, which paves the way to all kinds of photonic bandgap applications in slabs of materials with low refractive-index contrasts. Even a typical refractive-index contrast in the order of 1.1 between the ordinary and extraordinary polarization of a typical liquid crystal [134] would be sufficient.

In the 3D case we could not confirm the existence of a CPBG. Nevertheless, we demonstrate almost -10 dB suppression of emission at a contrast of 1.38 that could be realized with polymers. This by far exceeds the suppression shown in previous works investigating 3D structures at similar contrasts [12, 135]. We also realized the 3D structures by additive manufacturing with standard 3D-printing techniques and conducted transmission measurements in the microwave range. Thereby, we were able to confirm strong and nearly direction-independent transmission suppression over a wide angular range at the expected bandgap position and verify the quasiperiodic nature of the investigated structures.

5 Conclusions and outlook

5.1 Structural colors

Our work on structural colors added to the knowledge base regarding the understanding, design, and optimization of the underlying structures. However, there are several open questions and uncertainties left that will be discussed in the following paragraphs. Also, since the publication of our work, other groups have continued the work on the topic, leading to new, sometimes surprising results that we will briefly comment on here.

We show that the Ewald sphere can be a useful model to understand the scattering in low-contrast structures, even though for higher-contrast structures other approaches might be better suited. Another important message is the potentially beneficial effect of total internal reflection on the color saturation.

Further research might be needed regarding the second, lower-wavelength scattering peak in the reflection spectrum of structural colors. While Noh et al. found the cause of this peak to be doubly scattered light [67], and our study seems to confirm this conjecture, a new study by Hwang et al. seems to contradict our findings [136]. In their case, the secondary peak is explained by light totally internally reflected at the sample interface, which they claim has a high probability to be scattered again. This contradicts our conclusion that the total internal reflection leads to a drop in reflectivity. More research will be needed to investigate this disagreement.

Another point discussed in the same paper [136] is the thickness dependence of structural colors. In very thick films, multiple scattering predominates at all wavelengths, leading to a white appearance of the color film. When the film is very thin, scattering will generally be weak, and the sample will appear transparent. In between these two extrema there should be an optimum leading to maximum color saturation. For photonic glass, the paper provides a rough estimate, stating that the film thickness should be two to three times the transport mean free path. For the structures we used, it is more difficult to determine the scattering mean free path (and therefore the transport mean free path). Its calculation is typically based on the scattering cross sections of particles making up the structure, which is not compatible with our model. If the scattering mean free path of our structures was to be found, the model from the Hwang paper could directly be used to estimate the optimum thickness.

A second publication from the same group investigates a Monte Carlo algorithm for the optimization of structural color [137], as we also proposed in our paper on structural colors. However, instead of the first-order approximation the authors use the Mie theory to predict the probability of different scattering directions. This approach is suitable for a sample made from spherical particles, but it is limited to these and therefore less general than our approach. They also include a model for surface roughness based on a fit of simulated spectra to experimentally obtained ones. Furthermore, their model keeps track of the phase at least within single trajectories, and therefore at least partially considers interference effects.

The model is validated against experimental data and shown to work well at least in the weak multiple scattering regime. The authors use the model to investigate a wide range of parameters, including sample thickness, absorption strength, particle size, and packing density. Based on this, they realize an optimized gamut containing saturated blue and green colors, but still nearly entirely lacking yellows and reds. Nevertheless, their model provides a useful tool to approximately realize a target color from any given material. It might thereby mark another step in the direction of industrially usable structural colors.

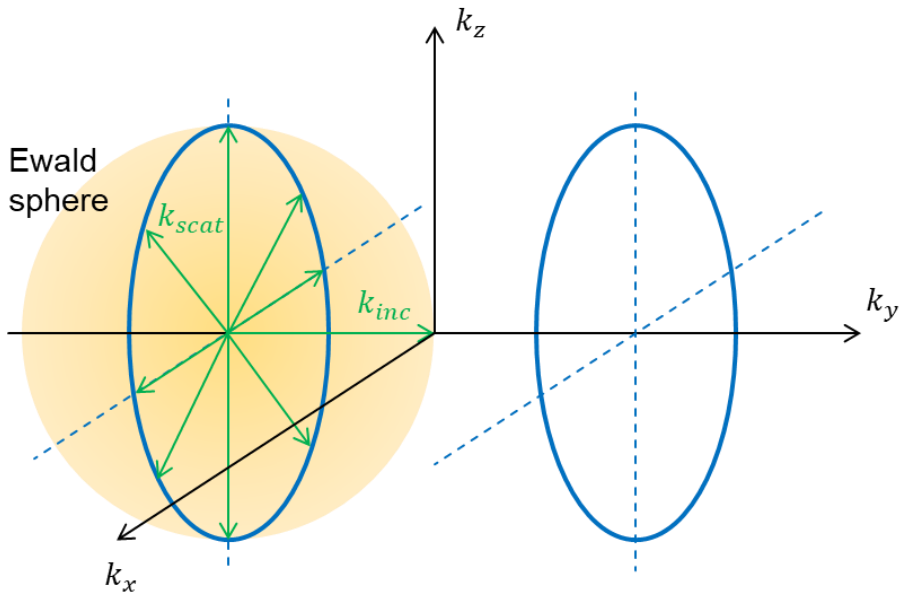


Fig. 29. Reciprocal design for narrow-band light trapping. Light incident in *y*-direction gets scattered orthogonally. In a film geometry, the scattered light would propagate parallel to the film, effectively trapping it inside.

Work on the topic also continues in our group. Based on the Ewald sphere approach and our structure generation approach based on the superposition of gratings, other structures can readily be conjectured that scatter light in a very controlled manner. E.g., structures are now designed with two spherical “belts” in reciprocal space (Fig. 29). For

normally incident light, the Ewald sphere will overlap the corresponding belt in a very narrow wavelength range, while little to no light is scattered at other wavelengths. The belt width can then be designed such that all scattered light falls into the angle range subject to total internal reflection. By this, light of the designed wavelength has a high chance to be trapped inside the film, where it can, e.g., be used for charge separation in photovoltaic applications.

5.2 Complete photonic bandgaps

By providing an approach to fully control light transport in arbitrary-index materials, we believe our results can end a decade-long search for the minimum allowable refractive index – at least for 2D, there is none. However, plenty of research opportunities remain open.

First and foremost, while we do show a functioning approach for 2D structures and a significant effect in 3D, no actual bandgap was found in the latter. And while we do discuss potential reasons for this, the exact problem with 3D structures, and especially the question how to overcome it, remain open.

Another drawback of our approach is that the structures become increasingly bulky as the refractive-index contrast is reduced. The large size of the structures is necessary as the light spreads out in a significant area (or volume in 3D). However, some of the applications of bandgap materials, e.g., in the field of sensing, rely explicitly on light to be strongly spatially confined. For such applications high-index materials remain the superior choice.

We focused our attention on truly quasiperiodic structures. For the 3D case, we showed simulations of structures with sizes of 125 periods and up to 126 Bragg peaks. Looking back at the Bragg peak numbers shown in Fig. 4C (page 24), it can be seen that this number of peaks can be reproduced in periodic structures already at $L/a < 10$. A rigorous search for peak distributions that are as homogeneous as possible, potentially allowing some small tolerance for the grating periods, may yield interesting periodic structures with unit cells small enough for full band simulations. By this method, complete bandgaps could be clearly identified, making this another very interesting direction for further investigation.

As a final point, the emission spectra of the dipoles placed inside the bandgap structures show another striking feature: Next to the bandgap, the emission is much stronger than in the reference case. The peaks can be clearly seen in Fig. 20 (page 68), where they reach significant levels, showing an emission enhancement by a factor of more than two. The

reason for the occurrence of these peaks lies in the extremely low slope of the bands at the band edges. This leads to a significant increase in the density of states and is also observed in simple geometries like a Bragg mirror. Since the band structure of our structures can directly be influenced by the number of gratings used, they seem to be an ideal candidate to further optimize the emission enhancement. Whether they can outperform known structures in this respect remains to be seen.

6 References

1. J. D. Joannopoulos, S. G. Johnson, J. N. Winn, and R. D. Meade, *Photonic crystals: Molding the flow of light* (Princeton University Press, ed. 2, 2008).
2. D. S. Wiersma, Disordered photonics. *Nat. Photonics* **7**, 188–196 (2013).
3. A. P. Gibson, J. C. Hebden, and S. R. Arridge, Recent advances in diffuse optical imaging. *Phys. Med. Biol.* **50**, R1-43 (2005).
4. H. Cao, Y. G. Zhao, S. T. Ho, E. W. Seelig, Q. H. Wang, and R. P. H. Chang, Random laser action in semiconductor powder. *Phys. Rev. Lett.* **82**, 2278–2281 (1999).
5. D. S. Wiersma, The physics and applications of random lasers. *Nature Phys* **4**, 359–367 (2008).
6. V. E. Ferry, M. A. Verschuuren, M. C. van Lare, R. E. I. Schropp, H. A. Atwater, and A. Polman, Optimized spatial correlations for broadband light trapping nanopatterns in high efficiency ultrathin film a-Si:H solar cells. *Nano Lett.* **11**, 4239–4245 (2011).
7. C. Rockstuhl, S. Fahr, K. Bittkau, T. Beckers, R. Carius, F.-J. Haug, T. Söderström, C. Ballif, and F. Lederer, Comparison and optimization of randomly textured surfaces in thin-film solar cells. *Opt. Express* **18**, A335-A342 (2010).
8. K. Vynck, M. Burresi, F. Riboli, and D. S. Wiersma, Photon management in two-dimensional disordered media. *Nat. Mater.* **11**, 1017–1022 (2012).
9. W. Man, M. Megens, P. J. Steinhardt, and P. M. Chaikin, Experimental measurement of the photonic properties of icosahedral quasicrystals. *Nature* **436**, 993–996 (2005).
10. K. Edagawa, S. Kanoko, and M. Notomi, Photonic amorphous diamond structure with a 3D photonic band gap. *Phys. Rev. Lett.* **100**, 13901 (2008).
11. G. Buxbaum and G. Praff (Eds.), *Industrial Inorganic Pigments* (WILEY-VCH Verlag, ed. 3, 2005).
12. H. Yin, B. Dong, X. Liu, T. Zhan, L. Shi, J. Zi, and E. Yablonovitch, Amorphous diamond-structured photonic crystal in the feather barbs of the scarlet macaw. *Proc. Natl. Acad. Sci. U.S.A.* **109**, 10798–10801 (2012).

13. J. C. Maxwell, A dynamical theory of the electromagnetic field. *Philos. Trans. Royal Soc.* **155**, 459–512 (1865).

14. C. Castelnovo, R. Moessner, and S. L. Sondhi, Magnetic monopoles in spin ice. *Nature* **451**, 42–45 (2008).

15. M. Born and E. Wolf, *Principles of optics: Electromagnetic theory of propagation, interference and diffraction of light* (Cambridge University Press, ed. 7, 1999).

16. J. J. Sakurai and J. Napolitano, *Modern quantum mechanics* (Cambridge University Press, ed. 2, 2017).

17. S. G. Johnson, M. Ibanescu, M. A. Skorobogatiy, O. Weisberg, J. D. Joannopoulos, and Y. Fink, Perturbation theory for Maxwell's equations with shifting material boundaries. *Phys. Rev. E* **65**, 66611 (2002).

18. B. E. A. Saleh and M. C. Teich, *Fundamentals of photonics* (John Wiley & Sons, Inc., 1991).

19. P. Sheng, *Introduction to wave scattering, localization and mesoscopic phenomena* (Springer, ed. 2, 2006).

20. A. Sihvola, *Electromagnetic mixing formulas and applications* (The Institution of Engineering and Technology, ed. 2, 2008).

21. H. C. van de Hulst, *Light scattering by small particles* (Dover Publications, Inc., 1981).

22. P. D. García, R. Sapienza, and C. López, Photonic glasses: a step beyond white paint. *Adv. Mater.* **22**, 12–19 (2010).

23. S. T. Flock, M. S. Patterson, B. C. Wilson, and D. R. Wyman, Monte Carlo modeling of light propagation in highly scattering tissue - I: Model predictions and comparison with diffusion theory. *IEEE Trans. Biomed. Eng.* **36**, 1162–1168 (1989).

24. E. Yablonovitch, Inhibited spontaneous emission in solid-state physics and electronics. *Phys. Rev. Lett.* **58**, 2059–2062 (1987).

25. C. Kittel, *Introduction to solid state physics* (John Wiley & Sons, Inc., ed. 8, 2005).

26. W. Setyawan and S. Curtarolo, High-throughput electronic band structure calculations: Challenges and tools. *Comput. Mater. Sci.* **49**, 299–312 (2010).

27. J. Bamberg, G. Cairns, and D. Kilminster, The crystallographic restriction, permutations, and Goldbach's conjecture. *Am. Math. Mon.* **110**, 202 (2003).

28. Press release of the Royal Swedish Academy of Sciences (available at https://www.nobelprize.org/prizes/chemistry/2011/press-release/, last retrieved on March 12, 2023).

29. D. Shechtman, I. Blech, D. Gratias, and J. W. Cahn, Metallic phase with long-range orientational order and no translational symmetry. *Phys. Rev. Lett.* **53**, 1951–1953 (1984).

30. C. Janot, *Quasicrystals: A Primer* (Oxford University Press, ed. 2, 1994).

31. R. Penrose, The role of aesthetics in pure and applied mathematical research. *Bull. Inst. Math. Appl.* **10**, 266 (1974).

32. P. J. Lu and P. J. Steinhardt, Decagonal and quasi-crystalline tilings in medieval Islamic architecture. *Science* **315**, 1106–1110 (2007).

33. L. Dal Negro and S. V. Boriskina, Deterministic aperiodic nanostructures for photonics and plasmonics applications. *Laser Photonics Rev.* **6**, 178–218 (2012).

34. P. Barthelemy, J. Bertolotti, and D. S. Wiersma, A Lévy flight for light. *Nature* **453**, 495–498 (2008).

35. G. Shang, L. Maiwald, H. Renner, D. Jalas, M. Dosta, S. Heinrich, A. Petrov, and M. Eich, Photonic glass for high contrast structural color. *Sci. Rep.* **8**, 7804 (2018).

36. L. Schertel, I. Wimmer, P. Besirske, C. M. Aegerter, G. Maret, S. Polarz, and G. J. Aubry, Tunable high-index photonic glasses. *Phys. Rev. Materials* **3**, 15203 (2019).

37. G. Maret, University of Konstanz, Germany and S. Torquato, Princeton University, USA, personal communication in the framework of the Disomat conference 2019, Potsdam, Germany.

38. R. C. Gauthier and A. Ivanov, Production of quasi-crystal template patterns using a dual beam multiple exposure technique. *Opt. Express* **12**, 990–1003 (2004).

39. N. D. Lai, W. P. Liang, J. H. Lin, C. C. Hsu, and C. H. Lin, Fabrication of two- and three-dimensional periodic structures by multi-exposure of two-beam interference technique. *Opt. Express* **13**, 9605–9611 (2005).

40. P. N. Dyachenko and Y. V. Miklyaev, Band structure calculations of 2D photonic pseudoquasicrystals obtainable by holographic lithography. *Proc. SPIE* **6182**, 61822I (2006).

41. P. L. Hagelstein and D. R. Denison, Nearly isotropic photonic bandgap structures in two dimensions. *Opt. Lett.* **24**, 708–710 (1999).

42. M. C. Rechtsman, H.-C. Jeong, P. M. Chaikin, S. Torquato, and P. J. Steinhardt, Optimized structures for photonic quasicrystals. *Phys. Rev. Lett.* **101**, 73902 (2008).

43. N. F. Berk, Scattering properties of the leveled-wave model of random morphologies. *Phys. Rev. A* **44**, 5069 (1991).

44. L. Maiwald, S. Lang, D. Jalas, H. Renner, A. Y. Petrov, and M. Eich, Ewald sphere construction for structural colors. *Opt. Express* **26**, 11352–11365 (2018).

45. C. Soyarslan, S. Bargmann, M. Pradas, and J. Weissmüller, 3D stochastic bicontinuous microstructures: Generation, topology and elasticity. *Acta Mater.* **149**, 326–340 (2018).

46. More information online (available at https://www.3ds.com/products-services/simulia/products/cst-studio-suite/, last retrieved on March 12, 2023).

47. T. Weiland, A discretization model for the solution of Maxwell's equations for six-component fields. *Arch. Elektron. Uebertrag.* **31**, 116–120 (1977).

48. T. Weiland, Time domain electromagnetic field computation with finite difference methods. *Int. J. Numer. Model.* **9**, 295–319 (1996).

49. K. Yee, Numerical solution of initial boundary value problems involving Maxwell's equations in isotropic media. *IEEE Trans. Antennas Propag.* **14**, 302–307 (1966).

50. S. Lang, L. Maiwald, H. Renner, D. Jalas, A. Y. Petrov, and M. Eich, A quantitative first-order approach for the scattering of light by structured thin films. *arXiv* 1802.07058 (2018).

51. P. Vukusic and J. R. Sambles, Photonic structures in biology. *Nature* **424**, 852–855 (2003).

52. S. Kinoshita and S. Yoshioka, Structural colors in nature: the role of regularity and irregularity in the structure. *ChemPhysChem* **6**, 1442–1459 (2005).

53. S. Kinoshita, S. Yoshioka, and J. Miyazaki, Physics of structural colors. *Rep. Prog. Phys.* **71**, 76401 (2008).

54. M. D. Shawkey, N. I. Morehouse, and P. Vukusic, A protean palette: colour materials and mixing in birds and butterflies. *J. R. Soc. Interface* **6**, S221-S231 (2009).

55. A. E. Seago, P. Brady, J.-P. Vigneron, and T. D. Schultz, Gold bugs and beyond: a review of iridescence and structural colour mechanisms in beetles (Coleoptera). *J. R. Soc. Interface* **6**, S165-S184 (2009).

56. R. O. Prum, T. Quinn, and R. H. Torres, Anatomically diverse butterfly scales all produce structural colours by coherent scattering. *J. Exp. Biol.* **209**, 748–765 (2006).

57. P. Vukusic, B. Hallam, and J. Noyes, Brilliant whiteness in ultrathin beetle scales. *Science* **315**, 348 (2007).

58. V. Saranathan, C. O. Osuji, S. G. J. Mochrie, H. Noh, S. Narayanan, A. Sandy, E. R. Dufresne, and R. O. Prum, Structure, function, and self-assembly of single network gyroid (I4132) photonic crystals in butterfly wing scales. *Proc. Natl. Acad. Sci. U.S.A.* **107**, 11676–11681 (2010).

59. G. E. Schröder-Turk, S. Wickham, H. Averdunk, F. Brink, J. D. Fitz Gerald, L. Poladian, M. C. J. Large, and S. T. Hyde, The chiral structure of porous chitin within the wing-scales of Callophrys rubi. *J. Struct. Biol.* **174**, 290–295 (2011).

60. J. P. Vigneron, J.-F. Colomer, N. Vigneron, and V. Lousse, Natural layer-by-layer photonic structure in the squamae of Hoplia coerulea (Coleoptera). *Phys. Rev. E* **72**, 61904 (2005).

61. B. D. Wilts, K. Michielsen, J. Kuipers, H. de Raedt, and D. G. Stavenga, Brilliant camouflage: photonic crystals in the diamond weevil, Entimus imperialis. *Proc. R. Soc. B* **279**, 2524–2530 (2012).

62. E. Shevtsova, C. Hansson, D. H. Janzen, and J. Kjærandsen, Stable structural color patterns displayed on transparent insect wings. *Proc. Natl. Acad. Sci. U.S.A.* **108**, 668–673 (2011).

63. V. Saranathan, J. D. Forster, H. Noh, S.-F. Liew, S. G. J. Mochrie, H. Cao, E. R. Dufresne, and R. O. Prum, Structure and optical function of amorphous photonic nanostructures from avian feather barbs: a comparative small angle X-ray scattering (SAXS) analysis of 230 bird species. *J. R. Soc. Interface* **9**, 2563–2580 (2012).

64. L. D'Alba, L. Kieffer, and M. D. Shawkey, Relative contributions of pigments and biophotonic nanostructures to natural color production: a case study in budgerigar (Melopsittacus undulatus) feathers. *J. Exp. Biol.* **215**, 1272–1277 (2012).

65. D. G. Stavenga, J. Tinbergen, H. L. Leertouwer, and B. D. Wilts, Kingfisher feathers – colouration by pigments, spongy nanostructures and thin films. *J. Exp. Biol.* **214**, 3960–3967 (2011).

66. H. Noh, S. F. Liew, V. Saranathan, S. G. J. Mochrie, R. O. Prum, E. R. Dufresne, and H. Cao, How noniridescent colors are generated by quasi-ordered structures of bird feathers. *Adv. Mater.* **22**, 2871–2880 (2010).

67. H. Noh, S. F. Liew, V. Saranathan, R. O. Prum, S. G. J. Mochrie, E. R. Dufresne, and H. Cao, Double scattering of light from biophotonic nanostructures with short-range order. *Opt. Express* **18**, 11942–11948 (2010).

68. R. O. Prum, R. H. Torres, S. Williamson, and J. Dyck, Coherent light scattering by blue feather barbs. *Nature* **396**, 28–29 (1998).

69. R. O. Prum, R. Torres, S. Williamson, and J. Dyck, Two-dimensional Fourier analysis of the spongy medullary keratin of structurally coloured feather barbs. *Proc. R. Soc. B* **266**, 13–22 (1999).

70. M. D. Shawkey and G. E. Hill, Significance of a basal melanin layer to production of non-iridescent structural plumage color: evidence from an amelanotic Steller's jay (Cyanocitta stelleri). *J. Exp. Biol.* **209**, 1245–1250 (2006).

71. J. P. Vigneron, J.-F. Colomer, M. Rassart, A. L. Ingram, and V. Lousse, Structural origin of the colored reflections from the black-billed magpie feathers. *Phys. Rev. E* **73**, 21914 (2006).

72. B. D. Wilts, K. Michielsen, H. de Raedt, and D. G. Stavenga, Sparkling feather reflections of a bird-of-paradise explained by finite-difference time-domain modeling. *Proc. Natl. Acad. Sci. U.S.A.* **111**, 4363–4368 (2014).

73. J. Tinbergen, B. D. Wilts, and D. G. Stavenga, Spectral tuning of Amazon parrot feather coloration by psittacofulvin pigments and spongy structures. *J. Exp. Biol.* **216**, 4358–4364 (2013).

74. M. D. Shawkey and G. E. Hill, Carotenoids need structural colours to shine. *Biol. Lett.* **1**, 121–124 (2005).

75. R. O. Prum and R. Torres, Structural colouration of avian skin. *J. Exp. Biol.* **206**, 2409–2429 (2003).

76. R. O. Prum and R. H. Torres, Structural colouration of mammalian skin. *J. Exp. Biol.* **207**, 2157–2172 (2004).

77. L. M. Mäthger, E. J. Denton, N. J. Marshall, and R. T. Hanlon, Mechanisms and behavioural functions of structural coloration in cephalopods. *J. R. Soc. Interface* **6**, S149-S163 (2009).

78. S. Vignolini, P. J. Rudall, A. V. Rowland, A. Reed, E. Moyroud, R. B. Faden, J. J. Baumberg, B. J. Glover, and U. Steiner, Pointillist structural color in Pollia fruit. *Proc. Natl. Acad. Sci. U.S.A.* **109**, 15712–15715 (2012).

79. S. Magkiriadou, J.-G. Park, Y.-S. Kim, and V. N. Manoharan, Absence of red structural color in photonic glasses, bird feathers, and certain beetles. *Phys. Rev. E* **90**, 62302 (2014).

80. M. Jansen and H. P. Letschert, Inorganic yellow-red pigments without toxic metals. *Nature* **404**, 980–982 (2000).

81. Regulation (EC) No 1907/2006 of the European Parliament and of the Council of 18 December 2006, CELEX number: 02006R1907-20220301. (March 01, 2022).

82. European Chemicals Agency, Annex XV report: Assessment whether the use of Cadmium and its compounds in plastic materials not covered by entry 23 of REACH Annex XVII should be restricted. (February 02, 2015).

83. P. D. García, R. Sapienza, Á. Blanco, and C. López, Photonic glass: a novel random material for light. *Adv. Mater.* **19**, 2597–2602 (2007).

84. S.-H. Kim, S. Y. Lee, S.-M. Yang, and G.-R. Yi, Self-assembled colloidal structures for photonics. *NPG Asia Mater.* **3**, 25–33 (2011).

85. C. H. Lim, H. Kang, and S.-H. Kim, Colloidal assembly in Leidenfrost drops for noniridescent structural color pigments. *Langmuir* **30**, 8350–8356 (2014).

86. Y. Takeoka, S. Yoshioka, A. Takano, S. Arai, K. Nueangnoraj, H. Nishihara, M. Teshima, Y. Ohtsuka, and T. Seki, Production of colored pigments with amorphous arrays of black and white colloidal particles. *Angew. Chem. Int. Ed.* **52**, 7261–7265 (2013).

87. J. D. Forster, H. Noh, S. F. Liew, V. Saranathan, C. F. Schreck, L. Yang, J.-G. Park, R. O. Prum, S. G. J. Mochrie, C. S. O'Hern, H. Cao, and E. R. Dufresne, Biomimetic isotropic nanostructures for structural coloration. *Adv. Mater.* **22**, 2939–2944 (2010).

88. A. Kawamura, M. Kohri, G. Morimoto, Y. Nannichi, T. Taniguchi, and K. Kishikawa, Full-color biomimetic photonic materials with iridescent and non-iridescent structural colors. *Sci. Rep.* **6**, 33984 (2016).

89. I. Lee, D. Kim, J. Kal, H. Baek, D. Kwak, D. Go, E. Kim, C. Kang, J. Chung, Y. Jang, S. Ji, J. Joo, and Y. Kang, Quasi-amorphous colloidal structures for electrically tunable full-color photonic pixels with angle-independency. *Adv. Mater.* **22**, 4973–4977 (2010).

90. Y. Zhang, B. Dong, A. Chen, X. Liu, L. Shi, and J. Zi, Using cuttlefish ink as an additive to produce non-iridescent structural colors of high color visibility. *Adv. Mater.* **27**, 4719–4724 (2015).

91. M. Teshima, T. Seki, R. Kawano, S. Takeuchi, S. Yoshioka, and Y. Takeoka, Preparation of structurally colored, monodisperse spherical assemblies composed of black and white colloidal particles using a micro-flow-focusing device. *J. Mater. Chem. C* **3**, 769–777 (2015).

92. D. Ge, L. Yang, G. Wu, and S. Yang, Angle-independent colours from spray coated quasi-amorphous arrays of nanoparticles. *J. Mater. Chem. C* **2**, 4395–4400 (2014).

93. M. Iwata, M. Teshima, T. Seki, S. Yoshioka, and Y. Takeoka, Bio-inspired bright structurally colored colloidal amorphous array enhanced by controlling thickness and black background. *Adv. Mater.* **29**, 1605050 (2017).

94. J.-G. Park, S.-H. Kim, S. Magkiriadou, T. M. Choi, Y.-S. Kim, and V. N. Manoharan, Full-spectrum photonic pigments with non-iridescent structural colors through colloidal assembly. *Angew. Chem. Int. Ed.* **53**, 2899–2903 (2014).

95. S. Magkiriadou, J.-G. Park, Y.-S. Kim, and V. N. Manoharan, Disordered packings of core-shell particles with angle-independent structural colors. *Opt. Mater. Express* **2**, 1343 (2012).

96. G. I. Márk, Z. Vértesy, K. Kertész, Z. Bálint, and L. P. Biró, Order-disorder effects in structure and color relation of photonic-crystal-type nanostructures in butterfly wing scales. *Phys. Rev. E* **80**, 51903 (2009).

97. B. E. Warren, *X-Ray Diffraction* (Dover Publications, Inc., 1990).

98. V. K. Pecharsky and P. Y. Zavalij, *Fundamentals of powder diffraction and structural characterization of materials* (Springer, ed. 2, 2009).

99. R. P. Porter, Determination of structure of weak scatterers from holographic images. *Opt. Commun.* **39**, 362–364 (1981).

100. T. D. Gerke and R. Piestun, Aperiodic volume optics. *Nat. Photonics* **4**, 188–193 (2010).

101. M. E. Zoorob, M. D. B. Charlton, G. J. Parker, J. J. Baumberg, and M. C. Netti, Complete photonic bandgaps in 12-fold symmetric quasicrystals. *Nature* **404**, 740–743 (2000).

102. C.-F. Lai, J.-Y. Chi, H.-C. Kuo, C.-H. Chao, H.-T. Hsueh, J.-F. T. Wang, and W.-Y. Yeh, Anisotropy of light extraction from GaN two-dimensional photonic crystals. *Opt. Express* **16**, 7285–7294 (2008).

103. H. Huang, C.-P. Huang, C. Zhang, X.-H. Hong, X.-J. Zhang, Y.-Q. Qin, and Y.-Y. Zhu, From Ewald sphere to Ewald shell in nonlinear optics. *Sci. Rep.* **6**, 29365 (2016).

104. R. O. Prum and R. H. Torres, A fourier tool for the analysis of coherent light scattering by bio-optical nanostructures. *Integr. Comp. Biol.* **43**, 591–602 (2003).

105. C. J. R. Sheppard, S. S. Kou, and J. Lin, The Green-function transform and wave propagation. *Front. Phys. (Lausanne)* **2**, 67 (2014).

106. H. L. Leertouwer, B. D. Wilts, and D. G. Stavenga, Refractive index and dispersion of butterfly chitin and bird keratin measured by polarizing interference microscopy. *Opt. Express* **19**, 24061–24066 (2011).

107. L. Maiwald, T. Sommer, M. S. Sidorenko, R. R. Yafyasov, M. E. Mustafa, M. Schulz, M. V. Rybin, M. Eich, and A. Y. Petrov, Control over light emission in low-refractive-index artificial materials inspired by reciprocal design. *Adv. Opt. Mater.* **10**, 2100785 (2022).

108. S. John, Strong localization of photons in certain disordered dielectric superlattices. *Phys. Rev. Lett.* **58**, 2486–2489 (1987).

109. J. D. Joannopoulos, P. R. Villeneuve, and S. Fan, Photonic crystals: putting a new twist on light. *Nature* **386**, 143–149 (1997).

110. H. Men, K. Y. K. Lee, R. M. Freund, J. Peraire, and S. G. Johnson, Robust topology optimization of three-dimensional photonic-crystal band-gap structures. *Opt. Express* **22**, 22632–22648 (2014).

111. A. Cerjan and S. Fan, Complete photonic band gaps in supercell photonic crystals. *Phys. Rev. A* **96**, 051802(R) (2017).

112. P. R. Villeneuve and M. Piché, Photonic band gaps in two-dimensional square and hexagonal lattices. *Phys. Rev. B* **46**, 4969–4972 (1992).

113. K. M. Ho, C. T. Chan, and C. M. Soukoulis, Existence of a photonic gap in periodic dielectric structures. *Phys. Rev. Lett.* **65**, 3152–3155 (1990).

114. D. Levine and P. J. Steinhardt, Quasicrystals: A new class of ordered structures. *Phys. Rev. Lett.* **53**, 2477–2480 (1984).

115. Z. V. Vardeny, A. Nahata, and A. Agrawal, Optics of photonic quasicrystals. *Nat. Photonics* **7**, 177–187 (2013).

116. W. Steurer and D. Sutter-Widmer, Photonic and phononic quasicrystals. *J. Phys. D* **40**, R229-R247 (2007).

117. X. Zhang, Z.-Q. Zhang, and C. T. Chan, Absolute photonic band gaps in 12-fold symmetric photonic quasicrystals. *Phys. Rev. B* **63**, 81105 (2001).

118. S.-Y. Jeon, H. Kwon, and K. Hur, Intrinsic photonic wave localization in a three-dimensional icosahedral quasicrystal. *Nat. Phys.* **13**, 363–368 (2017).

119. C. Rockstuhl and F. Lederer, Suppression of the local density of states in a medium made of randomly arranged dielectric spheres. *Phys. Rev. B* **79**, 132202 (2009).

120. M. Florescu, S. Torquato, and P. J. Steinhardt, Designer disordered materials with large, complete photonic band gaps. *Proc. Natl. Acad. Sci. U.S.A.* **106**, 20658–20663 (2009).

121. W. Man, M. Florescu, K. Matsuyama, P. Yadak, G. Nahal, S. Hashemizad, E. Williamson, P. Steinhardt, S. Torquato, and P. Chaikin, Photonic band gap in isotropic hyperuniform disordered solids with low dielectric contrast. *Opt. Express* **21**, 19972–19981 (2013).

122. Y. Xu, W. Liang, A. Yariv, J. G. Fleming, and S.-Y. Lin, High-quality-factor Bragg onion resonators with omnidirectional reflector cladding. *Opt. Lett.* **28**, 2144–2146 (2003).

123. M. E. Pollard and G. J. Parker, Low-contrast bandgaps of a planar parabolic spiral lattice. *Opt. Lett.* **34**, 2805–2807 (2009).

124. M. Goldberg, A class of multi-symmetric polyhedra. *Tohoku Math. J.* **43**, 104–108 (1937).

125. E. B. Saff and A. B. J. Kuijlaars, Distributing many points on a sphere. *Math. Intell.* **19**, 5–11 (1997).

126. A. E. Krasnok, A. P. Slobozhanyuk, C. R. Simovski, S. A. Tretyakov, A. N. Poddubny, A. E. Miroshnichenko, Y. S. Kivshar, and P. A. Belov, An antenna model for the Purcell effect. *Sci. Rep.* **5**, 12956 (2015).

127. K. M. Schulz, H. Vu, S. Schwaiger, A. Rottler, T. Korn, D. Sonnenberg, T. Kipp, and S. Mendach, Controlling the spontaneous emission rate of quantum wells in rolled-up hyperbolic metamaterials. *Phys. Rev. Lett.* **117**, 85503 (2016).

128. K. M. Schulz, D. Jalas, A. Y. Petrov, and M. Eich, Reciprocity approach for calculating the Purcell effect for emission into an open optical system. *Opt. Express* **26**, 19247–19258 (2018).

129. A. Della Villa, S. Enoch, G. Tayeb, V. Pierro, V. Galdi, and F. Capolino, Band gap formation and multiple scattering in photonic quasicrystals with a Penrose-type lattice. *Phys. Rev. Lett.* **94**, 183903 (2005).

130. M. A. Kaliteevski, S. Brand, R. A. Abram, T. F. Krauss, P. Millar, and R. M. D. La Rue, Diffraction and transmission of light in low-refractive index Penrose-tiled photonic quasicrystals. *J. Phys. Condens. Matter* **13**, 10459–10470 (2001).

131. MathWorks Help Center, *Prominence* (available at https://www.mathworks.com/help/signal/ug/prominence.html, last retrieved on March 12, 2023).

132. R. H. Hardin, N. J. A. Sloane, and W. D. Smith, *Tables of spherical codes with icosahedral symmetry* (available at http://neilsloane.com/icosahedral.codes/, last retrieved on March 12, 2023).

133. G. Boussatour, P.-Y. Cresson, B. Genestie, N. Joly, and T. Lasri, Dielectric characterization of Polylactic Acid substrate in the frequency band 0.5–67 GHz. *IEEE Microw. Wirel. Compon. Lett.* **28**, 374–376 (2018).

134. J. Li, C.-H. Wen, S. Gauza, R. Lu, and S.-T. Wu, Refractive indices of liquid crystals for display applications. *J. Display Technol.* **1**, 51–61 (2005).

135. M. J. Ventura and M. Gu, Engineering spontaneous emission in a quantum-dot-doped polymer nanocomposite with three-dimensional photonic crystals. *Adv. Mater.* **20**, 1329–1332 (2008).

136. V. Hwang, A. B. Stephenson, S. Magkiriadou, J.-G. Park, and V. N. Manoharan, Effects of multiple scattering on angle-independent structural color in disordered colloidal materials. *Phys. Rev. E* **101**, 12614 (2020).

137. V. Hwang, A. B. Stephenson, S. Barkley, S. Brandt, M. Xiao, J. Aizenberg, and V. N. Manoharan, Designing angle-independent structural colors using Monte Carlo simulations of multiple scattering. *arXiv* 2007.14831 (2020).

List of publications

Papers

- L. Maiwald, S. Lang, D. Jalas, H. Renner, A. Y. Petrov, and M. Eich, Ewald sphere construction for structural colors. *Opt. Express* **26**, 11352-11365 (2018).
- L. Maiwald, T. Sommer, M. S. Sidorenko, R. R. Yafyasov, M. E. Mustafa, M. Schulz, M. V. Rybin, M. Eich, and A. Y. Petrov, Control over light emission in low-refractive-index artificial materials inspired by reciprocal design. *Adv. Opt. Mater.* **10**, 2100785 (2022).
- G. Shang, L. Maiwald, H. Renner, D. Jalas, M. Dosta, S. Heinrich, A. Petrov, and M. Eich, Photonic glass for high contrast structural color. *Sci. Rep.* **8**, 7804 (2018).

Conference talks

- L. Maiwald, D. Jalas, S. Lang, A. Y. Petrov, and M. Eich, CST Microwave Studio simulations of structural color in disordered structures. CST European User Conference, April 2016, Strasbourg, France.
- L. Maiwald, D. Jalas, S. Lang, A. Y. Petrov, and M. Eich, Ewald sphere approach to structural color in disordered structures. EMRS Spring Meeting, May 2016, Lille, France.
- L. Maiwald, D. Jalas, S. Lang, A. Y. Petrov, and M. Eich, Application of the Ewald sphere approach to structural colors. DoKDoK, September 2016, Oppurg, Germany.
- L. Maiwald, G. Shang, H. Renner, S. Lang, D. Jalas, A. Y. Petrov, and M. Eich, Optimization of non-iridescent structural colors using CST Microwave Studio. CST European User Conference, June 2018, Munich, Germany.
- L. Maiwald, S. Lang, D. Jalas, H. Renner, A. Y. Petrov, and M. Eich, Ewald sphere construction for light scattering in disordered media. MRS Fall Meeting, November 2018, Boston, USA.
- G. Shang, L. Maiwald (speaker), H. Renner, D. Jalas, M. Dosta, S. Heinrich, A. Y. Petrov, and M. Eich, High-contrast structural color based on core-shell photonic glass. MRS Fall Meeting, November 2018, Boston, USA.
- L. Maiwald, T. Sommer, M. Schulz, M. Eich, and A. Y. Petrov, Complete photonic bandgap in distributed quasicrystals with arbitrarily small refractive-index contrast. DisoMAT Conference, September 2019, Potsdam, Germany.
- L. Maiwald, T. Sommer, M. Schulz, M. Eich, and A. Y. Petrov, Complete photonic bandgap in quasiperiodic structures with arbitrarily small refractive-index contrast. 3DEXPERIENCE Conference, November 2019, Darmstadt, Germany.

Posters

- L. Maiwald, S. Lang, D. Jalas, A. Y. Petrov, and M. Eich, Holography-based disordered structures for tailored scattering. SPP 1839 “Tailored Disorder” Spring School, May 2017, Karlsruhe, Germany.